FINAL REPORT

METEOROID HAZARDS

IN

DEEP SPACE

Prepared Under

Contract NAS 9-8104
National Aeronautics and Space Administration
Manned Spacecraft Center
Houston, Texas

Prepared by:

H. Chaess
S. Chandra
R. Grenda
R. Lambert
S. Neste
B. Rutter
W. Shaffer
R. Soberman

Space Sciences Laboratory
Missile and Space Division
General Electric Company
PO Box 8555
Philadelphia, Pennsylvania
19101

FINAL REPORT

METEOROID HAZARDS

IN

DEEP SPACE

Prepared Under

Contract NAS 9-8104
National Aeronautics and Space Administration
Manned Spacecraft Center
Houston, Texas

Prepared by: H. Chaes
S. Chandra
R. Grenda
R. Lambert
S. Neste
B. Rutter
W. Shaffer
R. Soberman

Space Sciences Laboratory
Missile and Space Division
General Electric Company
PO Box 8555
Philadelphia, Pennsylvania
19101

NASA CR 92399

TABLE OF CONTENTS

		Page
SISYPHUS - A NEW CONCEPT IN THE MEASUREMENT OF METEORIC FLUX		
I.	Introduction	1
II.	Concept of the Sisyphus System	1
III.	Data Return Rate	3
	A. Detection Level	3
	B. Event Rate	3
IV.	Thresholds for Signals and False Alarms	5
V.	Circuit Logic	5
VI.	Laboratory Demonstration Experiment	6
VII.	Advantages and Disadvantages	7
PROJECT REPORT #1 - SISYPHUS FALSE ALARM RATE		
I.	Introduction	1-1
II.	Experiment	1-1
	A. Objective	1-1
	B. Circuit Design	1-1
	1. Noise	1-1
	2. Threshold	1-3
	3. Coincidence	1-5
	4. Pulse Discrimination	1-5
	5. Final Preparation of Equipment	1-8
III.	Discussion	1-8
	A. Theoretical Considerations	1-8
	1. Threshold and Coincidence	1-8
	2. Threshold and Pulse Discrimination	1-14
	B. Evaluation of Results	1-14

IV. Conclusions 1-19

PROJECT REPORT #2 - SIGNAL AND NOISE ERROR ANALYSIS

I. Introduction 2-1

II. Theoretical Analysis 2-1

A. Noise-Free Considerations 2-1

1. Errors in Pulse-Width 2-1
2. Errors in Differential Times 2-4

B. Noise Considerations 2-6

1. Errors in Pulse Width 2-6
2. Errors in Differential Times 2-7

III. Experimental Verification of Theory 2-9

IV. Conclusions and Summary 2-17

PROJECT REPORT #3 - THE TWO-CONE SISYPHUS SYSTEM

I. Introduction 3-1

II. Range Error Analysis 3-1

III. Geometry and Mathematics of the Two-Cone Sisyphus 3-2

IV. Conclusions 3-11

PROJECT REPORT #4 - SOLUTION FOR A SISYPHUS SYSTEM OF GENERALIZED GEOMETRY

I. Introduction 4-1

II. Geometrical Considerations 4-1

III. Mathematical Solution for the General System 4-2

IV. Laboratory Model and Experimental Results 4-9

V. Conclusions 4-10

PROJECT REPORT #5 - OPTICAL CONSIDERATIONS FOR A SISYPHUS INTERPLANETARY METEOROID MEASUREMENT SYSTEM

I.	Introduction	5-1
II.	System Design	5-
	A. Design Constraints for the Optical System	5-
	B. Design Requirements	5-1
	C. Design Concept	5-1
	D. Aberration Analysis	5-2
III.	Detailed Design	5-2
	A. Preliminary Study	5-2
	B. Detailed Specifications of the Optical System	5-3
	C. Calculation of the Components	5-3
IV.	Dual Experiment Possibility	5-6
V.	Appendix - Sisyphus Optical Accuracy	5-9

FINAL REPORT

METEOROID HAZARDS IN DEEP SPACE

SUMMARY

This Final Report on the design study, phase 1 of contract #NAS 9-8104 describes the work done in developing the Sisyphus meteoroid detection scheme for use on interplanetary research vehicles. The report is divided into a number of sections, each covering a specific topic which was treated in detail.

The first section describes the concept as it is currently conceived. Specifically, it is a paper which was presented at the XIXth International Astronautical Federation meeting in New York on October 16, 1968. This description differs in a number of respects from that which was given in the original proposal, GE N-10897. The prime reason for the difference is that with the postponement of the Voyager concept of interplanetary exploration for the present, emphasis was shifted to systems compatible with the Mariner and Pioneer type of spacecraft. The system concept contained within this report reflects this shift in emphasis.

The subsequent sections treat in turn: (a) the false alarm rate expected on Sisyphus; (b) the signal and noise error analysis; (c) the two-cone Sisyphus system (assuming mechanical failure of the third and redundant subsystems); (d) solution for a Sisyphus system of generalized geometry; and (e) the Sisyphus optical design study. Currently envisioned errors which can arise in the use of the Sisyphus system are treated within the sections themselves. The number of parameters involved in a Sisyphus measurement makes it impossible to specify how a given error in one parameter will affect the final solution unless most of the other parameters are determined.

Continued work on errors is contemplated during the second phase of the contract during which a breadboard will be constructed. Efforts are continuing to define a small light-weight interplanetary version of the Sisyphus concept which can be adapted to the presently proposed interplanetary vehicles. A proposal with NASA Manned Spacecraft Center for the Pioneer F/G Missions through the asteroid belt to Jupiter is currently in preparation. Efforts on this proposal will undoubtedly modify the current concept of the Sisyphus system. Such modifications will be included in the final contract report.

No. SD 121

SISYPHUS – A NEW CONCEPT IN THE MEASUREMENT OF METEORIC FLUX

by

R. N. GRENDA, Research Physicist; W. A. SHAFFER, Research Fellow;
and R. K. SOBERMAN, Project Leader—Space Physics;
General Electric Company, Space Sciences Laboratory
Philadelphia, Pennsylvania, U.S.A.

IAF Paper
SD 121

19th Congress of the International Astronautical Federation

NEW YORK, N. Y./OCTOBER 13-19, 1968

SISYPHUS -- A NEW CONCEPT IN THE MEASUREMENT OF METEORIC FLUX

R. N. Grenda, Research Physicist; W. A. Shaffer, Research Fellow; and R. K. Soberman, Project Leader--Space Physics; General Electric Company, Space Sciences Laboratory, Philadelphia, Pennsylvania.

Abstract

A new concept in space-borne meteoroid measurements uses solar radiation reflected from the meteoroid for detection, range and velocity measurements. Three optical systems, coupled to photomultipliers and having overlapping conical fields of view, detect any meteoroid passing through the overlap region. The times of entrance into and exit from each cone are utilized to completely determine the body's trajectory and velocity. An "albedo cross-section" equal to the reflectivity times the illuminated cross-sectional area is determined from the calculated range and measured irradiance. Feasibility has been demonstrated by laboratory experiments which simulate the passage of an illuminated meteoroid through the field of view.

I. Introduction

A prime consideration in the design of space vehicles is the possibility of damage caused by collisions with extraterrestrial debris. Depending upon the size, mass and velocity of the impinging particles, surface erosion, puncture or failure of the exposed spacecraft structure can result. In order to provide adequate protection for critical spacecraft components, or possibly occupants, one must be able to determine the probability of damage occurring to the structure.

An estimate of the magnitude of the meteoroid hazard to the spacecraft requires a knowledge of the meteoroid flux and characteristics which the spacecraft is likely to encounter in the deep-space or near-earth environment. A pessimistic estimate of the meteoroid hazard can result in a severe performance penalty if additional weight is incorporated into the spacecraft structure to provide meteoroid protection. For this reason, more accurate knowledge of the meteoroid environment likely to be encountered in space under normal or abnormal conditions must be acquired.

Limited interplanetary measurements have been made on micrometeoroids, notably on the US and USSR Mars and Venus interplanetary probes.[1,2,10] These investigations have been carried out utilizing piezoelectric detectors which could only measure the momentum of the particle. Other space-borne micrometeoroid detectors had been utilized in the vicinity of the Earth. These have included particle collection experiments from rockets and satellites,[8,13] piezoelectric measurements,[6,12] and penetration measurements.[4] Only recently have attempts been made to measure velocities of meteoric material in space.[11] This measurement was only a beginning and the detector used could only determine one component of the velocity. The Explorer XVI, XXIII and Pegasus satellites were designed to provide engineering data concerning the near earth meteoroid environment. The measurements were based on the penetration of sheets of various materials of known thickness. Due to the uncertainties in penetration mechanics, the mass range associated with the experiments is difficult to determine to better than a factor of 10. In fact, when one considers the measurements of micrometeoroid flux in the mass range from 10^{-6} to 10^{-12} grams, the disagreement between various investigators becomes several orders of magnitude. The large scatter in the data suggests the need for an improved measurement technique which can simultaneously measure velocity and mass and be applicable over a large enough area to give statistical confidence in the data.

The Sisyphus system for meteoroid detection has the capability of determining range, velocity and size (with certain assumptions regarding reflectivity) of particles travelling at meteoric velocities. This new concept in meteoroid measurements uses reflected or scattered solar radiation from the meteoroid for detection. The transit is measured by three independent, non-imaging optical subsystems. Entrance and exit times of the particle through each of the three fields of view are all that is required to completely determine the range and three velocity components of the body through the system. From the calculated range and the measured amplitude of the intensity, an "albedo cross-section" equal to the reflectivity times the illuminated cross-sectional area is determined. A single meteoroid experiment can yield significant statistical data over six orders of magnitude of meteoroid mass. The detection system is completely passive and its relatively low weight, size, power and telemetry requirements are ideal for meteoroid astronomy measurements in remote regions of the solar system. The system can also be used in conjunction with other detectors, such as impact or penetration gauges, to yield mass, density and penetrating ability of the measured meteoroids.

II. Concept of the Sisyphus System

It is well known that a body in space will reflect sunlight by which it can be seen or detected. If an optical detector is oriented in space such that it looks away from the sun, we can approximate the amount of light incident on the aperture which results from the sunlight reflected by a spherical object. Thus,

$$I = \frac{I_O \, r \, \pi a^2}{2 s^2 \pi R^2} = \frac{I_O \, r}{2 s^2} \left[\frac{a}{R}\right]^2 \qquad (1)$$

where I is the intensity of the reflected sunlight incident on the optics; I_O is the solar illumination at the object; r is the reflectivity coefficient of the object; a is the radius of the object; R is the distance from the object to the detector; and s is the distance from the sun in astronomical units. We have assumed that the object is diffusely reflecting the sunlight uniformly in all directions.

Like most of the assumptions that are made in this description, this represents a worst case.

Using equation (1), one can calculate the size of an object that can be seen against a dark background. However, it is clear from the equation that a single detector would have no way of distinguishing different objects which had the same a/R ratio (i.e., a small object at close range from a large object far away). The Sisyphus system provides a means of determining the range and, hence, the size of the meteoroid.

Consider three optical subsystems as defining three parallel cones in space. Each subsystem consists of field optics (lens or mirror) and a photoelectric detector. If the optic subsystems are identical, then the edges of the field of view remain at a fixed distance from each other regardless of range. Any luminous object which crossed through the intersecting fields of view would then be detected by each of the optical systems. A geometrical model of the three optic Sisyphus system is shown in Figure 1. From the entrance and exit times in each field of view, one can completely calculate the trajectory of the body in space pro ided only that the body does not change its velocity during the transit time.

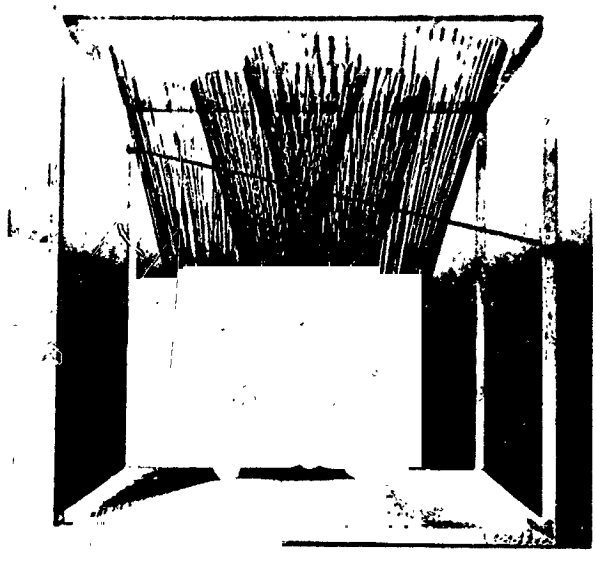

Figure 1. Geometrical Model of the Sisyphus System

Mathematically, the Sisyphus problem is equivalent to finding the intersection of a straight line with three parallel cones. To demonstrate the mathematics of the system, we will choose a system of three identical cones with half angles α, as shown in Figure 2. Lines joining their apexes form an arbitrary triangle in the plane perpendicular to their axes. For purposes of convention, the vector from the base of the i^{th} cone to the particle's entrance into that cone is designated $\hat{\rho}_i$ and the vector to the particle's exit is $\hat{\sigma}_i$ The corresponding angles of entrance and exit in the plane of the apexes are φ_i and ψ_i. Times of entrance and exit at the i^{th} cone are designated τ_{ij}, where j is 1 for an entrance point or 2 for an exit point. The vector $\hat{v}$ is an arbitrary velocity vector.

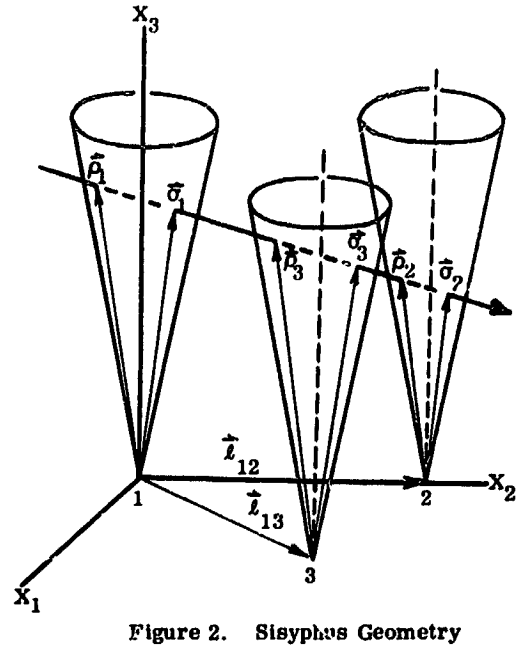

Figure 2. Sisyphus Geometry (for convention only)

Using this convention, five independent vector equations result:

$$\hat{\sigma}_1 = \hat{\rho}_1 + (\tau_{12} - \tau_{11})\,\hat{v} \qquad (2)$$

$$\hat{\rho}_2 = \hat{\rho}_1 + (\tau_{21} - \tau_{11})\,\hat{v} - \hat{\ell}_{12}$$

$$\hat{\sigma}_2 = \hat{\rho}_1 + (\tau_{22} - \tau_{11})\,\hat{v} - \hat{\ell}_{12}$$

$$\hat{\rho}_3 = \hat{\rho}_1 + (\tau_{31} - \tau_{11})\,\hat{v} - \hat{\ell}_{13}$$

$$\hat{\sigma}_3 = \hat{\rho}_1 + (\tau_{32} - \tau_{11})\,\hat{v} - \hat{\ell}_{13}$$

By breaking these into components, we have 15 equations in 15 unknowns - ρ_i, σ_i, φ_i, ψ_i, and v_i - so a solution exists. Since the derivation is long and tedious, it will be omitted here. The solution has been programmed for computer use.

The above vector equations remain unchanged if the cone axes are misaligned. However, the 15 component equations are more complex since they involve two additional angles for each cone necessary to specify its orientation. This misaligned case has been reduced from the 15 original equations to 3 equations in 3 unknowns. Because of their complexity, further reduction appears impractical. Numerical solutions are obtained by computer iteration.

Thus, independent of the amplitude of the signals detected by the individual optical systems, one can estab-

lish the three velocity components and the range of the luminous body. Using this calculated range, the measured light intensity at the detector and the known solar intensity, one can solve equation (1) for the product of the reflectivity and the cross-sectional area, and thus determine the mean radius of the body to an uncertainty of the square root of the reflectivity. Further, from the real time at which the event took place, the known position and orientation in space of the vehicle from which the measurement was made and the three velocity components of the body, the complete orbit of the body in the solar system can be determined.

III. Data Return Rate

Detection Level

The system is limited primarily by two factors - the time required to produce a detectable signal (one photoelectron) and the noise generated by the star background. Since the detector's aperture is fixed, threshold irradiance will generate a given number of photoelectrons per second. Statistically, the minimum time to produce a detectable signal is the time between two photoelectrons. This and the noise produced by the star background can both be calculated.

According to Allen,[3] the mean starlight level can be represented by 120 tenth magnitude stars (visual) per square degree. This number varies from 360 tenth magnitude stars per square degree in the plane of the galactic equator to 44 toward the galactic poles, dropping rapidly with latitude. Since a tenth magnitude star generates 3.1×10^{-17} watts/cm^2 in the visual, the mean stellar background irradiance is 3.7×10^{-15} watts/cm^2 - deg^2. The polar and equatorial values are 1.4×10^{-15} and 1.1×10^{-14} watts/cm^2 - deg^2, respectively.

The minimum signal irradiance required for a meteoroid's detection can be found from the limiting signal to noise ratio of the electronics. The noise generated by a background limited photomultiplier system is given by

$$i_n = \sqrt{2\, i_B\, q\, f} \qquad (3)$$

where i_B is the total background current; q is the unit electrical charge; and f is the frequency defined by $1/2\,\pi\,\tau$, τ being the time constant of the circuit. Considering a Sisyphus system having cone half angles of α degrees and optical apertures of D cm, the background current can be written as $i_B = I_B\,\eta \left(\frac{\pi\,\alpha\,D}{2}\right)^2$, where I_B is the background intensity in watts per square degree and η is the photomultiplier efficiency in amperes per watt. For an S20 photocathode surface, η is 4×10^{-2} amperes per watt. Using the mean star background and a frequency of one megahertz, we find that the noise encountered will be $i_n = 1.08 \times 10^{-14}\ \alpha\, D$ amperes. The signal can be written as

$$i_s = I\,\eta\,\frac{\pi\,D^2}{4} \qquad (4)$$

where I is the irradiance due to the particle. For a minimum i_s/i_n detectable by the electronics, the minimum detectable meteoroid irradiance is

$$I = 3.43 \times 10^{-13}\ \frac{\alpha}{D}\ (i_s/i_n)\ \text{watts/cm}^2 \qquad (5)$$

Event Rate

Before a value for the data return rate can be estimated, it is necessary to select a model for the flux of meteoroids in space and their mass distribution. We will, for the present purposes, adopt the radio and photographically determined rate of Hawkins & Upton[7] as modified by Whipple[14] since we will be dealing with approximately the same range of masses as these ground based detectors. Removing an earth shielding factor of 1/2 and reducing the total numbers by 78% to allow for the Earth's gravitational focussing effect, this flux can be expressed as

$$\log_{10} \Phi = -\frac{4}{3} \log_{10} m - 18.3 \qquad (6)$$

where Φ is the flux/cm^2/sec through a randomly oriented surface and m is the mass of the meteoroid in grams.

The differential of equation (6) can be written as:

$$\frac{d\Phi}{dm} = -6.8 \times 10^{-19}\ m^{-7/3} \qquad (7)$$

The effective area of the Sisyphus system is a function of the size of the particle. We can approximate this area by

$$A = \frac{2\,\pi^2}{180}\ \alpha\ (R - R_0)^2 \qquad (8)$$

where R_0 is the range at which the cones effectively intersect. Equation (1) can now be rewritten, using $I_O = 0.14$ watts/cm^2 for the solar constant

$$\frac{a}{R} = 2.22 \times 10^{-6} \left[\frac{\alpha\, s^2\, (i_s/i_n)}{r\, D}\right]^{1/2} \qquad (9)$$

Using this rate, the effective area becomes

$$A = 2.22 \times 10^{10}\ \frac{r\, D}{s^2\, (i_s/i_n)}\ (s - a_0)^2 \qquad (10)$$

where a_0 is the radius of the smallest detectable particle. Assuming spherical meteoroids of density ρ grams/cm^3, we have $a = (3\,m/4\,\pi\rho)^{1/3}$. Substituting this into equation (10), we obtain

$$A = 8.66 \times 10^9\ \frac{r\, D}{\rho^{2/3}\, s^2 (i_s/i_n)}\ (m^{1/3} - m_0^{1/3})^2\ \text{cm}^2 \qquad (11)$$

where m and m_0 (the minimum mass) are expressed in grams.

The event rate measured by the Sisyphus system can be written as

$$N = \int_A \int_\Phi d\,A\,d\,\Phi = \int_{\Phi_0}^{\Phi_2} A\,d\,\Phi. \qquad (12)$$

Using equation (7) for the differential of the flux, the event rate as a function of mass is given by

$$N = 5.83 \times 10^{-9} \frac{r\,D}{\rho^{2/3}\,s^2\,(i_s/i_n)} \cdot \int_{m_0}^{\infty} m^{-7/3}\,(m^{1/3} - m_0{}^{1/3})^2\,dm$$

$$= 1.46 \times 10^{-9} \frac{r\,D}{\rho^{2/3}\,s^2\,(i_s/i_n)}\; m_0{}^{-2/3} \qquad (13)$$

We can approximate the effective intersection range, R_0, by

$$R_0 \approx \frac{d}{\alpha}\,\frac{180}{\pi} \qquad (14)$$

where d is the separation distance between cone axes. This yields

$$a_0 = 1.26 \times 10^{-4}\,d \left[\frac{s^2\,(i_s/i_n)}{\alpha\,r\,D}\right]^{1/2} \qquad (15)$$

and

$$m_0 = 8.38 \times 10^{-12}\,d^3\,\rho \left[\frac{s^2\,(i_s/i_n)}{\alpha\,r\,D}\right]^{3/2} \qquad (16)$$

Substitution of the expression for m_0 into equation (13) gives the expected data return rate as

$$N = 3.54 \times 10^{-2} \frac{r^2\,D^2\,\alpha}{d^2\,\rho^{4/3}\,s^4\,(i_s/i_n)^2}\ \text{sec}^{-1} \qquad (17)$$

Again following Whipple,[14] we take the mean density of meteoroids to be 0.44 grams/cm^3. Estimates of the coefficient of reflectivity of meteoroids appear to lie between 0.07 and 0.2. We will assume that the mean albedo is 0.1. With the above assumptions, the data return rate in events per day at one astronomical unit from the sun (s = 1) becomes

$$N = 91.7 \frac{D^2\,\alpha}{d^2\,(i_s/i_n)^2}\ \text{day}^{-1}. \qquad (18)$$

A reasonable size for Sisyphus adapted to the present generation of interplanetary vehicles such as Mariner would have a 12 inch (30 cm) separation distance between optic axes, 6 inch (15 cm) primary apertures and 5 degree viewing half angles. To obtain a maximum false alarm rate of one per day, the signal to noise power ratio must be at least 10 (see Section IV). Thus, the signal to noise current ratio is $\sqrt{10}$. For this system, the expected data rate is 11.5 events per day. The smallest particles to be detected have radii of 2.4×10^{-3} cm and masses of 2.6×10^{-8} grams.

It is important to note that, unlike fixed area detectors, the data return rate of the Sisyphus system does not fall off proportionately to the mass distribution of the meteoroid flux. The count rate, as a function of mass, can be written as

$$N = A\,\Phi = 4.30 \times 10^{-9} \frac{r\,D}{\rho^{2/3}\,s^2\,(i_s/i_n)} \cdot m^{-4/3}\,(m^{1/3} - m_0{}^{1/3})^2 \qquad (19)$$

Thus, for large particles, the count rate decreases as $m^{-2/3}$ as opposed to fixed area systems where the count rate would decrease as $m^{-4/3}$ under our flux assumptions.

Figure 3 contains curves of count rate vs. meteoroid size for the above Sisyphus system using the two extreme values of reflectivity. The dashed curves represent the data return rate using another flux model through the micrometeoroid range. This model

$$\log_{10} \Phi = -1/2 \log_{10} m - 13.9 \qquad (20)$$

is based on penetration data from the Explorer XVI, XXIII and Pegasus satellites and was assumed for meteoroids having masses below 5×10^{-6} grams. Above 5×10^{-6} grams, the previous model was used. For comparison, the three Pegasus data return rates measured in earth orbit are also given.[4]

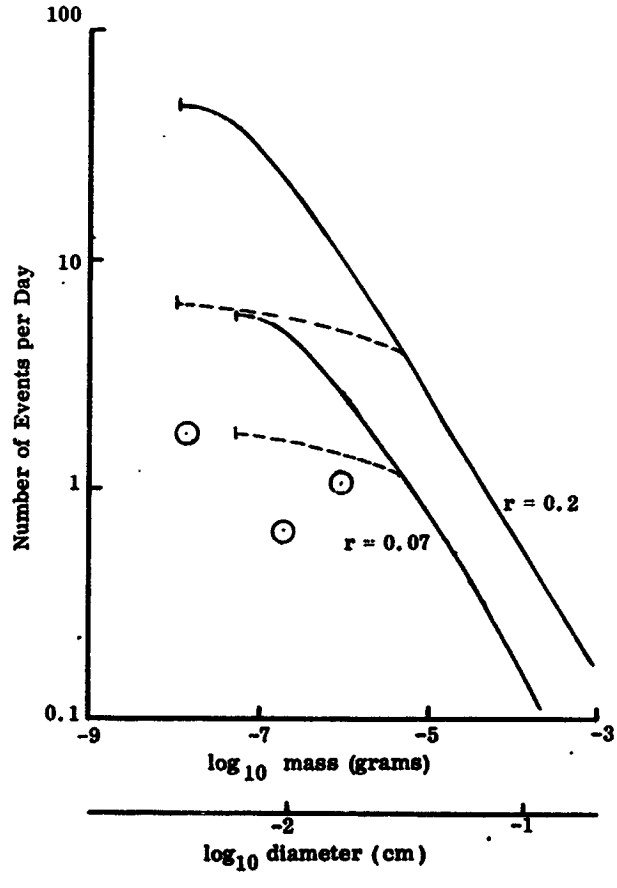

Figure 3. Data Return Rate

IV. Thresholds for Signals and False Alarms

Since the Sisyphus system consists of three optic systems from which a great deal of data is derived, one has a number of ways of distinguishing false alarms from real meteoroid events. A total false alarm rate of one per day appears reasonable. This low false alarm rate can be achieved if we set a very simple on-board threshold criteria which demands threefold coincidence for recording and subsequent transmission of an event. With the added pulse height information, most of the transmitted false alarms would be rejected in subsequent analysis. The threefold coincidence must occur during a predetermined minimum period of 2×10^{-5} seconds. This is the time for the worst case transit (v = 72 km/sec - the maximum meteoroid velocity at earth) of the field overlap at the previously defined minimum range (R_0). The one per day probability would thus be 2×10^{-5} sec divided by 86,400 sec or 2.3×10^{-10}. The probability of such noise pulses in the individual systems would be the cube root of the threefold coincidence or 6.1×10^{-4}. Since the false alarm probability can be written $e^{-T/n}$ where T is the established threshold and n is the RMS noise, the above probability requires a threshold to noise power ratio of 7.4.

The probability of detecting a signal can be written as

$$P = e^{-\frac{T}{n(1 + S/n)}} \qquad (21)$$

where S is the signal power. If, in the worst case (i.e., fastest moving particle at minimum range), we ask a 50% probability of detection (12.5% for all three), then the exponent in equation (21) must be equal to 0.69. Since we have indicated above that T/n is equal to 7.4, then S/n should be equal to 10.

The threshold is tied to the noise level by a relatively long time constant (~ 5 sec) circuit. Should the noise increase or decrease appreciably (as the vehicle changes orientation relative to the star field or when a bright star enters the field of view), the threshold will be varied to keep the ratio T/n constant at about 7.5. This will also change the sensitivity of the system.

V. Circuit Logic

The basic information available from the three photomultiplier detectors of the Sisyphus system is shown in Figure 4. In addition to measuring the three transit times, it is also desired to measure coincidence duration, three entrance differential times (start A - start B, A-C, B-C), and three exit differentials (end A - end B, A-C, B-C), some of which are redundant.

Ideally, the measurement system would be triggered into operation by the appearance of a pulse on any channel and would continue to make measurements until all three signals had disappeared. The fact that there is noise in the system requires the use of a threshold in the circuit. There will still be occasions where the noise will exceed the threshold and cause the measuring system to start operating. If a legitimate signal then

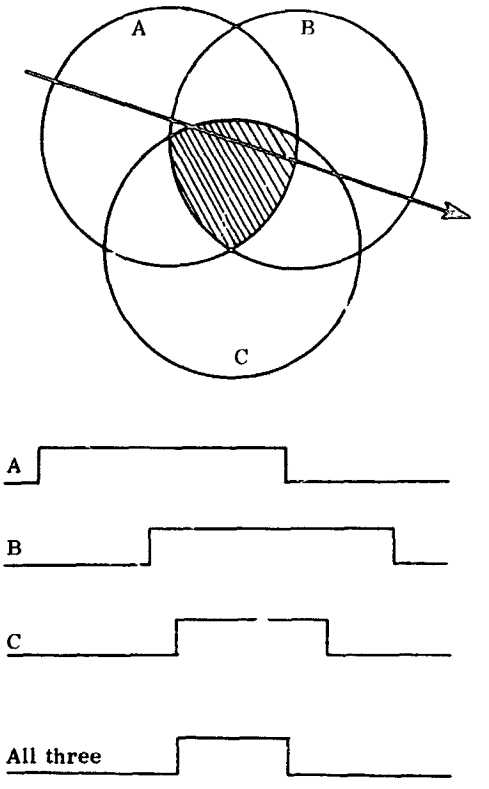

Figure 4. Basic Signals

occurred, before the system had recovered, the resulting measurements would be in error. As pointed out in Section IV, one approach to solving this problem is using multiple coincidence to confirm or reject measurements. Once a signal on any channel has started the measurements, they continue until there is no signal on any of the three channels. If a coincidence occurred during this interval, all the measurements are taken as legitimate; if not, they are rejected and the system is reset. Noise on any channel exceeding the threshold still starts the system; however, it is reset as soon as the noise drops below the threshold, resulting in negligible system dead or blind time. There is one potential problem associated with this approach. Assume a legitimate target is passing through the field of view as in Figure 4. If noise or fluctuations in target intensity cause the level to drop below the threshold while in A but before reaching C, it will be regarded as an error and rejected. It would be picked up again as soon as the perturbation had disappeared, but all measurements associated with cone A would be in error. To partially overcome this, the threshold is designed to have hysteresis. Once it has been exceeded, the threshold value is dropped to a lower level, thus reducing the probability of dropouts due to noise. Of course, the new lower threshold value cannot

be too low, or a legitimate end of signal might not be properly detected.

As indicated in Section IV, the value of the threshold in each channel is adjustable and controlled by the long-term or average background light level to maintain a constant threshold to noise ratio. This background level is included as part of the data for each event. In addition, the background is read out at regular intervals thereby providing an in-flight calibration of the system against the star background.

VI. Laboratory Demonstration Experiment

A model of the Sisyphus system has been assembled for study in the laboratory and the mathematical analysis has been programmed in Fortran IV for computer data reduction.

The laboratory model consists of three 7-power finder telescopes mated to three RCA-7265 photomultiplier tubes (Figure 5). The telescopes are mounted with their optical axes parallel and forming an equilateral triangle whose sides are a nominal 10.8 cm in length. The telescope objective has a diameter of 3 cm and a focal length of 17.35 cm. A 2.54 cm diameter field aperture restricts the optical system field of view to a cone with a half-angle of 4 degrees. Alignment and field of view were verified by projecting the images of the apertures onto a screen. The actual center-to-center spacings of the projected apertures were found to be 10.3 and 11.0 cm. This difference can be attributed to three possible sources:

a. angular misalignment of the telescopes;

b. lateral offset of the aperture from the optical axis of the objective lens (by rotation of the telescope body and observing the lateral motion of the projected aperture image this was found to be of the order of 0.6 cm); and

c. inability to determine the centers of the projected images to better than 0.3 cm.

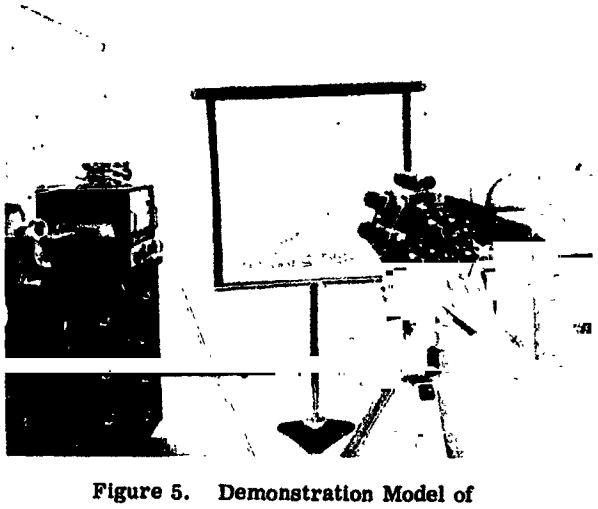

Figure 5. Demonstration Model of the Sisyphus System

In spite of these errors, the experimental values of range and velocity agree reasonably well with the computed values for this particular experimental configuration.

To simulate a solar illuminated particle, a flying spot scanner is used to project a repetitive sweep across a screen which is in the field of view of the three telescopes. The scanner being used consists of a small mirror attached to the shaft of a motor. A lens focusses the image of a small lamp and the rotating mirror causes this spot to traverse the screen. The scanner is located 1.7 meters from the screen and rotates at about 30 rps, resulting in a spot velocity of about 635 meters per second. The actual velocity of the light spot across the screen is determined by measuring the time required for the spot to cross a non-reflective surface of known dimensions placed in its path across the screen. The line of sight from the mirror to the screen is very nearly perpendicular to the plane of the screen in order to avoid significant velocity changes as the spot crosses the field of view. With a mirror to screen distance of 1.7 meters, the difference in velocity between the center and the edges of the field of view is less than 1%. By this method of simulating a solar illuminated particle, both the brightness and velocity can be easily controlled. The repetitive character of the sweep greatly eases the observational problem, while an oscilloscope camera can capture single sweep events for analysis of signal to noise characteristics.

The apparatus described has been used to perform a number of experiments in which one measures the times at which the light spot enters and leaves the field of view of each telescope. A typical oscilloscope trace is shown in Figure 6. The data inputs to the computer program which solves for the position and velocity are six entrance and exit times, the cone angle, and the spacing between the cones. An example of the experimental results is listed below:

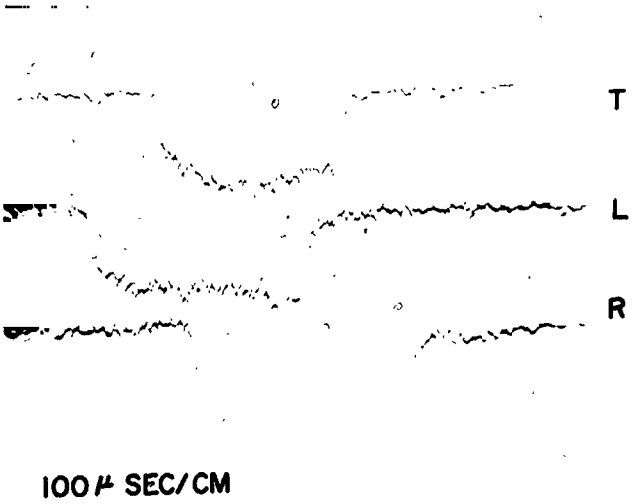

Figure 6. Oscilloscope Traces from Demonstration Sisyphus System

Trajectory Parameters	Measured	Computed from Sisyphus
R_{11}	179 cm.	173 cm.
R_{32}	168 cm.	166 cm.
V (magnitude)	6.40×10^4 cm/sec	6.35×10^4 cm/sec
v_3	1.51×10^4 cm/sec	1.26×10^4 cm/sec

The preliminary experiments have indicated that the velocity components V_1 and V_2 and the range can be determined very accurately with the present system. The axial velocity component appears to be more sensitive to errors in the entrance and exit times and in the instrument geometry parameters. Error analysis studies are in progress. The experiments have been sufficient to show the utility of the Sisyphus system in making velocity and position measurements of illuminated particles. The existing apparatus is being refined and used to test electronic and mathematical models for breadboard and flight versions of the Sisyphus system and to reconstruct some of the data situations to be encountered.

VII. Advantages and Disadvantages

As discussed above, the Sisyphus system offers a number of advantages and disadvantages when compared to any of the presently existing meteoroid detection schemes. The first advantage, when compared to ground based schemes, is the portability of the Sisyphus system. The entire system as designed for a Mariner vehicle - optics, photomultipliers, and electronics - can be built into a package of 1-1/4 cu. ft. weighing under 5 lbs.! Also, only 2 watts of power are required. With this system, meteoroid measurements can be made anywhere in the solar system where a space probe can travel. Like the ground based systems, the data about the physical nature of the meteoroid is limited. Only the "albedo cross section" can be measured.

Compared to present space borne systems, the ability of the proposed Sisyphus system to measure the astronomical quantities (i.e., orbit parameters) of the meteoroid represents a real advantage. However, the mass and cratering ability can only be inferred. For this reason, the Sisyphus system will be flown together with penetration sensors to establish a correlation in the smaller size region where a penetration sensor of reasonable area can obtain statistically significant data.

The Sisyphus system has a definite advantage over all existing meteoroid measurement schemes in that the sensitive area varies directly with the size of the meteoroids to be measured. Thus, in a mission that might last one year, a reasonable amount of data may be expected covering six orders of magnitude of meteoroid mass overlapping somewhat the scales of the ground based radio meteor detectors.

The use of independent optical systems lends a degree of credability to the final data which is not present in any of the present space borne meteoroid detection schemes. However, should one of the subsystems fail, the velocity and range can still be determined from the remaining two if the particle size is assumed. What would be required would be to adjust the three-fold coincidence requirement to a two-fold requirement and adjust the noise thresholds appropriately.

It is to be noted that the Sisyphus system utilizes "state of the art" technology achievable with proven components. A great deal of latitude exists, however, for future improvements that would enhance sensitivity and accuracy.

References

1. Alexander, W. M., "The Mission of Mariner II. Preliminary Observations: Cosmic Dust", Science 138, 1098 (1962).

2. Alexander, W. M., McCracken, C. W. and Bohn, J. L., "Zodiacal Dust: Measurements by Mariner IV", Science 149, 1240-1 (1965).

3. Allen, C. W., Astrophysical Quantities, 235 pp (U. of London Press, London, 1964).

4. Clifton, K. S., "Meteoroid Impacts" in "Scientific Results of Project Pegasus - Interim Report", NASA TM-X-53629, NASA Marshall, 3-7 (1967).

5. D'Aiutolo, C. T., Kinard, W. H. and Naumann, R. J., "Recent NASA Meteoroid Penetration Results from Satellites", Smithsonian Contributions to Astrophysics 11, 239-251 (1967).

6. Dubin, M. and McCracken, C. W., "Measurements of Distribution of Interplanetary Dust", Astronomical J. 67, 248-256 (1962).

7. Hawkins, G. S. and Upton, E. K. L., "The Influx Rate of Meteors in the Earth's Atmosphere", Astrophys. J. 128, 727-735 (1958).

8. Hemenway, C. L., Hallgren, D. S. and Kerridge, J. F., "Results from the Gemini S-12 Micrometeorite Experiment", Space Research VIII, ed. A. P. Mitra, L. G. Jacchia and W. S. Newman (North Holland, Amsterdam, 1968).

9. Naumann, R. J., "The Near-Earth Meteoroid Environment", NASA Tech. Note D-3717, 38 pp (1966).

10. Nazarova, T. N., "Preliminary Results of Investigations of Meteoric Matter Along Flight Trajectories of Zond 3 and Venus 2 Probes", Space Research VII, 1439-1442, ed. R. L. Smith-Rose and J. W. King (North Holland, Amsterdam, 1967).

11. Nilsson, C. S. and Alexander, W. M., "Measured Velocities of Interplanetary Dust Particles from OGO-1", Smithsonian Contributions to Astrophysics 11, 201-5 (1967).

12. Soberman, R. K. and Della Lucca, L., "Micrometeorite Measurements from Midas II (Satellite 1960 ζ 1)", Smithsonian Contributions to Astrophysics 7, 85-88 (1961).

July 1968

PROJECT REPORT #1

SISYPHUS FALSE ALARM RATE

METEOROID HAZARDS

IN

DEEP SPACE

Prepared Under

Contract NAS 9-8104
National Aeronautics & Space Administration
Manned Spacecraft Center
Houston, Texas

Prepared by: H. Chaess
S. Neste
B. Rutter
R. Soberman

Space Sciences Laboratory
Missile & Space Division
General Electric Company
PO Box 8555
Philadelphia, Pennsylvania
19101

I. INTRODUCTION

The Sisyphus system utilizes reflected or scattered solar radiation from a meteoroid for detection, trajectory and velocity measurements (Ref. 6). Three photoelectric detectors and associated optics which are separated by short base lines are pointed so that their optic axes are parallel and form the apexes of an equilateral triangle. The geometry of this system enables the trajectory of an object to be determined as it moves across the combined field of view of the detectors (see Fig. 1). While in the field of view, each photoelectric detector generates a signal from which transit times are obtained. The accuracy of such measurements is dependent upon the ability of the system to discriminate between noise (false alarms) and legitimate signals.

Discrimination between noise and signals can be obtained by three methods - (1) a threshold criteria, (2) a coincidence requirement, and (3) a pulse rejection technique. In the first approach, only those noise pulses which exceed a set threshold value will register as false alarms. In the second approach, coincidence signals from all three photoelectric detectors are required before a noise signal is registered while the third method requires, in addition, a minimum duration time for the pulse. Proper application of all three criteria should result in improved data return from the system which does not tax the available telemetry capacity.

II. EXPERIMENT

A. Objective

The first task in the development of the Sisyphus system is to investigate the effects of noise and threshold on discrimination of legitimate events and to demonstrate the degree of accuracy to which measurements can be made. To this end, the necessary laboratory equipment was designed, experimental data was obtained, and the results compared to the existing theories (Ref. 1, 2).

B. Circuit Design

1. Noise

To begin the investigation of the Meteoroid Detector, a noise background was needed to simulate a sky or star field. A "white noise" spectrum was selected because it supplied a "... wide, continuous frequency spectrum and its amplitude distribution simulates the characteristics of many natural phenomena ..." (Ref. 3).

Two white noise sources were considered. The first type used a regular carbon-base resistor. This type of resistor produced random voltage fluctuations across its terminals, known as Johnson Noise. The RMS voltage output across the resistor's terminals without an external current source may be expressed by:

FIGURE 1. Method of Particle Detection

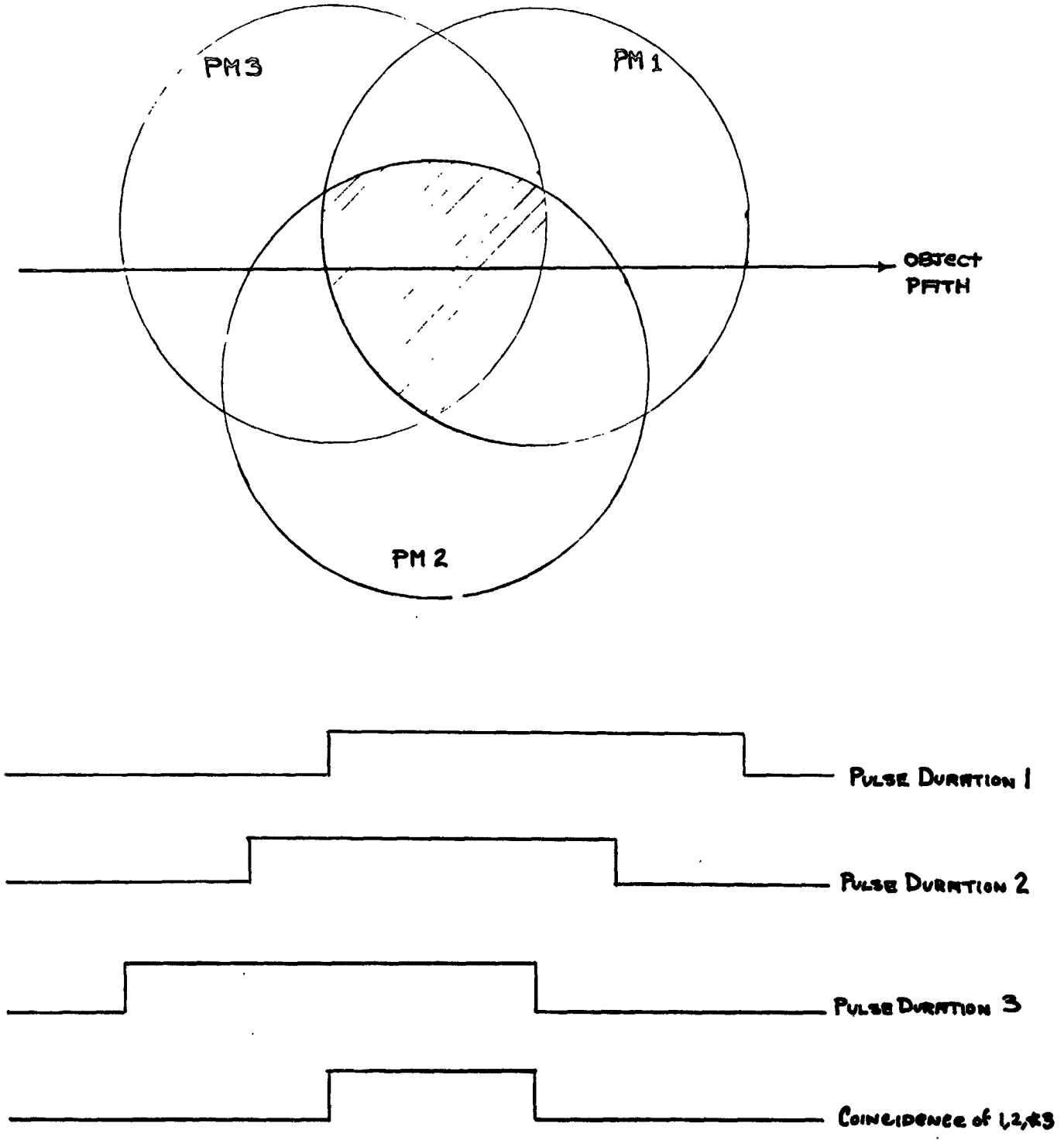

$$E_{RMS} = (4\,KCR\,\Delta F_{BW})^{1/2} \quad (1)$$

where K is the Boltzmann constant, C the temperature in degrees Kelvin, R the resistance and ΔF_{BW} the bandwidth frequency. For a sample case of 10 Megohm, 10^3 Hertz and 290° K (room temperature), the RMS voltage is

$$E_{RMS} = (4 \times 1.38 \times 10^{-23} \times 290 \times 10^6 \times 10^3)^{1/2} \cong 4 \text{ microvolts.}$$

This is well below the sensitivity of most instruments and, therefore, would have limited application. Even if the resistance and bandwidth frequency were squared and the ambient temperature raised an additional 100°C, the output E_{RMS} would only be approximately .15 volts. Consequently, the use of such a device would not be satisfactory.

The second approach to obtaining a suitable noise output resulted in the use of a photomultiplier tube (PM) as the noise source. The primary process of a PM is the absorption of quanta and the liberation of electrons. The fluctuations due to the discrete nature of this electronic charge is called Shot Noise. The RMS current from such a process may be expressed by the formula

$$I_{RMS} = 2\,e\,i\,\Delta F_{BW} \quad (2)$$

where e is 1.60×10^{-19} coulombs, i the average current, and ΔF_{BW} the bandwidth frequency. The RMS noise voltage for a PM may be defined as

$$E_{RMS} = I_{RMS} \times gain_{PM} \times R = gain_{PM} \times R \times (2\,e\,i\,\Delta F_{BW})^{1/2} \quad (3)$$

where i becomes the current found at the photocathode of the PM.

A comparison of Johnson and Shot noise may now be performed. If the $gain_{PM} = 10^6$, $i = 10^{-12}$ amperes, and the values for R, C and K from above, the Shot Noise output will be approximately 18 millivolts compared to the 4 microvolt output for Johnson Noise. This confirmed the use of a PM as a suitable noise source. The PM output was fed to a RMS voltmeter which was used both as a voltage measuring device and as an amplifier for input to the threshold circuit. Finally, it was found that only with proper shielding of the output, that is, using coaxial cables and light-tight covers, could the stray capacitances and 60 cycle noise be reduced within tolerable limits.

2. Threshold

A relatively simple threshold circuit was constructed as shown in Fig. 2. In essence, the transistors Q_1 and Q_2 act as switches. When Q_1 is on, Q_2 is

FIGURE 2. Schematic Diagram of a Threshold Circuit

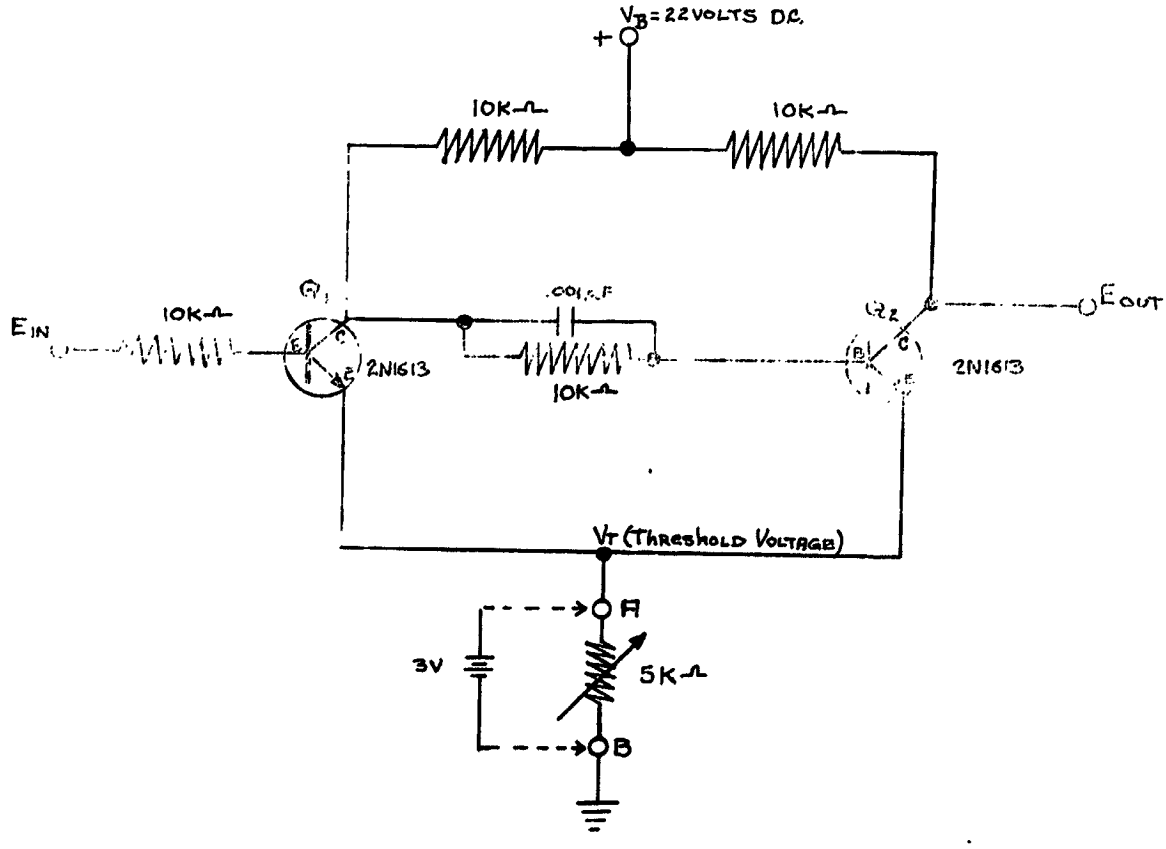

off and vice versa. The noise pulse (N) enters Q_1 at E_{in}; if $N < V_T$, Q_1 stays off while Q_2 stays on. The result is $E_{out} = V_T$. When $N \geq V_T$, Q_1 draws current to its collector, thereby turning off Q_2. This results in $E_{out} = V_B$. In other words, E_{out} will swing between V_T and V_B for a signal $N \geq V_T$. Q_2 also has the added effect of speeding up the switching rates of the threshold circuit.

In its original form, the circuit (see Fig. 2) included a 5K Ω potentiometer between terminals A and B. This potentiometer enabled the threshold V_T to be adjusted to various levels. This resistive load added an unwanted hysteresis effect thought to be of minimal importance at first.* It was found, however, that as soon as a noise pulse exceeded the threshold, the threshold would drop to a lower value, causing more noise pulses to exceed the new (lower) threshold. Also, recovery of the threshold to its normal position was inhibited. To eliminate this effect, the potentiometer was replaced by a 3 volt battery across terminals A and B. The equivalent threshold was measured to be 4 volts d. c.

3. Coincidence

To investigate coincidence of signals, as shown by Fig. 1, at least two threshold circuits, PMs and amplifiers, were needed. Design of the coincidence circuit required two diodes set in an "AND" position; that is, if one pulse from circuit 1 "and" another pulse from circuit 2 coincide, then a signal (E_c) would result). The final breadboard apparatus utilizing both threshold circuits and coincidence is shown in Fig. 3. In general, the amplitude of the coincidence signal will vary between V_T and V_B, similar to the threshold circuits.

4. Pulse Discrimination

The technique of pulse rejection can also be used in conjunction with the threshold criteria in order to reduce the false alarm problem. This method rejects all pulses which do not remain above the threshold for a preset length of time. Thus, even though a pulse satisfies the threshold criteria, it will not be accepted as legitimate unless the minimum time requirement is also satisfied.

The circuit employed to perform this rejection process is shown in Fig. 4. As can be seen from the figure, the circuit consists of two threshold circuits in series with an integrator. The integrator and the second threshold circuit make up the pulse discriminator. A noise signal entering the circuit must first satisfy the threshold criteria of circuit 1. The output of this threshold circuit is then passed on to the pulse discrimination circuit which tests the width of the pulse. If it is greater than or equal to 1/RC, the output of circuit 2 is $E_{out} = V_B$. If the pulse is too short, $E_{out} = V_T$. Thus, a false alarm will occur only if $N \geq V_T$ and the pulse width exceeds or equals 1/RC.

*In the more advanced stage of development of this system, hysteresis will be used.

FIGURE 3. Schematic Diagram of Both Threshold Circuits with Coincidence

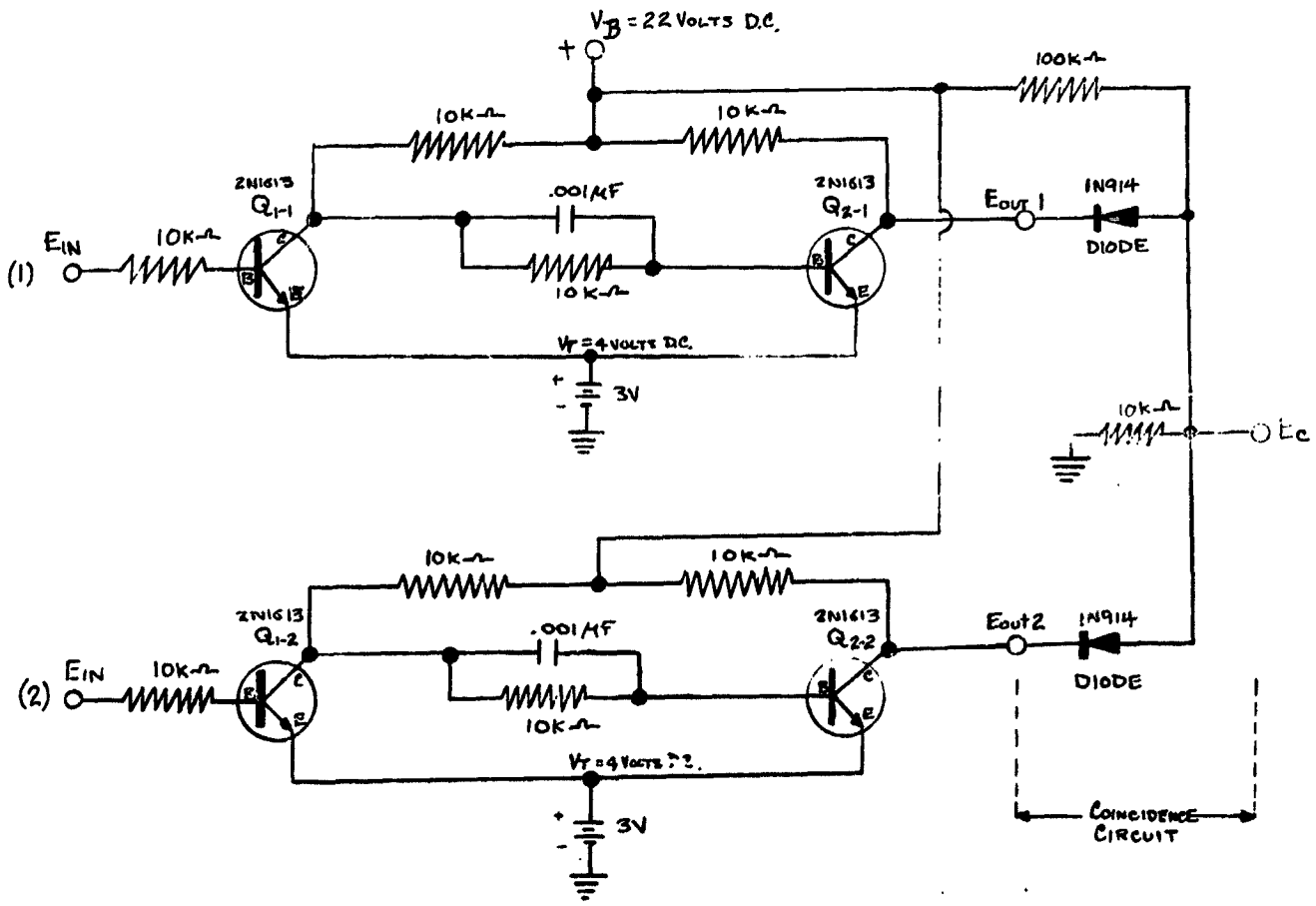

THRESHOLD CIRCUITS WITH PULSE DISCRIMINATION

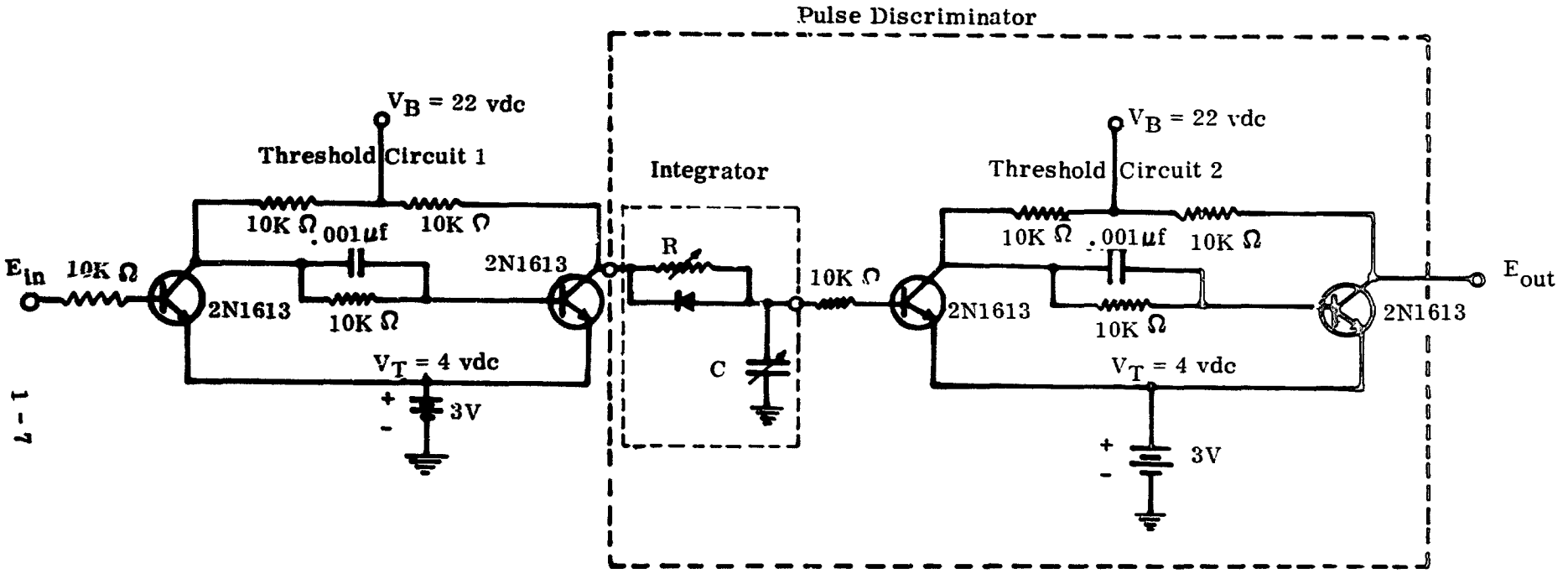

Figure 4

The probability of a false alarm can be further reduced by also requiring that the coincidence criteria be satisfied. The circuit, in this case, would be the same as that of Fig. 5 with threshold circuit 1 replaced by the coincidence circuit shown in Fig. 3.

5. Final Preparation of Equipment

The final assembly of the constructed test equipment required the addition of low level light sources to the PM windows and control of all unwanted stray light. The signal bandwidth (ΔF_{BW}) of each circuit was obtained by applying a sine wave of known amplitude at E_{in} and adjusting the input frequency until the half power point (-3 db) was reached. The noise equivalent bandwidth (ΔF_N) for a simple low pass RC circuit such as that used here may be expressed as $2\,\Delta F_{BW}$. The time constant (τ) of each circuit is given by the expression

$$\tau = 1/(2\,\pi\Delta F_{BW}) \tag{4}$$

The noise output of the PM (E_{RMS}) was amplified by the RMS volt meter. The RMS noise voltage (N) is given by the relationship

$$N = E_{RMS} \times \text{gain} \tag{5}$$

III. DISCUSSION

A. Theoretical Considerations

1. Threshold and Coincidence

The test equipment (as explained above) was designed on the principle that each time a noise signal exceeds the threshold (V_T), a false alarm pulse would occur (Fig. 5). In order to relate this concept into a useable form, the statistical fluctuations of the RMS noise voltage must be considered. The probability of detection of one false alarm is given by the Gaussian probability-density function (Ref. 4, 5).

$$P(n)\,dn = \frac{n}{N^2}\,\exp\left(-\frac{n^2}{2N^2}\right)\,dn \tag{6}$$

where "n" is the amplitude of the noise envelope and N the RMS value of the noise voltage. In order to determine the probability of a false alarm, P_{FA}, i.e., the probability of one noise pulse exceeding the threshold voltage (V_T), Eq. (6) is integrated between the limits of V_T and ∞. We now obtain

Figure 5. False Alarms Due to the Noise Voltage Exceeding Threshold

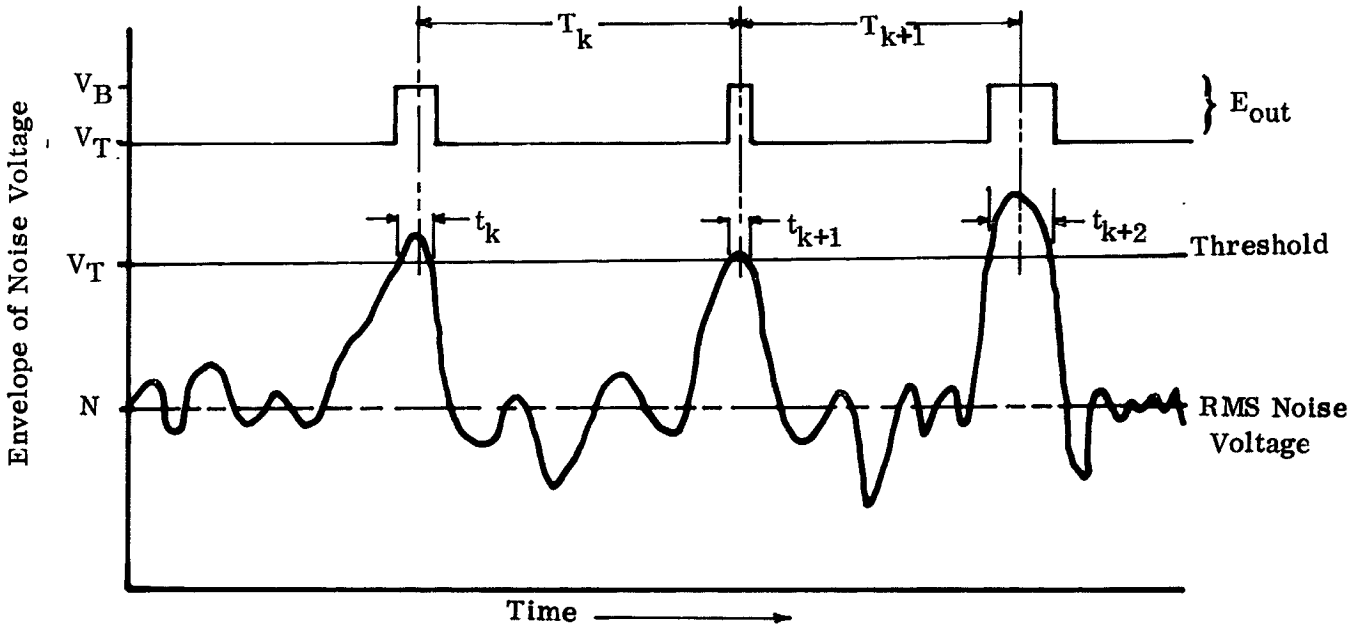

$$P_{FA} = \text{Probability } (V_T < n < \infty) = \int_{V_T}^{\infty} \frac{n}{N^2} \exp\left(-\frac{n^2}{2N^2}\right) dn$$

or

$$P_{FA} = \exp\left(-\frac{V_T^2}{2N^2}\right) \tag{7}$$

The relationship of Eq. (7) is one form of the Gaussian probability distribution, known as the Rayleigh probability distribution. The difference from the normal Gaussian is that the normalization of Eq. (6) is from V_T to ∞ and not $-\infty$ to ∞, as in the Gaussian distribution.

Substituting T (threshold voltage vdc) for V_T in Eq. (7), the final relationship, a power spectrum, is formed

$$P_{FA} = \exp\left(-\frac{1}{2}\left(\frac{T}{N}\right)^2\right) \tag{8}$$

In an earlier description (Ref. 6), T and N were defined in terms of power. Since our measurements in the laboratory will be made in terms of voltages, we shall henceforth define our threshold to noise ratio in terms of voltages. Given that ΔF_N, the noise equivalent bandwidth, defines the number of noise pulses possible per unit time, the false alarm rate (FAR) can now be obtained:

$$FAR = \Delta F_N \cdot P_{FA} = \Delta F_N \, e^{-1/2 \, (T/N)^2} \tag{9}$$

where T/N is the limiting factor in determining the FAR.

The probability of signal coincidence, given two independent circuits, may be expressed by the intersection of the two. Mathematically, it can be expressed as

$$P_c (1 \cap 2) = P_{FA} (1) \times P_{FA} (2) .$$

Therefore, Eq. (8) may be easily transformed to give

$$P_c = P_c (1 \cap 2) = e^{-1/2 \, (T/N)^2} \times e^{-1/2 \, (T/N)^2} = e^{-(T/N)^2} \tag{10}$$

To fully understand signal coincidence, the pulse shape must be considered. The actual pulse characteristics and shape duplicate a typical RC rise and decay curve. For the purpose of this discussion, since $\tau \ll 1$, the pulse will be considered rectangular; typical outputs of circuits 1 and 2 are shown in Figs. 6 and 7 (composite photograph). The outputs, as shown in Fig. 6, do not necessarily have the same pulse width. This is due to the fact that one or more pulses occurring close together could cause the threshold circuit to stay on for prolonged periods. This is especially true when $T/N \ll 1$. On the other hand, one noise pulse of high amplitude could also cause the same effect. Fig. 6-C shows the resultant or coincidence signal. The coincidence time squared (t_c^2) is just the product of the two circuits, or

$$t_c^2 = t_k \cdot t_j = (\tau_k + \epsilon_k) \cdot (\tau_j + \epsilon_j)$$

where ϵ is the signal width. Expanding, we get

$$t_c = (\tau_k \tau_j + \epsilon_k \tau_j + \epsilon_j \tau_k + \epsilon_j \epsilon_k)^{1/2} .$$

Coincidence of the signal pulses shown in Fig. 6-C can only occur when both pulses "happen to exist" at the same time. Predictions for rate of coincidence (ROC) may be readily obtained if their existence is due entirely to a random distribution. One such approach utilized DUTY CYCLE (D.C.), which may be defined as the percentage of time (t_k) a circuit is operable in contrast to the time it could have been operable (T_k). This may be written as

$$DC_1 = \frac{t_1}{T_k} \qquad \text{and} \qquad DC_2 = \frac{t_2}{T_k}$$

where the total on-time is equal to the number of pulses (N_i) times an available width τ, obtained from a given time period (T_k); therefore,

$$DC_1 = \frac{t_1}{T_k} = \frac{N_1 \tau_1}{T_k} \quad \text{and} \quad DC_2 = \frac{N_2 \tau_2}{T_k}$$

The actual percentage of on-time for a coincidence circuit is given by the product of the two duty cycles

$$DC_T = DC_1 \times DC_2 = \frac{N_1 \tau_1}{T_k} \times \frac{N_2 \tau_2}{T_k} = \frac{N_1 N_2 \tau_1 \tau_2}{T_k^2} \qquad (11)$$

Figure 6. Showing Signal Output of the Threshold Circuits with Coincidence

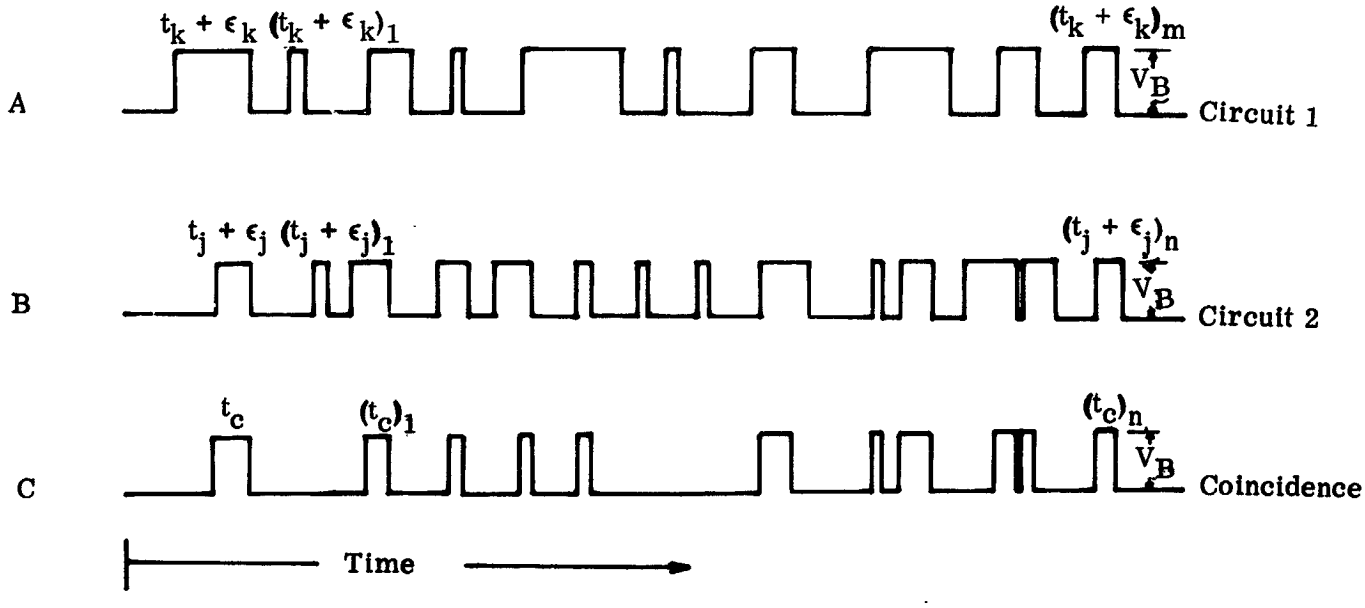

FIGURE 7. Composite Photograph Showing Typical Signal Output and Coincidence

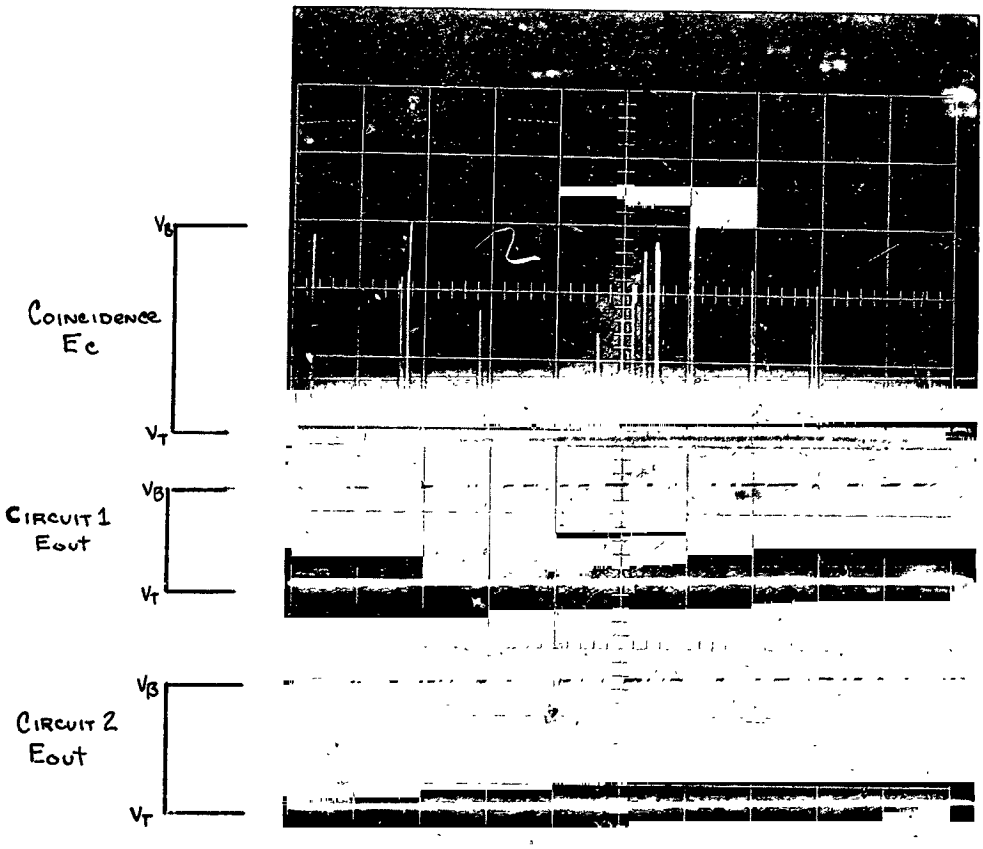

The actual ROC is then given as $ROC = DC_T/\tau$, where the τ used here must be the larger value, because the ROC should represent the minimum coincidence rate. In practice, the width of each pulse is a function of the noise amplitude and not τ (refer to Fig. 6). However, the minimum width per pulse must be at least equal to τ. Therefore, using $\tau = \tau_2$ because $\tau_2 > \tau_1$ (experimental results), we obtain

$$ROC = \frac{DC_T}{\tau_2} = \frac{N_1 N_2 \tau_1 \tau_2}{\tau_2 T_k^2} = \frac{N_1 N_2 \tau_1}{T_k^2} \qquad (12)$$

2. Threshold and Pulse Discrimination

The test equipment in this case was designed such that a false alarm pulse would occur each time the noise signal remained above the threshold for a predetermined length of time. In order to predict the false alarm rate for these conditions we must determine the probability that a noise pulse will be greater than or equal to a preset length of time and that it will also exceed the threshold.

The theory postulated is as follows. If pulses shorter than twice the time constant of the circuit are rejected, it is possible to simulate the false alarm rate of a broadband circuit by

$$FAR = \Delta F_N \, e^{-(T/N)^2} \qquad (13)$$

instead of

$$FAR = \Delta F_N \, e^{-1/2(T/N)^2} \; . \qquad (14)$$

As will be shown in the next section, the experimental results seem to verify this theory.

B. Evaluation of Results

The results of the experimental (measured) data and the theoretical (predicted) data have been compiled in Tables 1 and 2.

In comparing the results of each threshold circuit, one sees that a close correlation exists. Figs. 8 and 9 present these data in a graphical manner. The principal difference is in the slopes. It is believed that the divergence of the slopes is a function of the measured T/N ratio. The RMS noise voltage, together with the computed amplifier gain, could have been consistently too high throughout the measurement interval. The effect here would, in essence, shift the measured data and its slope upward.

TABLE ONE

EXPERIMENTAL DATA (SAMPLE SPACE 100 SECONDS)

NOISE PULSES PER SECOND

RMS NOISE VOLTAGE (MILLIVOLTS)	$(T/N)^2$	CIRCUIT NO. 1*		CIRCUIT NO. 2**		COINCIDENCES	
		PREDICTED	MEASURED	PREDICTED	MEASURED	PREDICTED	MEASURED
2.20	12.415	32.81	19.00	31.81	11.1	NA	
.40	10.432	88.46	58.00	85.74	30.9	NA	
.60	8.889	191.30	130.10	185.40	85.0	NA	
.80	7.664	353.00	252.41	342.10	177.0	.87	.71
3.00	6.676	578.50	430.01	560.70	322.0	2.71	2.10
.20	5.868	866.70	681.00	840.10	489.0	6.51	5.40
.40	5.198	1211.00	960.40	1174.00	755.0	14.20	12.00
.60	4.636	1604.00	1283.00	1555.00	1036.0	25.90	23.00
.80	4.161	2034.00	1711.00	1972.00	1410.0	47.20	44.00
4.00	3.755	2492.00	2136.00	2416.00	1650.0	68.90	55.00
.20	3.406	2967.00	2534.00	2876.00	2100.0	104.10	106.00
.40	3.103	3452.00	3050.00	3346.00	2610.0	155.70	157.00
.60	2.839	3940.00	3498.00	3819.00	2854.0	195.30	205.00
.80	2.608	4424.00	3885.00	4288.00	3298.0	250.60	270.00
5.00	2.403	4900.00	4330.00	4750.00	3840.0	325.20	346.00
.20	2.222	5365.00	4790.00	5200.00	4100.0	384.10	430.00
.40	2.060	5816.00	5290.00	5638.00	4813.0	497.90	572.00
.60	1.916	6252.00	5394.00	6061.00	4956.0	522.80	740.00
.80	1.786	6672.00	6105.00	6467.00	5201.0	621.00	875.00
6.00	1.669	7074.00	6660.00	6857.00	5453.0	710.40	1037.00
.20	1.563	7459.00	6993.00	7230.00	6113.0	835.90	NA
.40	1.467	7827.00	7134.00	7587.00	6230.0	869.20	
.60	1.379	8177.00	7300.00	7926.00	6790.0	969.50	
.80	1.299	8511.00	7850.00	8250.00	7038.0	1080.40	
7.00	1.226	8828.00	8220.00	8557.00	7387.0	1187.70	
.20	1.159	9130.00	8600.00	8849.00	7703.0	1295.60	
.40	1.097	9416.00	8850.00	9127.00	8801.0	1385.00	
.60	1.040	9688.00	9100.00	9391.00	8100.0	1441.80	
.80	.987	9947.00	9405.00	9642.00	8790.0	1617.00	
8.00	.938	10190.00	9650.00	9880.00	8805.0	1662.00	
.20	.893	10420.00	9800.00	10100.00	9023.0	1729.60	
.40	.851	10540.00	10010.00	10320.00	9400.0	1840.50	
.60	.812	10850.00	10020.00	10520.00	9629.0	1887.10	
.80	.775	11050.00	10035.00	10710.00	9930.0	1949.00	
9.00	.741	11240.00	10040.00	10900.00	10043.0	1972.20	

*FN = 16.3 kc; τ = 19.56; threshold = 4 volts dc; gain = 516

**FN = 15.8 kc; τ = 20.10; threshold = 4 volts dc; gain = 516

NA = not available

TABLE TWO

RMS NOISE VOLTAGE (MV)	$(T/N)^2$	FALSE ALARM RATE	
		PREDICTED	MEASURED
3.0	8.33	5	8
3.6	6.10	46	55
4.2	4.70	189	205
5.2	3.32	755	725
6.4	2.50	1720	1400

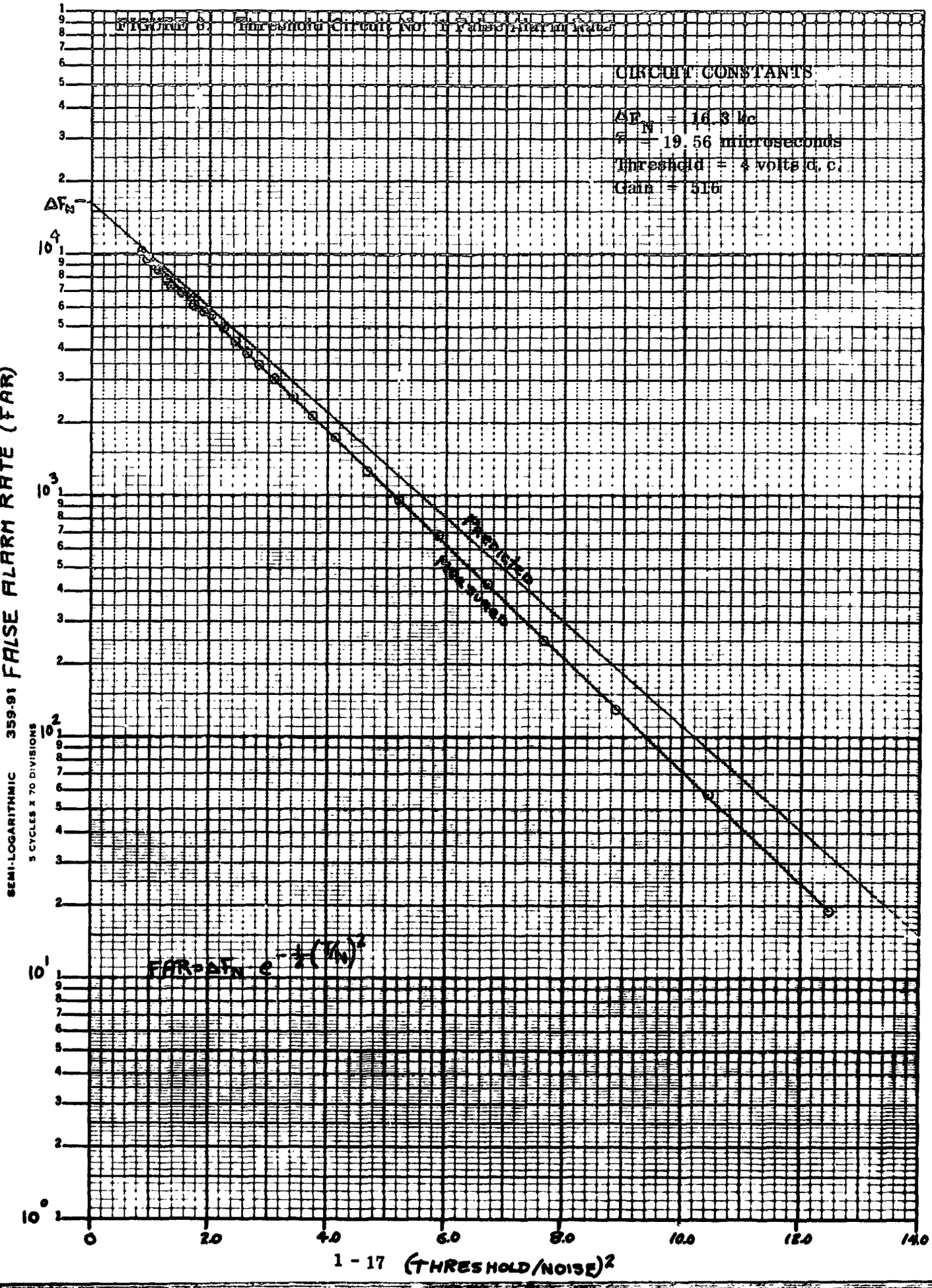
FIGURE 6. Threshold Circuit Noise False Alarm Rate
CIRCUIT CONSTANTS
ΔF_N = 16.3 kc
τ = 19.56 microseconds
Threshold = 4 volts d. c.
Gain = 516
ΔF_N
Theoretical
Measured
$FAR = \Delta F_N e^{-\frac{1}{2}\left(\frac{T}{N}\right)^2}$
FALSE ALARM RATE (FAR)
359-91
SEMI-LOGARITHMIC
5 CYCLES X 70 DIVISIONS
10^4
10^3
10^2
10^1
10^0
0
2.0
4.0
6.0
8.0
10.0
12.0
14.0
(THRESHOLD/NOISE)^2

FIGURE 11 Threshold Level vs. False Alarm Rate

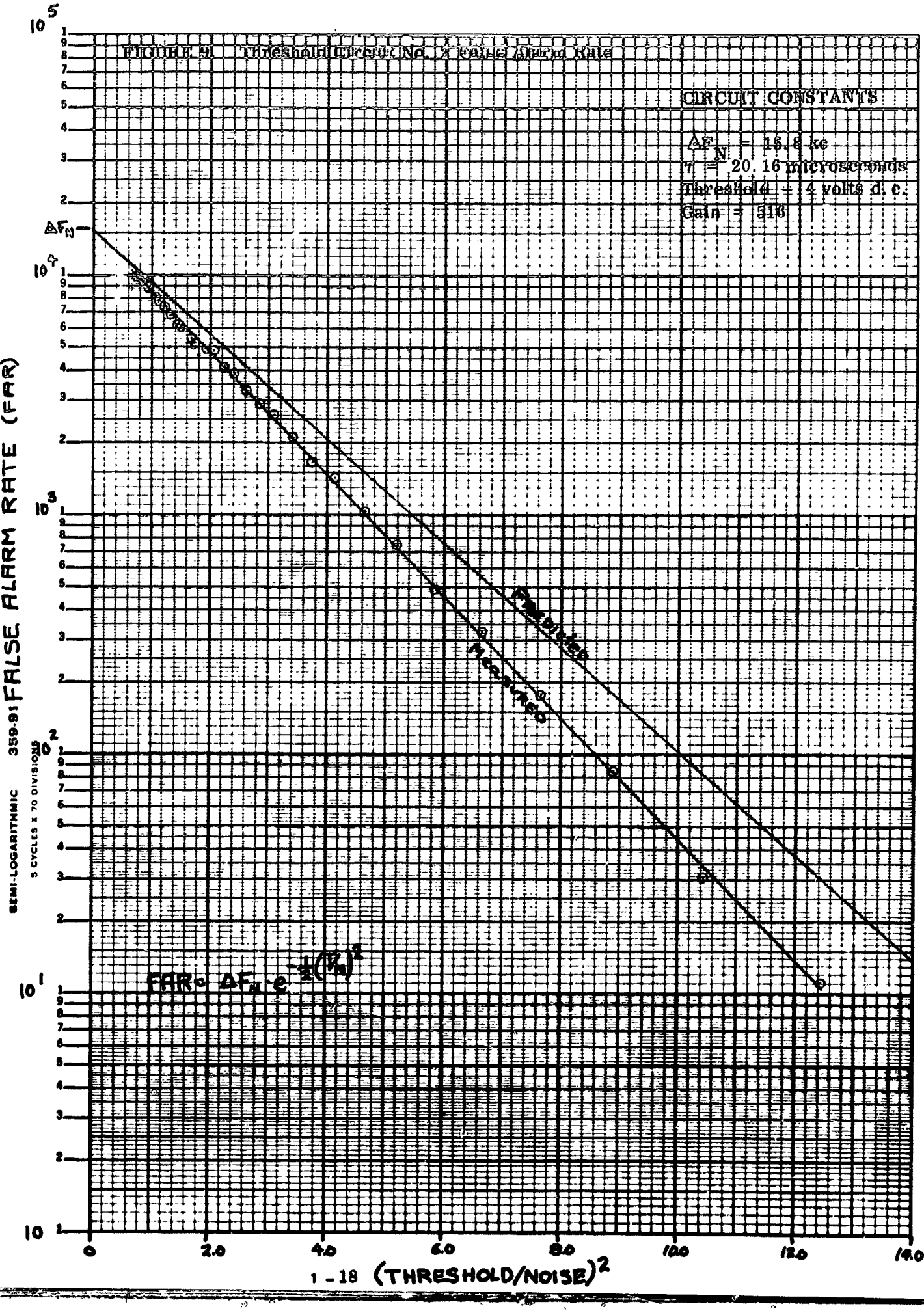

Also, the threshold (T) was found to vary somewhat under load conditions. In operation, it was found that the coincidence circuit added a small delay time to the individual threshold circuits. These subtle errors could shift the results enough so as to produce those differences obtained between the predicted and measured data. It is to be noted that predicted rates are always higher than those measured.

The measured and predicted ROC, as shown in Fig. 10, agreed satisfactorily. It appears that for very small T/N values, the percent increase in the number of coincidences declined because each circuit is in coincidence for longer periods of time. During this "coincidence time", the counter could not register new pulses. Typically, this occurs when a large amplitude noise signal coincides with several closely spaced lower amplitude signals. This counter could only sense the number of pulses and not their duration.

Figure 11 illustrates the effect of employing a pulse discrimination circuit together with the threshold circuit. The false alarm rate is reduced considerably as can be seen by comparison with Figures 8 and 9. The relatively good agreement between the predicted and measured values of FAR indicate that the theory postulated in the previous section is valid. The slight difference in slopes of the two curves illustrates the sensitivity of FAR to the value of the threshold voltage.

IV. CONCLUSIONS

The results presented in the preceding pages indicate that we can predict the effect of noise on the false alarm rate. This capability will allow us to determine the value of the threshold to noise ratio which is necessary to obtain any desired false alarm rate. This knowledge is needed in order to determine the sensitivity to which the circuit must be designed.

The next logical step in the development of the Sisyphus system is to consider the effect of noise on the measurement of transit times and differential times. These effects can be determined by superimposing noise on a signal of known width and then measuring the width of this pulse. The error in differential times, i.e., error in time between pulses, can be determined in a similar manner. This error analysis will be the subject of a separate report.

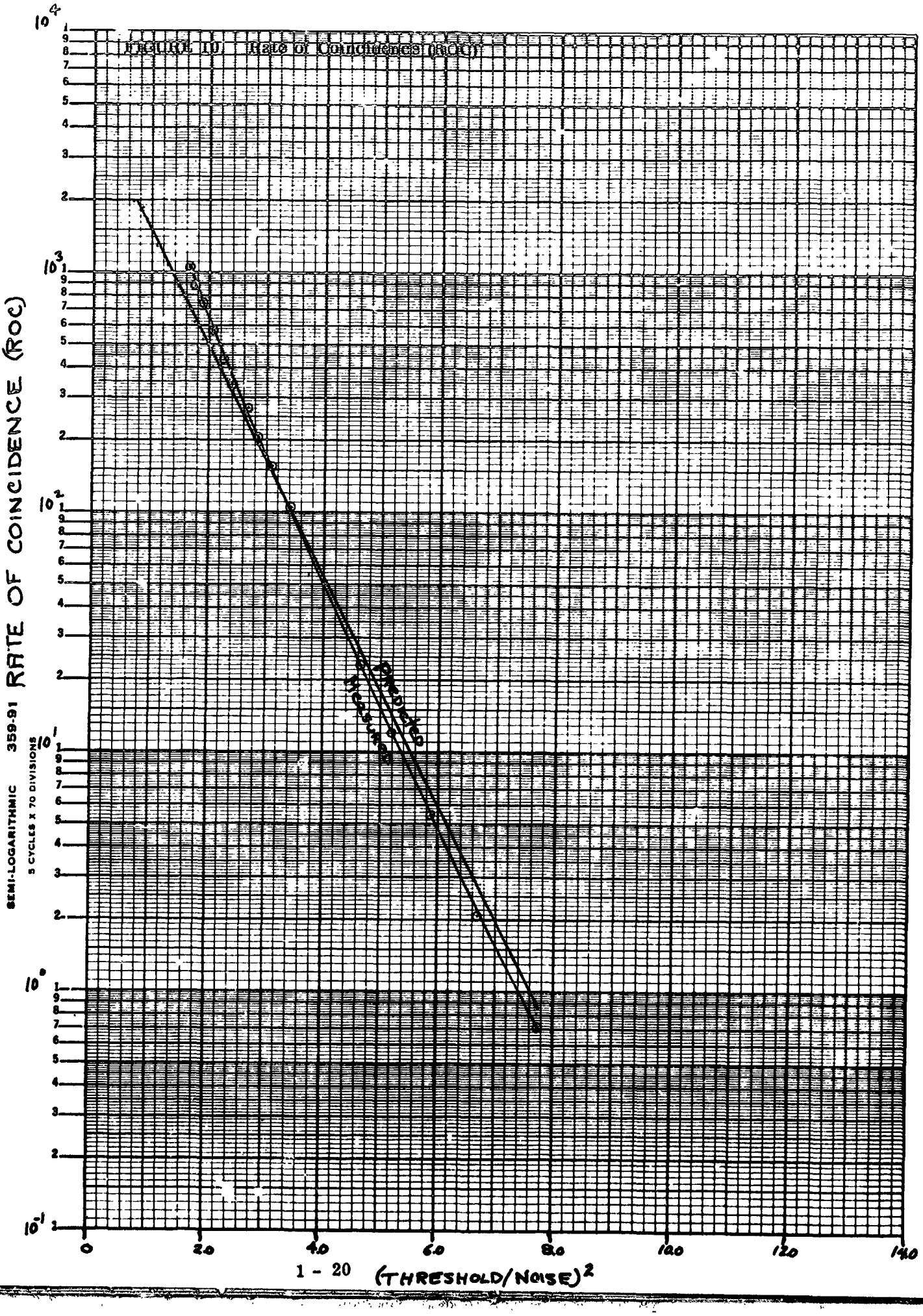
FIGURE 10 Rate of Coincidence (ROC)
RATE OF COINCIDENCE (ROC)
SEMI-LOGARITHMIC 359-91
5 CYCLES X 70 DIVISIONS
10^4
10^3
10^2
10^1
10^0
10^{-1}
0
2.0
4.0
6.0
8.0
10.0
12.0
14.0
(THRESHOLD/NOISE)^2

FALSE ALARM RATE WITH PULSE DISCRIMINATION

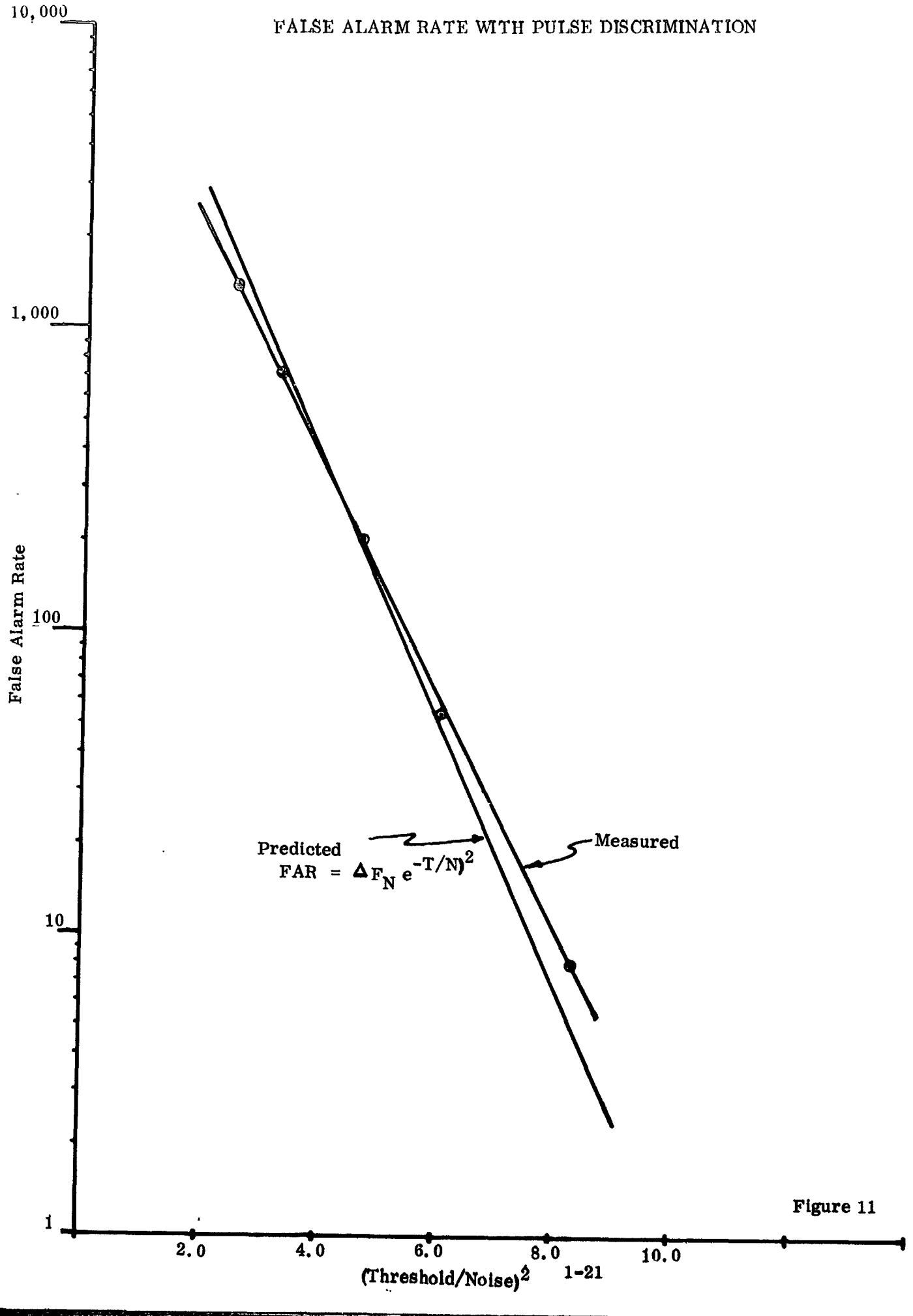

Figure 11

VI. REFERENCES

1. Skolnik, Merrill I., Introduction to Radar Systems (McGraw-Hill, New York, 1962).

2. Bissett-Berman Corp., Research on Non-Sequential Scanner for Surveillance Application, Confidential Report, 1965.

3. Faran, J. J., Jr., Random-Noise Generators, Experimenter, Vol. 42, No. 1, General Radio Co., January 1968.

4. Schwartz, Mischa, Information Transmission Modulation and Noise (McGraw-Hill, New York, 1959).

5. Skolnik, M., op cit.

6. Soberman, R. K., Meteoroid Astronomy in Deep Space and Supplement, GE Document No. N-10788, 1967.

PROJECT REPORT #2

SIGNAL AND NOISE ERROR ANALYSIS

METEOROID HAZARDS

IN

DEEP SPACE

Prepared Under

Contract NAS 9-8104
National Aeronautics & Space Administration
Manned Spacecraft Center
Houston, Texas

Prepared by: H. Chaess
S. Neste
B. Rutter
R. Soberman

Space Sciences Laboratory
Missile & Space Division
General Electric Company
PO Box 8555
Philadelphia, Pennsylvania
19101

I. INTRODUCTION

The Sisyphus Detection System obtains information concerning the range and velocity of meteoroids by measuring their transit times through the fields of view of three independent, non-imaging optical subsystems. The success of the system depends upon its ability to produce reliable values for the measured transit times. However, since the system has a finite response time and since the measurements will be made in the presence of background noise it is inevitable that the information returned will be in error to some degree. It is therefore necessary to determine the values of threshold to noise and signal to threshold which will minimize these errors and still allow an adequate amount of data to be obtained. Also, given specific values for the above parameters we must possess the ability to determine the reliability of the data returned.

The errors which should be considered are of two types, namely, the error in the pulse width and the error in the differential times between the pulses of any two subsystems. The errors will be caused by the previously mentioned factors of finite rise time and the presence of noise. An additional source of error may result if the gains of any two pulses are not equal and thus the actual differential times would be altered.

A theoretical analysis of these potential errors is presented in the following pages. For convenience and clarity, the effect of the finite response time is treated first and then the effects of noise and variable gain are added to complete the theoretical study. Experimental verification of the theoretical results is presented in the final pages.

II. THEORETICAL ANALYSIS

A. Noise-Free Considerations

1. Errors in Pulse-width

The analysis which follows assumes that an exponential rise and decay is appropriate for the pulse form, as is shown in Figure 1.

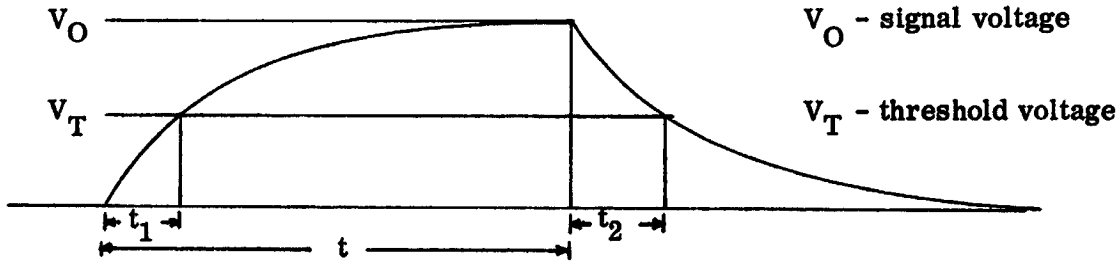

Figure 1

The time which we want to accurately determine is denoted by t. However, due to the non-zero rise-time of the circuit, the threshold voltage will not be reached at t=0 but at some later time (threshold-time) t_1. This limitation on the circuit thus causes our measured value for the lead threshold-time to be too large. Similarly, the trailing edge of the pulse will cross the threshold at a time $t + t_2$ which will also be larger than desired. The total measured width of the pulse will then be given by $t + t_2 - t_1$ which is in error by the amount $t_2 - t_1$. We must, therefore, obtain an expression for this error as a function of known variables.

If we consider the equations for the voltage as a function of time we have

$$V = V_o \left(1 - e^{-t/\tau}\right) \qquad (1)$$

from which we obtain, for the leading edge,

$$\frac{t_1}{\tau} = -\ln \left(1 - {}^{V_{T/V_o}}\right) \qquad (2)$$

where τ is the time constant of the circuit. We have the analogous expression for the trailing edge, namely,

$$\frac{t_2}{\tau} = -\ln \left({}^{V_{T/V_o}}\right). \qquad (3)$$

Subtracting Eq. (2) from Eq. (3) yields

$$\frac{t_2 - t_1}{\tau} = \ln \left(1 - {}^{V_{T/V_o}}\right) - \ln \left({}^{V_{T/V_o}}\right) \qquad (4)$$

Thus, we see that the pulse-width error is a function of the ratio (signal voltage/threshold voltage), V_o/V_T. The curves shown in Figure 2 illustrate this functional relationship. Note that the error is given in terms of the time constant, τ.

Also shown in Figure 2 is the case where the lead threshold is twice as large as the trailing threshold. This case of unequal thresholds may be used to eliminate the "dropout problem," i.e., when a signal is caused to fall below

EFFECT OF GAIN ON
MEASURED PULSE WIDTH

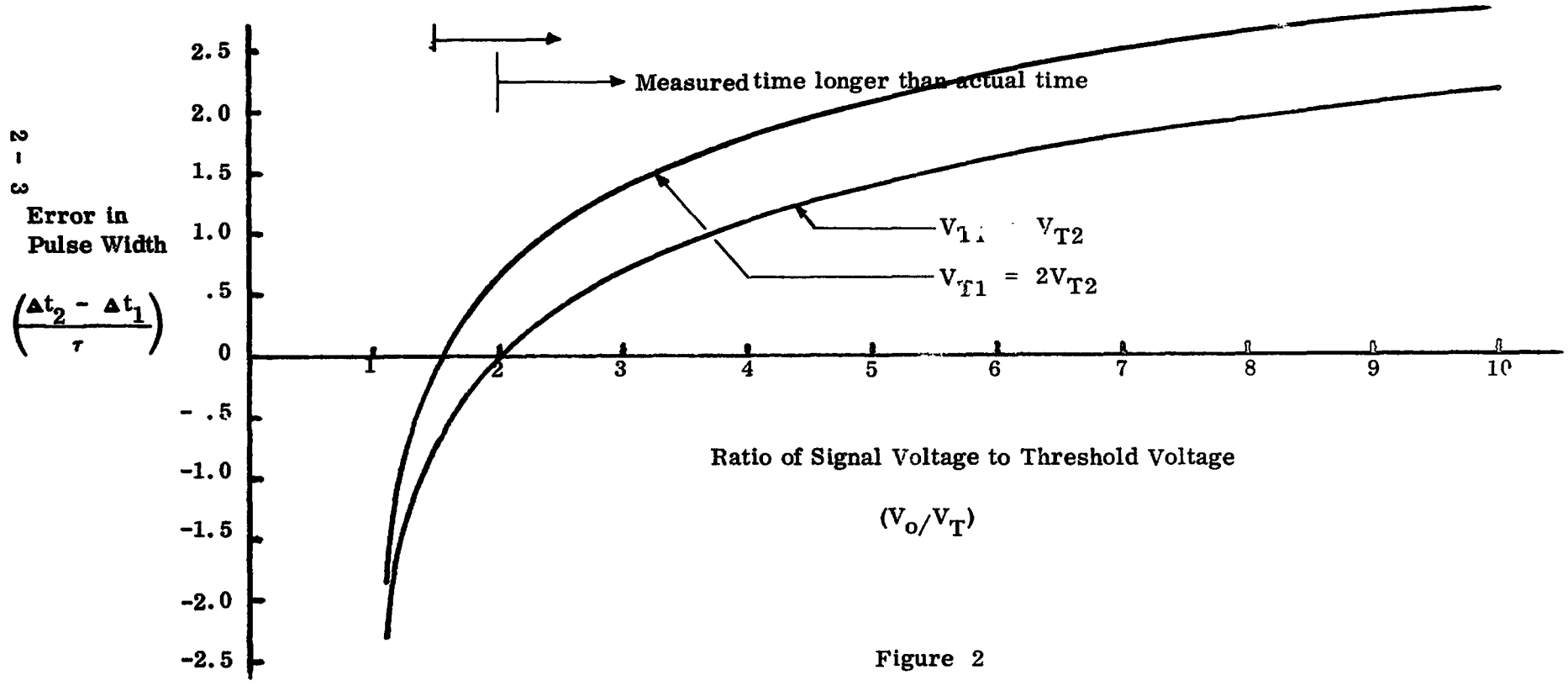

Figure 2

the threshold prematurely due to background noise. If dropout did occur the measured time for the pulse-width would be too small. Since the occurrence of "dropout" is difficult to detect and to compensate for the probability of its occurrence should be minimized.

2. Errors in Differential Times

Determination of the pulse-to-pulse error can be simplified by considering the change in threshold time produced by a variation in the gain. This difference is the error in the differential time measurements. We should, therefore, determine the change in threshold time as a function of the variation in gain. The parameters of interest are illustrated in Figure 3.

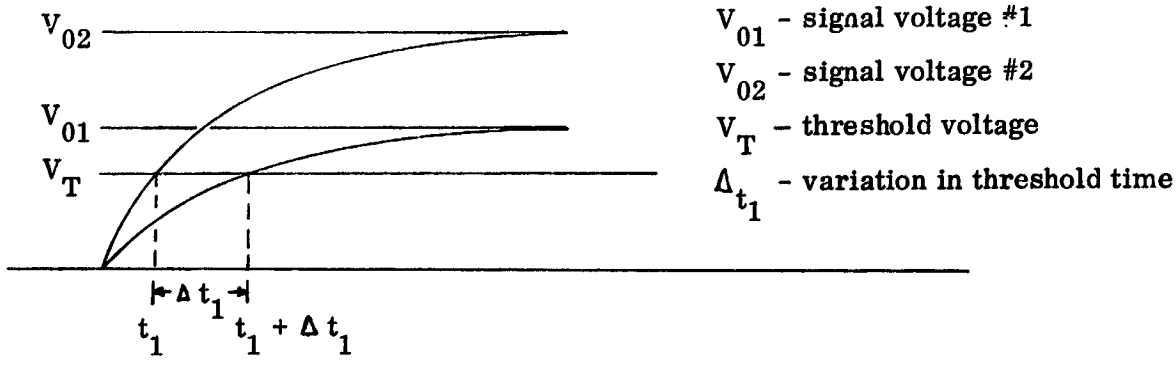

Figure 3

From Figure 3 we see that we must obtain an expression for Δt_1, (since it represents the variation in threshold-time). For any given threshold voltage, V_T, we have the expressions

$$V_T = V_{o1} (1-e^{-t_1/\tau}) \qquad (5)$$

and

$$V_T = V_{o2} (1-e^{-(t_1 + \Delta t_1)/\tau}) \qquad (6)$$

Manipulation of Eqs. (5) and (6) give us the results

EFFECT OF GAIN ON PULSE TO PULSE ERROR

Noise Voltage = 0

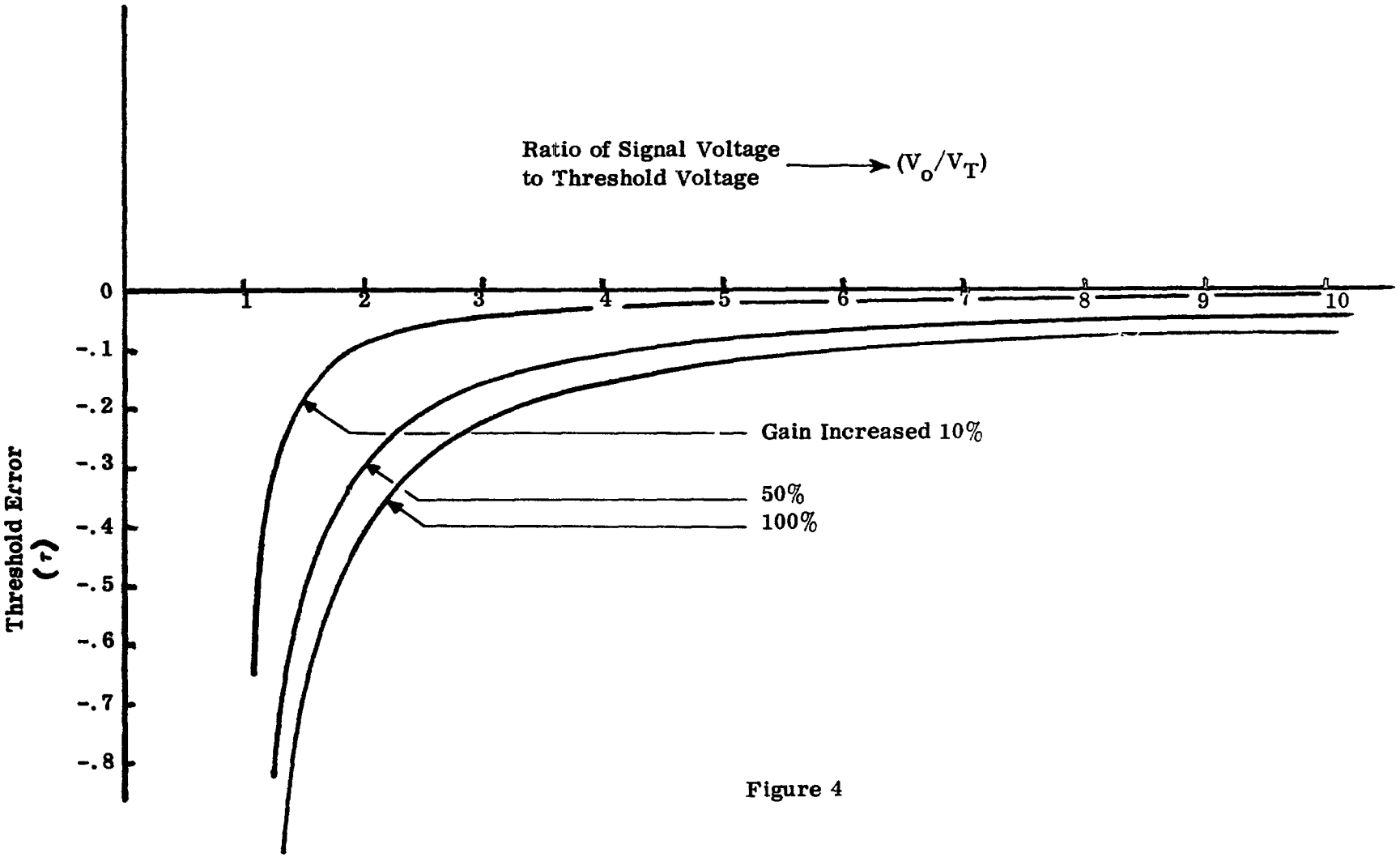

Figure 4

$$\frac{t_1}{\tau} = -\ln (1 - V_{T/V_{o1}}) \qquad (7)$$

and

$$\frac{t_1 + \Delta t_1}{\tau} = -\ln (1 - V_{T/V_{o2}}) \qquad (8)$$

Subtracting Eq. (7) from Eq. (8) provides us with the desired expression for Δt_1, namely,

$$\frac{\Delta t_1}{\tau} = \ln (1 - V_{T/V_{o1}}) - \ln (1 - V_{T/V_{o2}}). \qquad (9)$$

Thus, by varying the ratio V_{T/V_o} we can determine the behavior of Δt_1 for various values of $V_{o2/V_{o1}}$. The results of these calculations are shown by the curves in Figure 4. If we assume that $V_{o/V_T} = 2.$ is a typical value for the signal to threshold ratio, we see that a 100% variation in the gain produces an error of $.4\tau$ in the measured differential time.

B. Noise Considerations

1. Errors in Pulse Width

The previous analyses have assumed that we have been working with noise free circuits. At this point we shall consider the effect of white noise on the leading and trailing edges and thereby determine the pulse width errors.

It has been shown (Reference 1) that the noise in a circuit can be approximated by its constant rms value and added to the signal. On this basis our pulse (with noise) will be as shown in Figure 5.

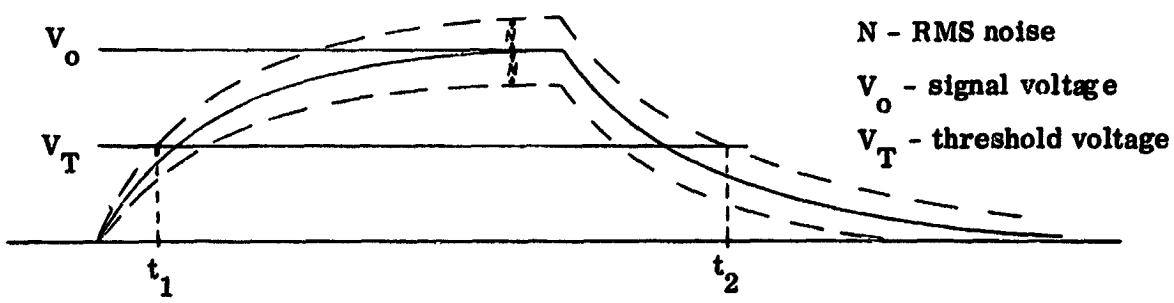

Figure 5

Our equations for the potential will thus have the form

$$V = V_o (1-e^{-t_{1/\tau}}) \pm N \qquad \text{(leading edge)} \quad (10)$$

and

$$V = V_o e^{-t_{2/\tau}} \pm N. \qquad \text{(trailing edge)} \quad (11)$$

Since we want the worst case we must use the expressions for the potentials in which the rms noise is added to both the trailing and leading edge of the pulse. Our expressions for the threshold times then become

$$\frac{t_1}{\tau} = -\ln (1- V_{T/V_o} + N/V_o) \qquad (12)$$

and

$$t_{2/\tau} = -\ln (V_{T/V_o} - N/V_o). \qquad (13)$$

Combining eqs. (12) and (13) gives us

$$\frac{t_2 - t_1}{\tau} = \ln (1- V_{T/V_o} + N/V_o) - \ln (V_{T/V_o} - N/V_o) \qquad (14)$$

as the expression for the pulse width error in the presence of noise. In Figure 6 the pulse width error in the presence of noise is shown as a function of V_o/V_T for a (threshold/noise) ratio of 5. In order to illustrate the effect of noise more clearly, the error without noise is again presented.

2. Errors in Differential Times

As before we can determine the pulse-to-pulse errors by considering only the errors in the leading edge measurements as is illustrated in Figure 7.

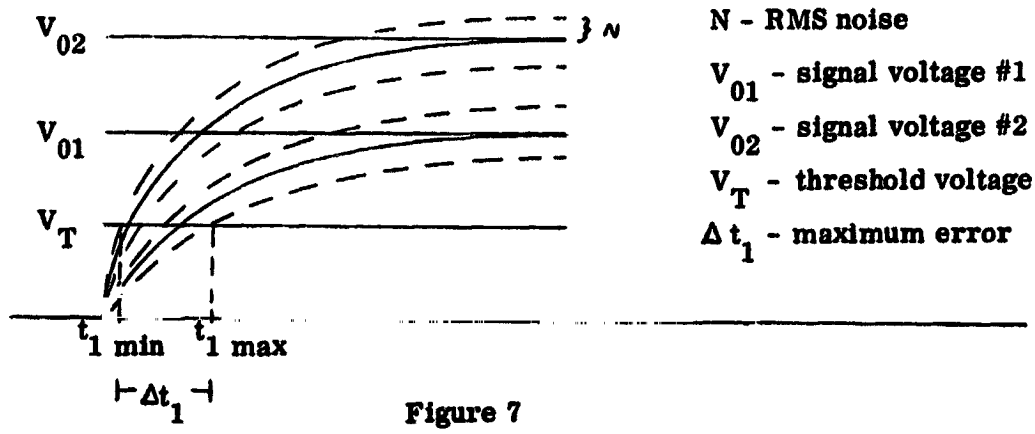

Figure 7

EFFECT OF GAIN ON MEASURED PULSE WIDTH

$$\frac{\text{Threshold Voltage}}{\text{Noise Voltage}} \left(\frac{V_T}{N}\right) = 5.0$$

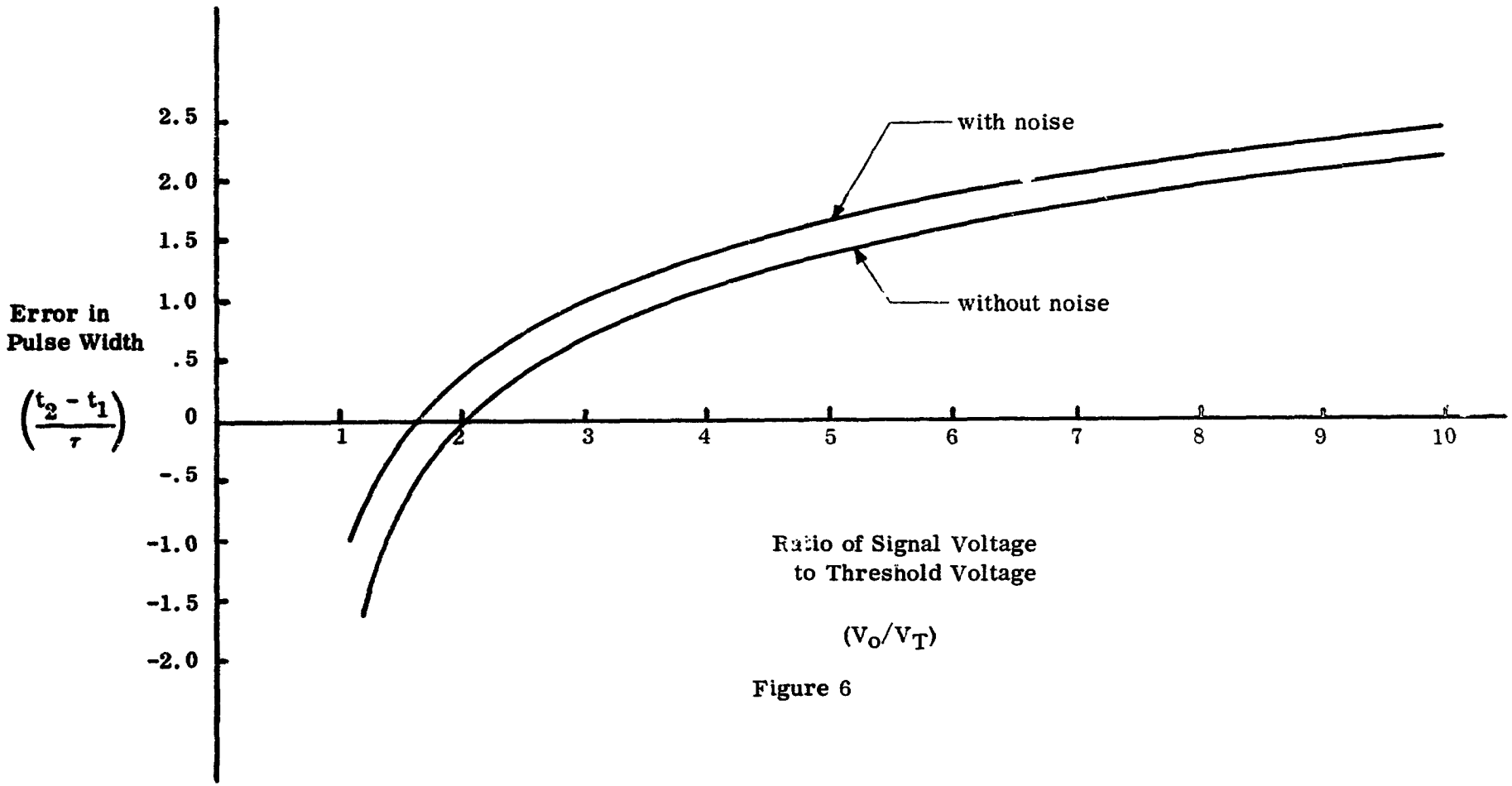

Figure 6

The quantity Δt_1 represents the maximum rms error which can occur in measuring the threshold-time. If we determine an expression for Δt_1, in Figure 7, it will represent a worst case analysis of the problem. Our expression for the potential now has the form

$$V_T = V_{o1} \left(1-e^{t_{1\,max}/\tau}\right) - N \qquad (15)$$

which yields

$$\frac{t_{1\,max}}{\tau} = -\ln \left(1- {}^{N/V_{o2}} - {}^{V_{T/V_{o1}}}\right). \qquad (16)$$

Similarly, we have

$$\frac{t_{1\,min}}{\tau} = -\ln \left(1 + {}^{N/V_{o2}} - {}^{V_{T/V_{o2}}}\right). \qquad (17)$$

Thus, the maximum rms error which could be obtained in measuring the threshold-time of a pulse with variable gain in the presence of noise is given by

$$\frac{t_{1\,max} - t_{1\,min}}{\tau} = \ln \left(1 + {}^{N/V_{o2}} - {}^{V_{T/V_{o2}}}\right) - \ln \left(1- {}^{N/V_{o1}} - {}^{V_{T/V_{o1}}}\right) \qquad (18)$$

The magnitude of this error can be examined as a function of the three ratios V_{o1}/V_{o2}, V_{T}/N, and V_{o}/V_{T}. The results of such a study are shown in Figures 8 and 9.

III. EXPERIMENTAL VERIFICATION OF THEORY

In order to determine the validity of the theoretical predictions, an electrical circuit capable of simulating actual signal to noise problems was constructed. The circuit, shown in block form in Figure 10, was essentially the same as that used previously in determining false alarm rates (FAR) for the system (Ref. 2). The only modification was the addition of a pulse generator, which provided the signal input.

The noise signal was generated by light emission to a photomultiplier tube. The output of the photomultiplier was then added to a signal from the pulse generator

EFFECT OF GAIN ON PULSE TO PULSE ERROR

$$\frac{\text{Threshold Voltage}}{\text{Noise Voltage}} \left(\frac{V_T}{N}\right) = 3$$

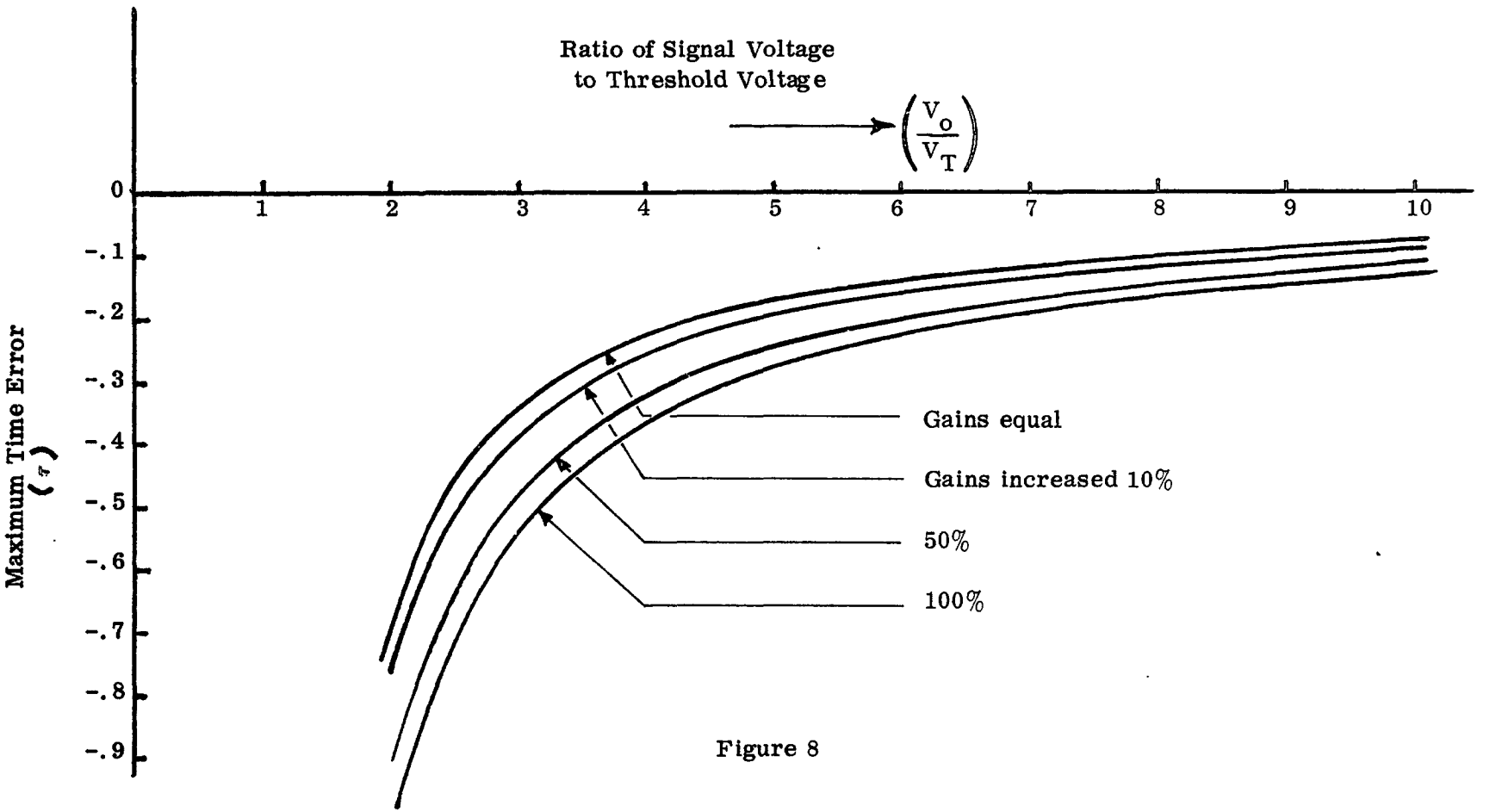

Figure 8

EFFECT OF GAIN ON
PULSE TO PULSE ERROR

$$\frac{\text{Threshold Voltage}}{\text{Noise Voltage}} \left(\frac{V_T}{N}\right) = 5$$

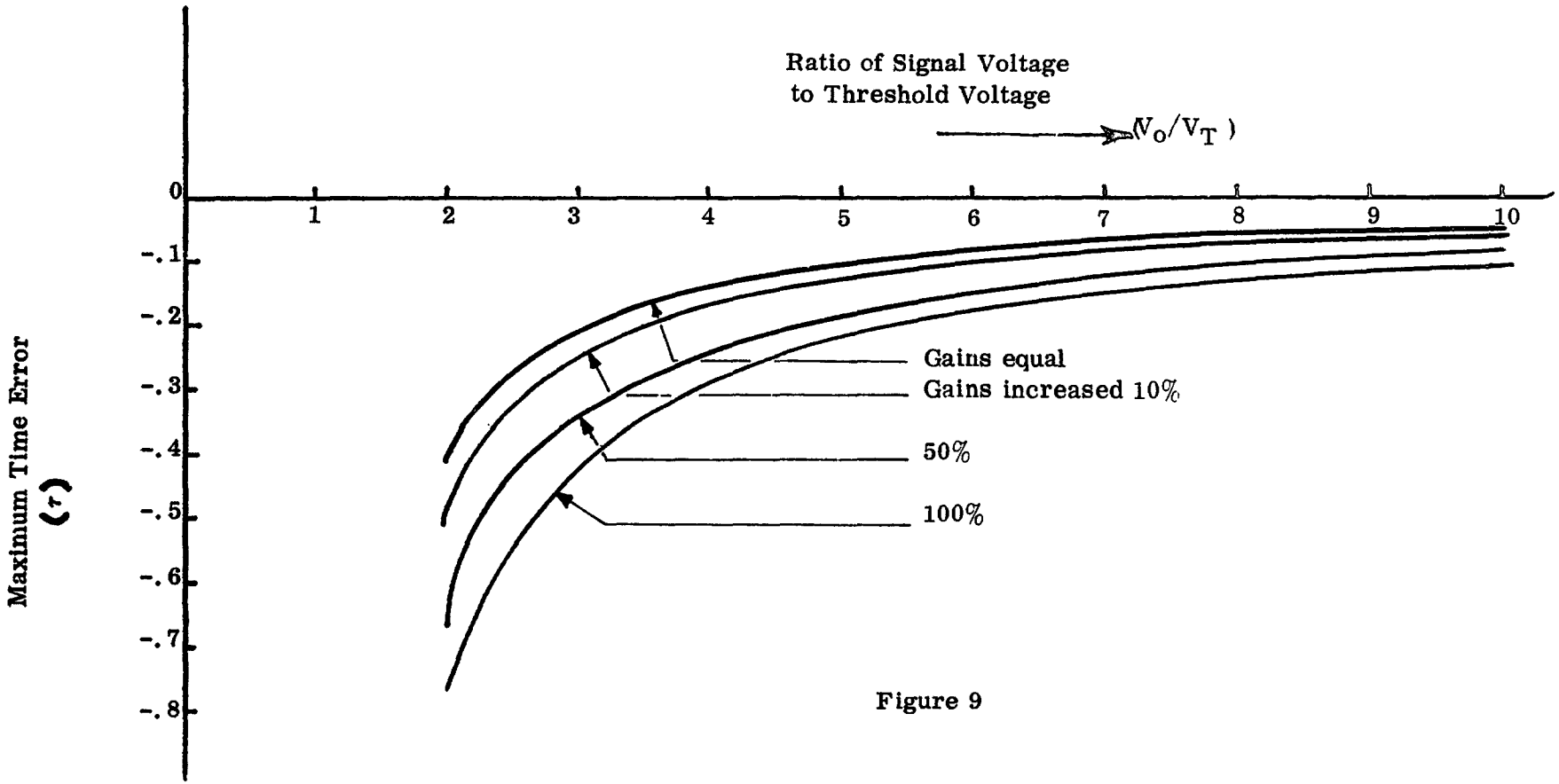

Figure 9

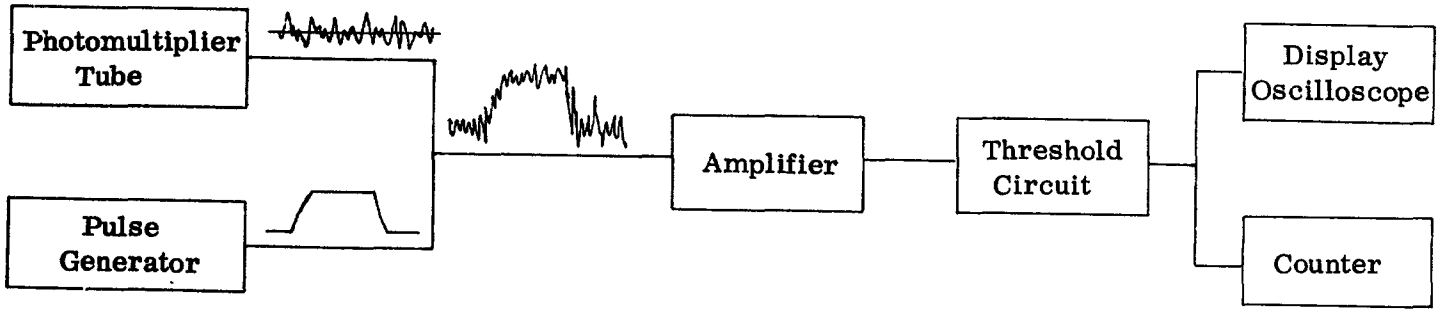
Photomultiplier Tube
Pulse Generator
Amplifier
Threshold Circuit
Display Oscilloscope
Counter

Figure 10

to produce a signal in the presence of noise. This output was then amplified and used to make the signal to noise measurements.

The threshold voltage was preset at a constant value of 4 vdc. Then by varying the rms noise voltage the ratio of (threshold/noise) could be controlled. The value of V_T/N will determine the false alarm rate as was shown in Ref. 2. It should be noted that a high V_T/N ratio corresponds to a low false alarm rate, e.g. if $V_T/N = 5$ then FAR $\simeq$ .6/sec. The value of (signal/noise) can be controlled by adjusting the amplitude of the pulse generator. It is, therefore, possible to obtain any set of conditions desired.

In order to provide experimental verification of our theoretical results we made several measurements in the most sensitive region of the curve. For each value of V_o/V_T several ($\sim$50) readings were taken for the pulse width and the standard deviation was calculated (Table 1). In this case the standard deviation is actually the deviation from the pulse-width error without noise. Thus, if these points are plotted they should fall on the theoretical curve for pulse-width error with noise. As is shown in Fig. 11, there is close agreement between the predicted and actual values. The accuracy of the theory seems to increase with larger values of V_o/V_T. The significance of Fig. 11 is that 68% of the pulse-width measurements will have errors which lie within the dashed boundaries.

Similar measurements were made for the pulse-to-pulse errors (Table 2) with the results shown in Fig. 12 for the specific value of $V_T/N = 5$. Again we see that the experimental and theoretical values are in close agreement.

PULSE WIDTH ERROR RANGE (1σ)

$$\frac{\text{Threshold Voltage}}{\text{Noise Voltage}} \left(\frac{V_T}{N}\right) = 5.0$$

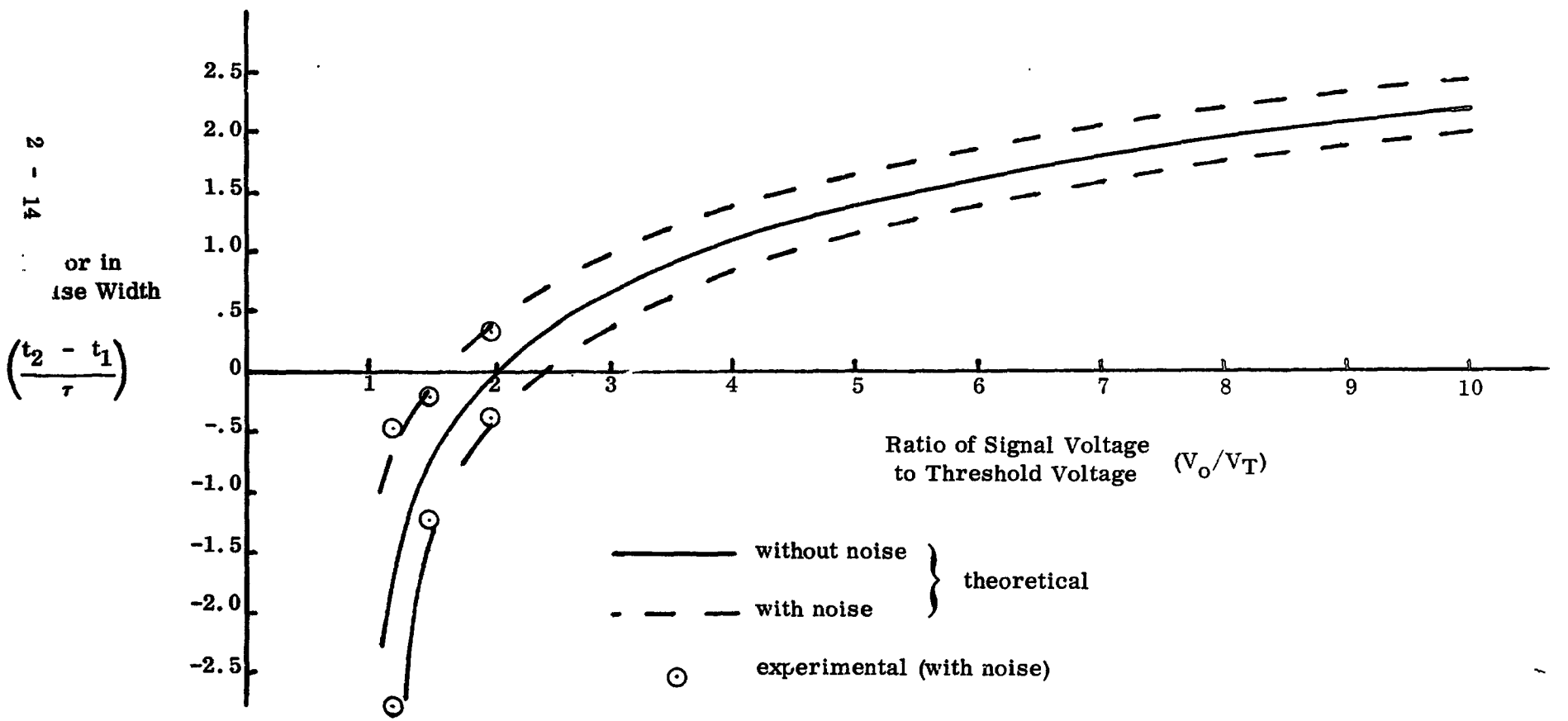

Figure 11

PULSE TO PULSE ERROR RANGE (1σ)

$$\frac{\text{Threshold Voltage}}{\text{Noise Voltage}} \left(\frac{V_T}{N}\right) = 5.0$$

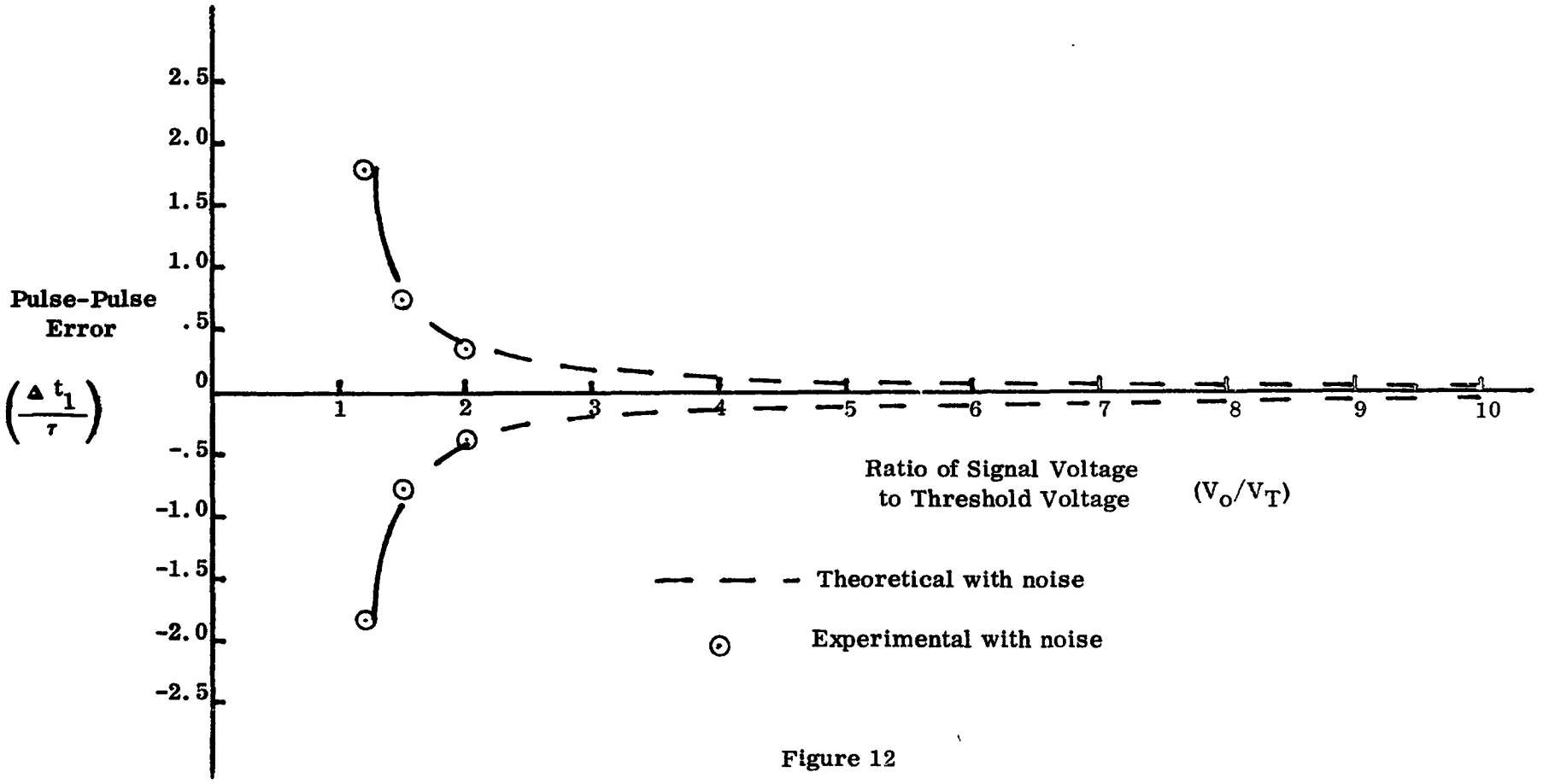

Figure 12

*TABLE 1

Pulse-width Errors

V_o/V_T (signal/threshold)	Theoretical** RMS Error	Experimental RMS Error
1.2	$1.05\tau = 15.75$ μ-sec.	17.43 μ-sec
1.5	$.55\tau = 8.25$ μ-sec.	7.64 μ-sec
2.0	$.4\tau = 6.00$ μ-sec.	5.95 μ-sec.

*TABLE 2

Pulse-to-Pulse Errors

V_o/V_T	Theoretical** RMS Error	Experimental RMS Error
1.2	-------	27.36 μ-sec.
1.5	$.85\tau = 12.75$ μ-sec	11.37 μ-sec.
2.0	$.4\tau = 6.00$ μ-sec	5.41 μ-sec.

**τ = time constant = 15μ s

*Note that (RMS Error)/τ is plotted in Figs. 11 & 12

IV. CONCLUSIONS AND SUMMARY

Although the experimental values obtained were limited in number, they were obtained for the most critical and sensitive portion of the curve. Since they correlated quite well throughout this region, it seems reasonable to assume that this close correspondence will continue for the remainder of the useable operating region.

We have therefore exhibited the capability of predicting the accuracy to which any time measurement can be made. Given the value of (threshold/noise) and (signal/threshold) it is possible to determine confidence limits on the error in the measurement. For example in Figures 11 and 12 we have shown the 68% confidence limits for the pulse-width error and pulse-to-pulse error.

The initial step in determining any error range is to define the expected false alarm rate, which in turn, will give us the (threshold/noise) ratio. It is then possible to generate the range of expected error as a function of (signal/threshold) and thus determine the reliability or accuracy of the data returned.

V. REFERENCES

1. Skolnik, M. I., Introduction to Radar Systems, pp. 462 - 465, (McGraw-Hill Book Company, Inc., New York, 1962).

2. Chaess, H., Threshold to Noise and Coincidence, Measurements for a New Meteoroid Detector, May, 1968.

PROJECT REPORT #3

THE TWO-CONE SISYPHUS SYSTEM

METEOROID HAZARDS

IN

DEEP SPACE

Prepared Under

Contract NAS 9-8104
National Aeronautics & Space Administration
Manned Spacecraft Center
Houston, Texas

Prepared by: S. Neste
W Shaffer
R. Soberman

Space Sciences Laboratory
Missile and Space Division
General Electric Company
PO Box 8555
Philadelphia, Pennsylvania
19101

THE TWO-CONE SISYPHUS SYSTEM

I. INTRODUCTION

A detailed analysis of the two-cone Sisyphus system has shown that a solution is possible only if some initial assumptions are made. Since the solution involves five unknowns (R, φ, V_1, V_2, V_3) and only three independent equations (one for each independent time measurement), no solution exists unless two of the unknowns are specified.

It is hoped that data will be available from operation prior to the failure of one subsystem. This data will allow a flux distribution to be established and will furnish knowledge of signal amplitudes. Should one subsystem then fail, the remaining two subsystems will continue to measure entrance and exit times and furnish amplitude information.

II. RANGE ERROR ANALYSIS

The range radius relationship

$$I = \frac{0.14\, r}{2} \left[\frac{a}{R}\right]^{1/2} \tag{1}$$

can be written as

$$R = \frac{a}{(I/0.07\, r)^2} \tag{2}$$

where R is the range, a the particle radius, I the incident light intensity, and r the reflectivity of the particle; an approximation to the range can be made if one assumes that the particle is of the most probable size. The intensity I is found from the signal amplitude and the photomultiplier sensitivity and gain. Using the initial and final amplitudes, reasonable bounds can be set for the axial velocity.

Let us assume for purposes of demonstration the flux of Hawkins and Upton (1958) as modified by Whipple (1963, 1967)

$$\log_{10} \Phi = -4/3 \log_{10} m - 18.3 \tag{3}$$

where Φ is the flux/cm^2/sec/2 π ster through a randomly oriented surface and m is the meteoroid mass in grams. For the Sisyphus system, the count rate as a function of mass can be written as

$$N = A\Phi = 4.3 \times 10^{-9} \frac{r D}{\rho^{2/3} s^2 (i_s/i_n)} m^{-4/3} (m^{1/3} - m_0^{1/3})^2 \tag{4}$$

or, by letting $m = x\, m_0$ with $x \geq 1$,

$$N = 4.3 \times 10^{-9} \frac{r\, D}{\rho^{2/3}\, s^2\, (i_s/i_n)}\, m_0^{-2/3}\, x^{-4/3}\, (x^{1/3} - 1)^2 \qquad (5)$$

Here, D is the system aperture in cm, ρ is the meteoroid density in gm/cm^3, s is the distance from the sun in astronomical units and (i_s/i_n) is the minimum detectable ratio of signal to noise. The minimum detectable mass is given by

$$m_0 = 8.38 \times 10^{-12}\, d^3\, \rho \left[\frac{s^2\, (i_s/i_n)}{\alpha\, r\, D} \right] \qquad (6)$$

where d is the cone separation in cm and α is the cone half-angle in degrees. The derivations of the expressions for N and m_0 are found in "Sisyphus - A New Concept in the Measurement of Meteoric Flux" by R. N. Grenda, W. A. Shaffer and R. K. Soberman.

The maximum count rate occurs at $x = 8$, or at the mass $m = 8\, m_0$. Thus, the most probable mass is $8\, m_0$, which has the most probable radius of $2\, a_0$.

Figure (1) shows a plot of count rate as a function of mass. Here, the count rate has been normalized to give $N = 1$ at its maximum. Fifty percent of the events will lie within the mass range of $2.19\, m_0$ and $82.8\, m_0$. This corresponds to particle radii of $1.30\, a_0$ and $4.36\, a_0$. Returning to equation (2), the error in the range will be, at the maximum value of R,

$$\frac{R_{max} - \bar{R}}{R} = 1.18$$

and at the minimum value

$$\frac{R_{min} - \bar{R}}{R} = 0.35 .$$

It should be noted that these values can vary considerably depending on the flux model chosen. A more reliable flux will be determined by the Sisyphus system prior to failure of one subsystem.

III. GEOMETRY AND MATHEMATICS OF THE TWO-CONE SISYPHUS

The two cones are assumed to have equal half-angles, denoted by α, parallel axes, and both apexes lying a plane perpendicular to their axes. As a matter of convention, the first cone through which the particle passes will be labelled cone 1. The other is cone 2.

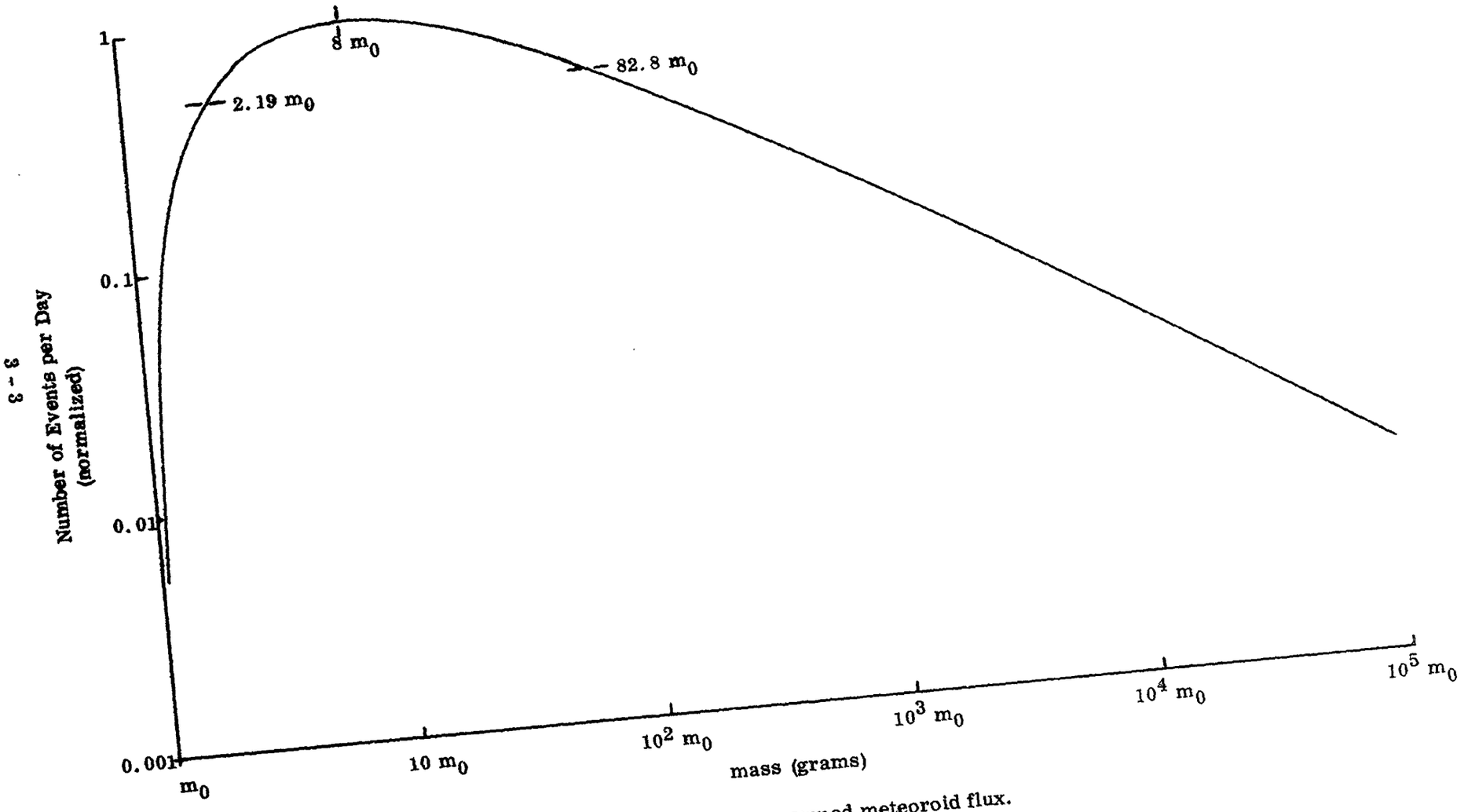

Figure 1. Sisyphus count rate vs. mass for an assumed meteoroid flux.

A right hand coordinate system is established in cone 1, as shown in Figure 2. The X_3 axis coincides with the axis of cone 1 and is positive in the direction from the apex into the field of view. The X_2 axis lies in the plane of the apexes and its positive direction is from cone 1 to cone 2, cone 2 being a distance +d from cone 1 along this axis. The X_1 axis forms a right hand orthogonal system with X_2 and X_3.

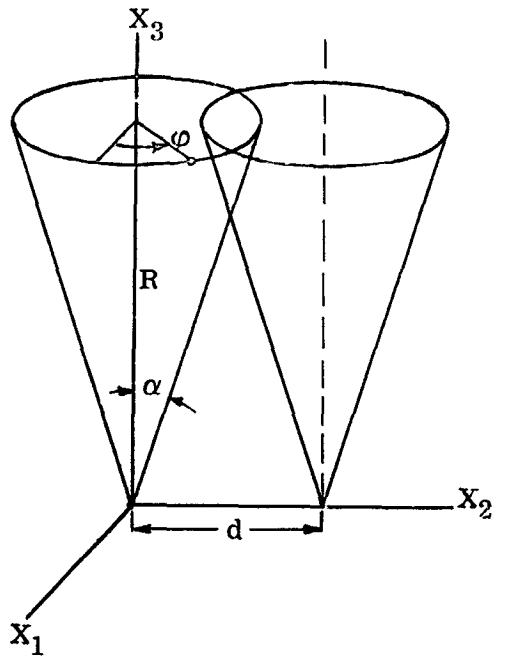

$$X_1 = R \tan \alpha \cos \varphi$$

$$X_2 = R \tan \alpha \sin \varphi$$

$$X_3 = R$$

Figure 2.

A new variable, X_{ijk}, is now defined where

i	=	1, 2, 3	for X_1, X_2, X_3
j	=	1, 2	for cone 1, 2
k	=	1	denotes an entrance point
		2	denotes an exit point

The equations of an entrance or exit point are then

$$X_{1jk} = R_{jk} \tan \alpha \cos \varphi_{jk}$$

$$X_{2jk} = R_{jk} \tan \alpha \sin \varphi_{jk} - d\ \delta_{2j}$$

$$X_{3jk} = R_{jk} \qquad ; \quad \delta_{2j} \equiv \begin{cases} 1 & j = 2 \\ 0 & j \neq 2 \end{cases} \tag{7}$$

Also, assuming constant velocity,

$$X_{ij2} = X_{ij1} + V_i (\tau_{j2} - \tau_{j1}) \tag{8}$$

where τ_{jk} is a time and V_i is the component of velocity in the i^{th} direction. In addition,

$$X_{ijk} = X_{i11} + V_i (\tau_{jk} - \tau_{11}) \qquad (9)$$

Using (9) in (7) gives

$$\begin{aligned} R_{jk} \tan\alpha \cos\varphi_{jk} &= R_{11} \tan\alpha \cos\varphi_{11} + V_1 (\tau_{jk} - \tau_{11}) \\ R_{jk} \tan\alpha \sin\varphi_{jk} &= R_{11} \tan\alpha \sin\varphi_{11} + V_2 (\tau_{jk} - \tau_{11}) - d\,\delta_{2j} \\ R_{jk} &= R_{11} + V_3 (\tau_{jk} - \tau_{11}) \end{aligned} \qquad (10)$$

Using the last equation in the first two yields

$$\begin{aligned} &\left[R_{11} + V_3 (\tau_{jk} - \tau_{11})\right] \tan\alpha \cos\varphi_{jk} \\ &\quad = R_{11} \tan\alpha \cos\varphi_{11} + V_1 (\tau_{jk} - \tau_{11}) \\ &\left[R_{11} + V_3 (\tau_{jk} - \tau_{11})\right] \tan\alpha \sin\varphi_{jk} \\ &\quad = R_{11} \tan\alpha \sin\varphi_{11} + V_2 (\tau_{jk} - \tau_{11}) - d\,\delta_{2j} \end{aligned} \qquad (11)$$

Squaring and adding yields

$$\begin{aligned} &\left[R_{11} + V_3 (\tau_{jk} - \tau_{11})\right]^2 \tan^2\alpha \\ &\quad = \left[R_{11} \tan\alpha \cos\varphi_{11} + V_1 (\tau_{jk} - \tau_{11})\right]^2 \\ &\quad + \left[R_{11} \tan\alpha \sin\varphi_{11} + V_2 (\tau_{jk} - \tau_{11}) - d\,\delta_{2j}\right]^2 \end{aligned} \qquad (12)$$

It is now convenient to let

$$\begin{aligned} d_{2j} &= -d/\tan\alpha\ \delta_{2j} \\ h_{jk} &= (\tau_{jk} - \tau_{11})/\tan\alpha \\ v_3 &= V_3 \tan\alpha \\ r &= R_{11} \\ \lambda &= \varphi_{11} \end{aligned} \qquad (13)$$

Equation (12) now becomes

$$(r + v_3 h_{jk})^2 = (r\cos\lambda + V_1 h_{jk})^2 + (r\sin\lambda + V_2 h_{jk} + d_{2j})^2 \qquad (14)$$

Squaring yields

$$h_{jk}^2 (V_1^2 + V_2^2 - v_3^2) + 2r\, h_{jk} (V_1 \cos\lambda + V_2 \sin\lambda - v_3) + 2r\, d_{2j} \sin\lambda + 2\, h_{jk}\, d_{2j}\, V_2 + d_{2j}^2 = 0 \quad (15)$$

Equation (15) is essentially three equations in three unknowns, V_1, V_2 and λ. The range and axial velocity are determined from the amplitude data as previously discussed.

For $j = 1$, $k = 2$

$$(V_1 \cos\lambda + V_2 \sin\lambda - v_3) = -\frac{h_{12}}{2r} (V_1^2 + V_2^2 - v_3^2) \quad (16)$$

Using this in equation (15) gives

$$h_{jk}^2 (V_1^2 + V_2^2 - v_3^2) - h_{12}\, h_{jk} (V_1^2 + V_2^2 - v_3^2) + 2r\, d_{2j} \sin\lambda + 2\, h_{jk}\, d_{2j}\, V_2 + d_{2j}^2 = 0$$

or

$$(h_{jk}^2 - h_{jk}\, h_{12}) (V_1^2 + V_2^2 - v_3^2) + 2r\, d_{2j} \sin\lambda + 2\, h_{jk}\, d_{2j}\, V_2 + d_{2j}^2 = 0 \quad (17)$$

When $j = 2$, $k = 1$, we have

$$(h_{21}^2 - h_{21}\, h_{12}) (V_1^2 + V_2^2 - v_3^2) + 2r\, d_{22} \sin\lambda + 2\, h_{21}\, d_{22}\, V_2 + d_{22}^2 = 0 \quad (18)$$

and when $j = k = 2$,

$$(h_{22}^2 - h_{12}\, h_{22}) (V_1^2 + V_2^2 - v_3^2) + 2r\, d_{22} \sin\lambda + 2\, h_{22}\, d_{22}\, V_2 + d_{22}^2 = 0 \quad (19)$$

Subtracting (19) from (18) yields

$$\left\{ h_{21}^2 - h_{22}^2 - h_{12} (h_{21} - h_{22}) \right\} (V_1^2 + V_2^2 - v_3^2) + 2 (h_{21} - h_{22})\, d_{22}\, V_2 = 0 \quad (20)$$

and adding gives

$$\left\{h_{21}^2 + h_{22}^2 - h_{12}(h_{21} + h_{22})\right\}(V_1^2 + V_2^2 - v_3^2)$$
$$+ 4r\, d_{22} \sin\lambda + 2(h_{21} + h_{22})\, d_{22}\, V_2 + 2 d_{22}^2 = 0 \quad (21)$$

Dividing (21) by (20) gives

$$\frac{h_{21}^2 + h_{22}^2 - h_{12}(h_{21} + h_{22})}{h_{21}^2 - h_{22}^2 - h_{12}(h_{21} - h_{22})} = \frac{4r\, d_{22} \sin\lambda + 2(h_{21} + h_{22})\, d_{22}\, V_2 + 2d_{22}^2}{2(h_{21} - h_{22})\, d_{22}\, V_2} \quad (22)$$

So

$$\sin\lambda = \frac{V_2}{2r}\left\{\frac{(h_{21} - h_{22})\left[h_{21}^2 + h_{22}^2 - h_{12}(h_{21} + h_{22})\right]}{h_{21}^2 - h_{22}^2 - h_{12}(h_{21} - h_{22})} - (h_{21} + h_{22})\right\} - \frac{d_{22}}{2r} \quad (23)$$

This reduces to

$$\sin\lambda = -\left\{\frac{V_2}{r}\,\frac{h_{21}\, h_{22}}{h_{21} + h_{22} - h_{12}} + \frac{d_{22}}{2r}\right\} \quad (24)$$

Substituting (24) into (18)

$$(h_{21}^2 - h_{21}\, h_{12})(V_1^2 + V_2^2 - v_3^2) - 2 d_{22}\left\{V_2\,\frac{h_{21}\, h_{22}}{h_{21} + h_{22} - h_{12}} + \frac{d_{22}}{2}\right\}$$
$$+ 2 h_{21}\, d_{22}\, V_2 + d_{22}^2 = 0 \quad (25)$$

which gives

$$V_1^2 = v_3^2 - V_2^2 - \frac{2 d_{22}\, V_2}{h_{21} + h_{22} - h_{12}} \quad (26)$$

Let us define

$$a = h_{21} + h_{22} - h_{12} \quad (27)$$

Then using (24) and (26) in (16) yields

$$\frac{d_{22}\, V_2\, h_{12}}{ar} = \left\{\left(v_3^2 - V_2^2 - \frac{2 d_{22}\, V_2}{a}\right)\left[1 - \left(\frac{V_2\, h_{21}\, h_{22}}{ar} + \frac{d_{22}}{2r}\right)^2\right]\right\}^{1/2}$$
$$+ V_2\left(-\frac{V_2\, h_{21}\, h_{22}}{ar} - \frac{d_{22}}{r}\right) - v_3 \quad (28)$$

or

$$V_2 \left\{ \frac{d_{22}\, h_{12}}{ar} + \frac{V_2\, h_{21}\, h_{22}}{ar} + \frac{d_{22}}{r} \right\} + v_3$$

$$= \left\{ \left(v_3^2 - V_2^2 - \frac{2\, d_{22}\, V_2}{a} \right) \left[1 - \left(\frac{V_2\, h_{21}\, h_{22}}{ar} + \frac{d_{22}}{2r} \right)^2 \right] \right\}^{1/2} \tag{29}$$

By squaring (29) and collecting like powers of V_2, we obtain, if $a \neq 0$

$$V_2^3 \left\{ \frac{2\, d_{22}\, h_{12}\, h_{21}\, h_{22}}{a^2 r^2} + \frac{d_{22}\, h_{21}\, h_{22}}{ar^2} - \frac{2\, d_{22}\, h_{21}^2\, h_{22}^2}{a^3 r^2} \right\}$$

$$+ V_2^2 \left\{ \frac{d_{22}^2\, h_{12}^2}{a^2 r^2} + \frac{3\, d_{22}^2}{4r^2} + \frac{2\, d_{22}^2\, h_{12}}{ar^2} + \frac{2\, v_3\, h_{21}\, h_{22}}{ar} \right.$$

$$\left. + \frac{v_3^2\, h_{21}^2\, h_{22}^2}{a^2 r^2} - \frac{2\, d_{22}^2\, h_{21}\, h_{22}}{a^2 r^2} + 1 \right\}$$

$$+ V_2 \left\{ \frac{2\, v_3\, d_{22}\, h_{12}}{ar} + \frac{2\, v_3\, d_{22}}{r} + \frac{v_3^2\, d_{22}\, h_{21}\, h_{22}}{ar^2} \right.$$

$$\left. + \frac{2\, d_{22}}{a} - \frac{d_{22}^3}{2\, ar^2} \right\}$$

$$+ \frac{v_3^2\, d_{22}^2}{4r^2} = 0 \tag{30}$$

The correct root of this cubic equation must be determined. The first requirement is that the velocity V_2 is real. A further restriction on V_2 can be obtained by requiring that the range r is positive.

A condition was imposed stating that the particle enters cone 1. Referring to Figure 3, where A is the plane tangent to cone 1 at P, the entrance point, and $\hat{n}$ is the unit normal of the plane directed into the cone. This condition can be written as

$$\vec{V} \cdot \hat{n} \geq 0$$

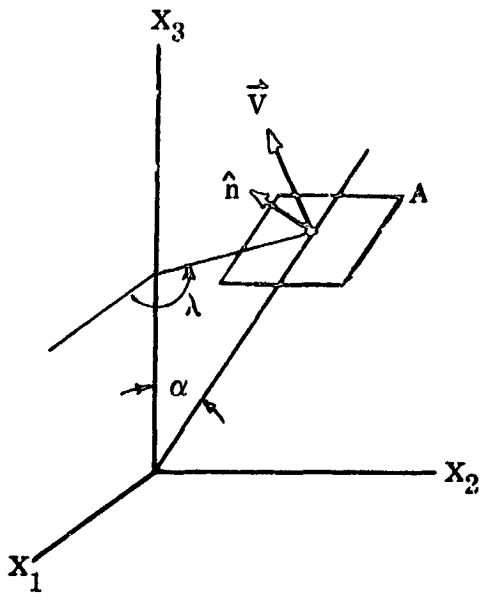

Figure 3.

Since

$$\hat{n} = -\cos\alpha\ \cos\lambda\ \hat{i} - \cos\alpha\ \sin\lambda\ \hat{j} + \sin\alpha\ \hat{k}, \tag{32}$$

we have

$$-V_1 \cos\lambda - V_2 \sin\lambda + v_3 \geq 0 \quad \text{for } \alpha \leq \pi/2 \tag{33}$$

The range is, from equation (16),

$$r = \frac{(V_1^2 + V_2^2 - v_3^2)\ h_{12}}{2\,(-V_1 \cos\lambda - V_2 \sin\lambda + v_3} = \frac{-d_{22}\ V_2/a\ h_{12}}{-V_1 \cos\lambda - V_2 \sin\lambda + v_3}$$

Since d_{22} is negative, h_{12} is positive, and, by the entrance condition, the denominator is positive, we have the further restriction that

$$\frac{V_2}{a} \geq 0 \tag{34}$$

for a positive range.

Throughout the preceeding arguments, it was assumed that $a \neq 0$. Since this quantity appears in the denominator of the expression for $\sin\lambda$ and for the cubic, let us investigate the problem when $a = 0$; that is, when

$$h_{12} = h_{21} + h_{22} \tag{35}$$

Using this in equation (12) gives

$$- h_{21}\, h_{22}\, (V_1^2 + V_2^2 - v_3^2) + 2\, r\, d_{22} \sin \lambda + 2\, h_{21}\, d_{22}\, V_2 + d_{22}^2 = 0 \tag{36}$$

and in (13) gives

$$- h_{21}\, h_{22}\, (V_1^2 + V_2^2 - v_3^2) + 2\, r\, d_{22} \sin \lambda + 2\, h_{22}\, d_{22}\, V_2 + d_{22}^2 = 0 \tag{37}$$

By equating (36) and (37), we obtain

$$h_{21}\, V_2 = h_{22}\, V_2 \tag{38}$$

So, either

$$\text{a)} \quad h_{21} = h_{22}$$
$$\text{or} \tag{39}$$
$$\text{b)} \quad V_2 = o$$

Case (a) implies that the particle enters and exits cone 2 at the same time, so the particle never enters the region of overlap between the two cones. Since equations (36) and (37) are identical if $h_{21} = h_{22}$, we have only two independent equations, (16) and (36). Thus, no solution exists for case (a).

For case (b), we can assume that $a = \epsilon$ where $\epsilon \ll h_{12}$. Then equation (24) with $V_2 = 0$ gives

$$\sin \lambda = - \frac{d_{22}}{2\, r} \tag{40}$$

Substituting $V_2 = 0$ into (36) gives

$$- h_{21}\, h_{22}\, (V_1^2 - v_3^2) + 2\, r\, d_{22} \sin \lambda + d_{22}^2 = 0 \tag{41}$$

which upon substitution of (40) gives

$$V_1^2 = v_3^2 \tag{42}$$

IV. CONCLUSIONS

The results of the foregoing analysis indicate that even if one of the Sisyphus subsystems should become inoperative, the system as a whole could still yield useful information. However, the accuracy of the data returned would depend to a large extent upon the time at which the failure occurred. If sufficient data were obtained from the three cone system so that a reliable flux rate could be established, the accuracy of the data returned after a subsystem failure would be increased. It should be noted, however, that even a complete failure of one subsystem does not preclude the success of the experiment.

PROJECT REPORT #4

SOLUTION FOR A SISYPHUS SYSTEM OF GENERALIZED GEOMETRY

METEOPOID HAZARDS

IN

DEEP SPACE

Prepared Under

Contract NAS 9-8104
National Aeronautics & Space Administration
Manned Spacecraft Center
Houston, Texas

Prepared by: **S. Neste**
W. Shaffer
R. Soberman

Space Sciences Laboratory
Missile and Space Division
General Electric Company
PO Box 8555
Philadelphia, Pennsylvania 19101

SOLUTION FOR A SISYPHUS SYSTEM OF GENERALIZED GEOMETRY

I. INTRODUCTION

The original solution for the Sisyphus system made the rather restricting assumption that the optic axes of the fields of view were exactly parallel. Since it is quite probable that the experimental package will encounter vibration, strain, and thermal variation, we must consider the possibility that the system may become misaligned. We must, therefore, possess the ability to accurately reduce any data which may be returned from such a misaligned system. This capability does now exist. The mathematical derivation and the experimental results are presented in the following pages.

II. GEOMETRICAL CONSIDERATIONS

Consider the Sisyphus system as defining three identical cones of half angle α. Let us denote the first cone entered by the particle as cone 1. If the triangle formed by the line joining the apexes is traversed in a clockwise direction as seen looking back into the detector, the next apex encountered will be designated as the apex of cone 2. The remaining cone is cone 3.

We can establish a right-hand coordinate system as shown in Figure 1. The X_2 axis lies in the plane of the apexes and joins apexes 1 and 2, being positive in the direction from 1 to 2. Axis X_1 lies in the plane of the apexes. The X_3 axis is in the general direction of the cone's view such that it forms a right-handed coordinate system with X_1 and X_2.

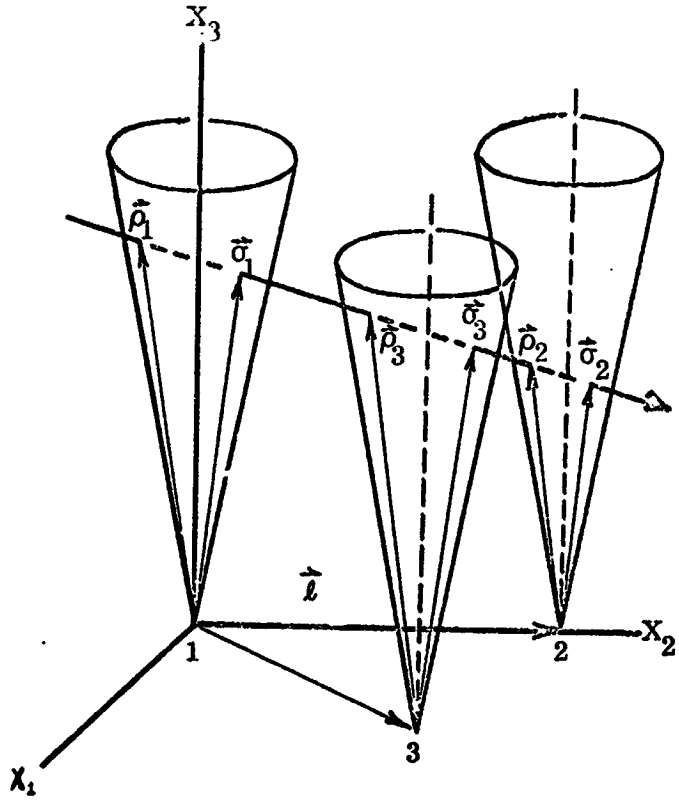

Figure 1. Sisyphus Geometry
(for convention only)

The vector from the base of the i^{th} cone to the particle's entrance into that cone is designated ρ_i and the vector to the particle's exit is σ_i. The corresponding angles of entrance and exit in the plane of the apexes are φ_i and ψ_i. Times of entrance and exit at the i^{th} cone are designated τ_{ij} where j is 1 for an entrance point and 2 for an exit point. The vector v is an arbitrary velocity vector.

Two angles are required to specify the orientation of a misaligned cone, as shown in Figure 2. The X' system of coordinates can be pictured as a rotation of the original system by γ about the X_3 axis followed by a rotation of θ about this new X_1' axis. Here, both γ and θ are positive in the counterclockwise direction. Relating the two coordinate systems, we have

$$X = AX'$$

where

$$A = \begin{pmatrix} \cos\gamma & -\cos\theta\sin\gamma & \sin\theta\sin\gamma \\ \sin\gamma & \cos\theta\cos\gamma & -\sin\theta\cos\gamma \\ 0 & \sin\theta & \cos\theta \end{pmatrix}$$

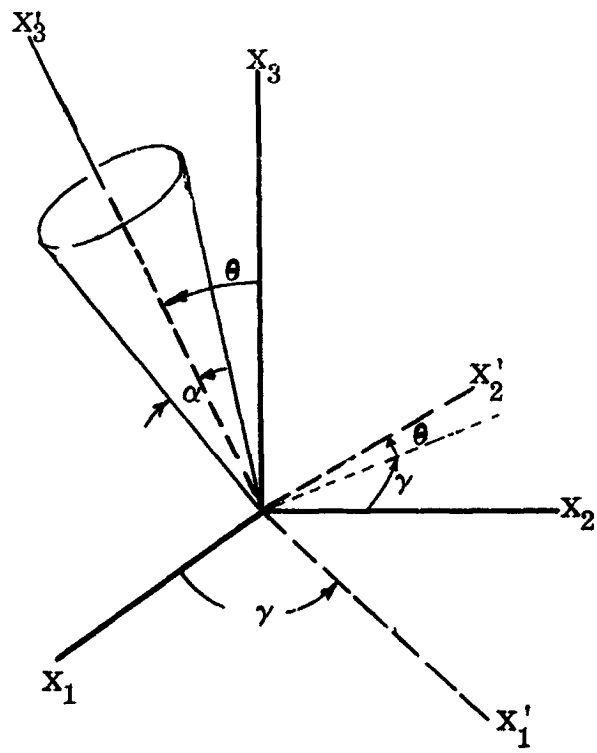

Figure 2.

III. MATHEMATICAL SOLUTION FOR THE GENERAL SYSTEM

The vector equations describing the particle's trajectory through the Sisyphus system can be written as

$$\vec{\sigma}_1 = \vec{\rho}_1 + \vec{v}\, t_{12} \qquad (1.1)$$
$$\vec{\rho}_3 = \vec{\rho}_1 + \vec{v}\, t_{31} - \vec{m} \qquad (1.2)$$
$$\vec{\sigma}_3 = \vec{\rho}_1 + \vec{v}\, t_{32} - \vec{m} \qquad (1.3)$$
$$\vec{\rho}_2 = \vec{\rho}_1 + \vec{v}\, t_{21} - \vec{\ell} \qquad (1.4)$$
$$\vec{\sigma}_2 = \vec{\rho}_1 + \vec{v}\, t_{22} - \vec{\ell} \qquad (1.5)$$

where $v = V_1 \hat{i} + V_2 \hat{j} + V_3 \hat{k}$ and t_{ij} is the time interval from the entrance into the first cone to the entrance (j = 1) or the exit (j = 2) of the i^{th} cone.

Taking components, we get the following 15 equations:

$\hat{i}$ components

$$\sigma_1 (\sin\alpha \cos\psi_1 \cos\gamma_1 - \sin\alpha \sin\psi_1 \sin\gamma_1 \cos\theta_1 + \cos\alpha \sin\gamma_1 \sin\theta_1) =$$
$$\rho_1 (\sin\alpha \cos\varphi_1 \cos\gamma_1 - \sin\alpha \sin\varphi_1 \sin\gamma_1 \cos\theta_1 + \cos\alpha \sin\gamma_1 \sin\theta_1)$$
$$+ V_1 t_{12} \qquad (2.1)$$

$$\rho_3 (\sin\alpha \cos\varphi_3 \cos\gamma_3 - \sin\alpha \sin\varphi_3 \sin\gamma_3 \cos\theta_3 + \cos\alpha \sin\gamma_3 \sin\theta_3) =$$
$$\rho_1 (\sin\alpha \cos\varphi_1 \cos\gamma_1 - \sin\alpha \sin\varphi_1 \sin\gamma_1 \cos\theta_1 + \cos\alpha \sin\gamma_1 \sin\theta_1)$$
$$+ V_1 t_{31} - m \sin\lambda \qquad (2.2)$$

$$\sigma_3 (\sin\alpha \cos\psi_3 \cos\gamma_3 - \sin\alpha \sin\psi_3 \sin\gamma_3 \cos\theta_3 + \cos\alpha \sin\gamma_3 \sin\theta_3) =$$
$$\rho_1 (\sin\alpha \cos\varphi_1 \cos\gamma_1 - \sin\alpha \sin\varphi_1 \sin\gamma_1 \cos\theta_1 + \cos\alpha \sin\gamma_1 \sin\theta_1)$$
$$+ V_1 t_{32} - m \sin\lambda \qquad (2.3)$$

$$\rho_2 (\sin\alpha \cos\varphi_2 \cos\gamma_2 - \sin\alpha \sin\varphi_2 \sin\gamma_2 \cos\theta_2 + \cos\alpha \sin\gamma_2 \sin\theta_2) =$$
$$\rho_1 (\sin\alpha \cos\varphi_1 \cos\gamma_1 - \sin\alpha \sin\varphi_1 \sin\gamma_1 \cos\theta_1 + \cos\alpha \sin\gamma_1 \sin\theta_1)$$
$$+ V_1 t_{21} \qquad (2.4)$$

$$\sigma_2 (\sin\alpha \cos\psi_2 \cos\gamma_2 - \sin\alpha \sin\psi_2 \sin\gamma_2 \cos\theta_2 + \cos\alpha \sin\gamma_2 \sin\theta_2) =$$
$$\rho_1 (\sin\alpha \cos\varphi_1 \cos\gamma_1 - \sin\alpha \sin\varphi_1 \sin\gamma_1 \cos\theta_1 + \cos\alpha \sin\gamma_1 \sin\theta_1)$$
$$+ V_1 t_{22} \qquad (2.5)$$

$\hat{j}$ components

$$\sigma_1 (\sin\alpha \cos\psi_1 \sin\gamma_1 + \sin\alpha \sin\psi_1 \cos\theta_1 \cos\gamma_1 - \cos\alpha \sin\theta_1 \cos\gamma_1) =$$
$$\rho_1 (\sin\alpha \cos\varphi_1 \sin\gamma_1 + \sin\alpha \sin\varphi_1 \cos\theta_1 \cos\gamma_1 - \cos\alpha \sin\theta_1 \cos\gamma_1)$$
$$+ V_2 t_{12} \qquad (3.1)$$

$$\rho_3 (\sin\alpha \cos\varphi_3 \sin\gamma_3 + \sin\alpha \sin\varphi_3 \cos\theta_3 \cos\gamma_3 - \cos\alpha \sin\theta_3 \cos\gamma_3) =$$
$$\rho_1 (\sin\alpha \cos\varphi_1 \sin\gamma_1 + \sin\alpha \sin\varphi_1 \cos\theta_1 \cos\gamma_1 - \cos\alpha \sin\theta_1 \cos\gamma_1)$$
$$+ V_2 t_{31} - m \cos\lambda \qquad (3.2)$$

$$\sigma_3 (\sin\alpha \cos\psi_3 \sin\gamma_3 + \sin\alpha \sin\psi_3 \cos\theta_3 \cos\gamma_3 - \cos\alpha \sin\theta_3 \cos\gamma_3) =$$
$$\rho_1 (\sin\alpha \cos\varphi_1 \sin\gamma_1 + \sin\alpha \sin\varphi_1 \cos\theta_1 \cos\gamma_1 - \cos\alpha \sin\theta_1 \cos\gamma_1)$$
$$+ V_2 t_{32} - m \cos\lambda \qquad (3.3)$$

$$\rho_2 (\sin\alpha \cos\varphi_2 \sin\gamma_2 + \sin\alpha \sin\varphi_2 \cos\theta_2 \cos\gamma_2 - \cos\alpha \sin\theta_2 \cos\gamma_2) =$$
$$\rho_1 (\sin\alpha \cos\varphi_1 \sin\gamma_1 + \sin\alpha \sin\varphi_1 \cos\theta_1 \cos\gamma_1 - \cos\alpha \sin\theta_1 \cos\gamma_1)$$
$$+ V_2 t_{21} - \ell \qquad (3.4$$

$$\sigma_2 (\sin\alpha \cos\psi_2 \sin\gamma_2 + \sin\alpha \sin\psi_2 \cos\theta_2 \cos\gamma_2 - \cos\alpha \sin\theta_2 \cos\gamma_2) =$$
$$\rho_1 (\sin\alpha \cos\varphi_1 \sin\gamma_1 + \sin\alpha \sin\varphi_1 \cos\theta_1 \cos\gamma_1 - \cos\alpha \sin\theta_1 \cos\gamma_1)$$
$$+ V_2 t_{22} - \ell \qquad (3.5)$$

k components

$$\sigma_1 (\sin\alpha \sin\psi_1 \sin\theta_1 + \cos\alpha \cos\theta_1) =$$
$$\rho_1 (\sin\alpha \sin\varphi_1 \sin\theta_1 + \cos\alpha \cos\theta_1) + V_3 t_{12} \qquad (4.1)$$

$$\rho_3 (\sin\alpha \sin\varphi_3 \sin\theta_3 + \cos\alpha \cos\theta_3) =$$
$$\rho_1 (\sin\alpha \sin\varphi_1 \sin\theta_1 + \cos\alpha \cos\theta_1) + V_3 t_{31} \qquad (4.2)$$

$$\sigma_3 (\sin\alpha \sin\psi_3 \sin\theta_3 + \cos\alpha \cos\theta_3) =$$
$$\rho_1 (\sin\alpha \sin\varphi_1 \sin\theta_1 + \cos\alpha \cos\theta_1) + V_3 t_{32} \qquad (4.3)$$

$$\rho_2 (\sin\alpha \sin\varphi_2 \sin\theta_2 + \cos\alpha \cos\theta_2) =$$
$$\rho_1 (\sin\alpha \sin\varphi_1 \sin\theta_1 + \cos\alpha \cos\theta_1) + V_3 t_{21} \qquad (4.4)$$

$$\sigma_2 (\sin\alpha \cos\psi_2 \sin\theta_2 + \cos\alpha \cos\theta_2) =$$
$$\rho_1 (\sin\alpha \sin\varphi_1 \sin\theta_1 + \cos\alpha \cos\theta_1) + V_3 t_{22} \qquad (4.5)$$

Multiplying equations (2.1) by $\cos\gamma_1$ and (3.1) by $\sin\gamma_1$ and adding, we obtain

$$\sigma_1 \sin\alpha \cos\psi_1 = \rho_1 \sin\alpha \cos\varphi_1 + V_1 t_{12} \cos\gamma_1 + V_2 t_{12} \sin\gamma_1 \qquad (5.1)$$

$$\rho_3 \sin\alpha \cos\varphi_3 = \rho_1 [\sin\alpha \cos\varphi_1 \cos(\gamma_1 - \gamma_3)$$
$$- \sin\alpha \sin\varphi_1 \cos\theta_1 \sin(\gamma_1 - \gamma_3) + \cos\alpha \sin\theta_1 \sin(\gamma_1 - \gamma_3)]$$
$$+ t_{31} (V_1 \cos\gamma_3 + V_2 \sin\gamma_3) - m (\sin\lambda \cos\gamma_3 + \sin\gamma_3 \cos\lambda) \qquad (5.2)$$

$$\sigma_3 \sin\alpha \cos\psi_3 = \rho_1 [\sin\alpha \cos\varphi_1 \cos(\gamma_1 - \gamma_3)$$
$$- \sin\alpha \sin\varphi_1 \cos\theta_1 \sin(\gamma_1 - \gamma_3) + \cos\alpha \sin\theta_1 \sin(\gamma_1 - \gamma_3)]$$
$$+ t_{32} (V_1 \cos\gamma_3 + V_2 \sin\gamma_3) - m (\sin\lambda \cos\gamma_3 + \sin\gamma_3 \cos\lambda) \qquad (5.3)$$

$$\rho_2 \sin\alpha \cos\varphi_2 = \rho_1 [\sin\alpha \cos\varphi_1 \cos(\gamma_1 - \gamma_2)$$
$$- \sin\alpha \sin\varphi_1 \cos\theta_1 \sin(\gamma_1 - \gamma_2) + \cos\alpha \sin\theta_1 \sin(\gamma_1 - \gamma_2)]$$
$$+ t_{21} (V_1 \cos\gamma_2 + V_2 \sin\gamma_2) - \ell \sin\gamma_2 \qquad (5.4)$$

$$\sigma_2 \sin\alpha \cos\psi_2 = \rho_1 [\sin\alpha \cos\varphi_1 \cos(\gamma_1 - \gamma_2)$$
$$- \sin\alpha \sin\varphi_1 \cos\theta_1 \sin(\gamma_1 - \gamma_2) + \cos\alpha \sin\theta_1 \sin(\gamma_1 - \gamma_2)]$$
$$+ t_{22} (V_1 \cos\gamma_2 + V_2 \sin\gamma_2) - \ell \sin\gamma_2 \qquad (5.5)$$

Now, multiply (2.1) by $(-\sin\gamma_1)$ and (3.1) by $\cos\gamma_1$ etc., and add:

$$\sigma_1 (\sin\alpha \sin\psi_1 \cos\theta_1 - \cos\alpha \sin\theta_1) =$$
$$\rho_1 (\sin\alpha \sin\varphi_1 \cos\theta_1 - \cos\alpha \sin\theta_1) - t_{12} (V_1 \sin\gamma_1 - V_2 \cos\gamma_1) \quad (6.1)$$

$$\rho_3 (\sin\alpha \sin\varphi_3 \cos\theta_3 - \cos\alpha \sin\theta_3) =$$
$$\rho_1 [\sin\alpha \cos\varphi_1 \sin(\gamma_1 - \gamma_3) + \sin\alpha \sin\varphi_1 \cos\theta_1 \cos(\gamma_1 - \gamma_3)$$
$$- \cos\alpha \sin\theta_1 \cos(\gamma_1 - \gamma_3)] - t_{31} (V_1 \sin\gamma_3 - V_2 \cos\gamma_3)$$
$$+ m (\sin\lambda \sin\gamma_3 - \cos\lambda \cos\gamma_3) \quad (6.2)$$

$$\sigma_3 (\sin\alpha \sin\psi_3 \cos\theta_3 - \cos\alpha \sin\theta_3) =$$
$$\rho_1 [\sin\alpha \cos\varphi_1 \sin(\gamma_1 - \gamma_3) + \sin\alpha \sin\varphi_1 \cos\theta_1 \cos(\gamma_1 - \gamma_3)$$
$$- \cos\alpha \sin\theta_1 \cos(\gamma_1 - \gamma_3)] - t_{32} (V_1 \sin\gamma_3 - V_2 \cos\gamma_3)$$
$$+ m (\sin\lambda \sin\gamma_3 - \cos\lambda \cos\gamma_3) \quad (6.3)$$

$$\rho_2 (\sin\alpha \sin\varphi_2 \cos\theta_2 - \cos\alpha \sin\theta_2) =$$
$$\rho_1 [\sin\alpha \cos\varphi_1 \sin(\gamma_1 - \gamma_2) + \sin\alpha \sin\varphi_1 \cos\theta_1 \cos(\gamma_1 - \gamma_2)$$
$$- \cos\alpha \sin\theta_1 \cos(\gamma_1 - \gamma_2)] - t (V_1 \sin\gamma_2 - V_2 \cos\gamma_2)$$
$$- \ell \cos\gamma_2 \quad (6.4)$$

$$\sigma_2 (\sin\alpha \cos\psi_2 \cos\theta_2 - \cos\alpha \sin\theta_2) =$$
$$\rho_1 [\sin\alpha \cos\varphi_1 \sin(\gamma_1 - \gamma_2) + \sin\alpha \sin\varphi_1 \cos\theta_1 \cos(\gamma_1 - \gamma_2)$$
$$- \cos\alpha \sin\theta_1 \cos(\gamma_1 - \gamma_2)] - t_{22} (V_1 \sin\gamma_2 - V_2 \cos\gamma_2)$$
$$- \ell \cos\gamma_2 \quad (6.5)$$

Multiplying (4.1) by $\sin\theta_1$ and adding it to (6.1) multiplied by $\cos\theta_1$, etc. yields

$$\sigma_1 \sin\alpha \sin\psi_1 = \rho_1 \sin\alpha \sin\varphi_1 - t_{12} (V_1 \sin\gamma_1 - V_2 \cos\gamma_1) \cos\theta_1$$
$$+ V_3 t_{12} \sin\theta_1 \quad (7.1)$$

$$\rho_3 \sin\alpha \sin\varphi_3 = \rho_1 [\sin\alpha \cos\varphi_1 \sin(\gamma_1 - \gamma_3) \cos\theta_3$$
$$+ \sin\alpha \sin\varphi_1 (\sin\theta_1 \sin\theta_3 + \cos\theta_1 \cos\theta_3 \cos(\gamma_1 - \gamma_3)$$
$$+ \cos\alpha (\cos\theta_1 \sin\theta_3 - \sin\theta_1 \cos\theta_3 \cos(\gamma_1 - \gamma_3)]$$
$$- t_{31} [(V_1 \sin\gamma_3 - V_2 \cos\gamma_3) \cos\theta_3 - V_3 \sin\theta_3]$$
$$+ m \cos\theta_3 (\sin\lambda \sin\gamma_3 - \cos\gamma_3 \cos\lambda) \quad (7.2)$$

$$\sigma_3 \sin\alpha \sin\psi_3 = \rho_1 [\sin\alpha \cos\varphi_1 \sin(\gamma_1 - \gamma_3) \cos\theta_3$$
$$+ \sin\alpha \sin\varphi_1 (\sin\theta_1 \sin\theta_3 + \cos\theta_1 \cos\theta_3 \cos(\gamma_1 - \gamma_3))$$
$$+ \cos\alpha (\cos\theta_1 \sin\theta_3 - \sin\theta_1 \cos\theta_3 \cos(\gamma_1 - \gamma_3))]$$
$$- t_{32} [(V_1 \sin\gamma_3 - V_2 \cos\gamma_3) \cos\theta_3 - V_3 \sin\theta_3]$$
$$+ m \cos\theta_3 (\sin\lambda \sin\gamma_3 - \cos\gamma_3 \cos\lambda) \quad (7.3)$$

$$\rho_2 \sin\alpha \sin\varphi_2 = \rho_1 [\sin\alpha \cos\varphi_1 \sin(\gamma_1 - \gamma_2) \cos\theta_2$$
$$+ \sin\alpha \sin\varphi_1 (\sin\theta_1 \sin\theta_2 + \cos\theta_1 \cos\theta_2 \cos(\gamma_1 - \gamma_2))$$
$$+ \cos\alpha (\cos\theta_1 \sin\theta_2 - \sin\theta_1 \cos\theta_2 \cos(\gamma_1 - \gamma_2))]$$
$$- t_{21} [(V_1 \sin\gamma_2 - V_2 \cos\gamma_2) \cos\theta_2 - V_3 \sin\theta_2]$$
$$- \ell \cos\gamma_2 \cos\theta_2 \quad (7.4)$$

$$\sigma_2 \sin\alpha \sin\psi_2 = \rho_1 \Big[\sin\alpha \cos\varphi_1 \sin(\gamma_1 - \gamma_2) \cos\theta_2 + \sin\alpha \sin\varphi_1 (\sin\theta_1 \sin\theta_2 + \cos\theta_1 \cos\theta_2 \cos(\gamma_1 - \gamma_2)) + \cos\alpha (\cos\theta_1 \sin\theta_2 - \sin\theta_1 \cos\theta_2 \cos(\gamma_1 - \gamma_2)) \Big] - t_{22} \Big[(V_1 \sin\gamma_2 - V_2 \cos\gamma_2) \cos\theta_2 - V_3 \sin\theta_2 \Big] - \ell \cos\gamma_2 \cos\theta_2 \tag{7.5}$$

Next, multiply (4.1) by $\cos\theta_1$ and (6.1) by $(-\sin\theta_1)$ etc. and add:

$$\sigma_1 \cos\alpha = \rho_1 \cos\alpha + t_{12} \Big[(V_1 \sin\gamma_1 - V_2 \cos\gamma_1) \sin\theta_1 + V_3 \cos\theta_1 \Big] \tag{8.1}$$

$$\rho_3 \cos\alpha = \rho_1 \Big[-\sin\alpha \cos\varphi_1 \sin(\gamma_1 - \gamma_3) \sin\theta_3 + \sin\alpha \sin\varphi_1 (\sin\theta_1 \cos\theta_3 - \cos\theta_1 \sin\theta_3 \cos(\gamma_1 - \gamma_3)) + \cos\alpha (\cos\theta_1 \cos\theta_3 + \sin\theta_1 \sin\theta_3 \cos(\gamma_1 - \gamma_3)) \Big] + t_{31} \Big[(V_1 \sin\gamma_3 - V_2 \cos\gamma_3) \sin\theta_3 + V_3 \cos\theta_3 \Big] - m \sin\theta_3 (\sin\lambda \sin\gamma_3 - \cos\lambda \cos\gamma_3) \tag{8.2}$$

$$\sigma_3 \cos\alpha = \rho_1 \Big[-\sin\alpha \cos\varphi_1 \sin(\gamma_1 - \gamma_3) \sin\theta_3 + \sin\alpha \sin\varphi_1 (\sin\theta_1 \cos\theta_3 - \cos\theta_1 \sin\theta_3 \cos(\gamma_1 - \gamma_3)) + \cos\alpha (\cos\theta_1 \cos\theta_3 + \sin\theta_1 \sin\theta_3 \cos(\gamma_1 - \gamma_3)) \Big] + t_{32} \Big[(V_1 \sin\gamma_3 - V_2 \cos\gamma_3) \sin\theta_3 + V_3 \cos\theta_3 \Big] - m \sin\theta_3 (\sin\lambda \sin\gamma_3 - \cos\lambda \cos\gamma_3) \tag{8.3}$$

$$\rho_2 \cos\alpha = \rho_1 \Big[-\sin\alpha \cos\varphi_1 \sin(\gamma_1 - \gamma_2) \sin\theta_2 + \sin\alpha \sin\varphi_1 (\sin\theta_1 \cos\theta_2 - \cos\theta_1 \sin\theta_2 \cos(\gamma_1 - \gamma_2)) + \cos\alpha (\cos\theta_1 \cos\theta_2 + \sin\theta_1 \sin\theta_2 \cos(\gamma_1 - \gamma_2)) \Big] + t_{21} \Big[(V_1 \sin\gamma_2 - V_2 \cos\gamma_2) \sin\theta_2 + V_3 \cos\theta_2 \Big] + \ell \cos\gamma_2 \sin\theta_2 \tag{8.4}$$

$$\sigma_2 \cos\alpha = \rho_1 \Big[-\sin\alpha \cos\varphi_1 \sin(\gamma_1 - \gamma_2) \sin\theta_2 + \sin\alpha \sin\varphi_1 (\sin\theta_1 \cos\theta_2 - \cos\theta_1 \sin\theta_2 \cos(\gamma_1 - \gamma_2)) + \cos\alpha (\cos\theta_1 \cos\theta_2 + \sin\theta_1 \sin\theta_2 \cos(\gamma_1 - \gamma_2)) \Big] + t_{22} \Big[(V_1 \sin\gamma_2 - V_2 \cos\gamma_2) \sin\theta_2 + V_3 \cos\theta_2 \Big] + \ell \cos\gamma_2 \sin\theta_2 \tag{8.5}$$

Equations (5), (7) and (8) constitute 15 equations in 15 unknowns - ρ_i , σ_i , V_i , φ_i , and ψ_i ; i = 1, 2, 3.

Eliminate σ_1 from (5.1) and (7.1) using (8.1), etc.:

$$\left.\begin{aligned} &\tan\alpha \cos\psi_1 \Big[\rho_1 \cos\alpha + t_{12} (V_1 \sin\gamma_1 - V_2 \cos\gamma_1) \sin\theta_1 + V_3 t_{12} \cos\theta_1 \Big] = \rho_1 \sin\alpha \cos\varphi_1 + t_{12} (V_1 \cos\gamma_1 + V_2 \sin\gamma_1) \\ &\tan\alpha \sin\psi_1 \Big[\rho_1 \cos\alpha + t_{12} (V_1 \sin\gamma_1 - V_2 \cos\gamma_1) \sin\theta_1 + V_3 t_{12} \cos\theta_1 \Big] = \rho_1 \sin\alpha \sin\varphi_1 - t_{12} (V_1 \sin\gamma_1 - V_2 \cos\gamma_1) \cos\theta_1 + V_3 t_{12} \sin\theta_1 \end{aligned}\right\} \tag{9.1}$$

$$\left.\begin{array}{l} \tan\alpha \cos\varphi_3 \ [\text{RHS of } (8.2)] = [\text{RHS of } (5.2)] \\ \tan\alpha \sin\varphi_3 \ [\text{RHS of } (8.2)] = [\text{RHS of } (7.2)] \end{array}\right\} \quad (9.2)$$

$$\left.\begin{array}{l} \tan\alpha \cos\psi_3 \ [\text{RHS of } (8.3)] = [\text{RHS of } (5.3)] \\ \tan\alpha \sin\psi_3 \ [\text{RHS of } (8.3)] = [\text{RHS of } (7.3)] \end{array}\right\} \quad (9.3)$$

$$\left.\begin{array}{l} \tan\alpha \cos\varphi_2 \ [\text{RHS of } (8.4)] = [\text{RHS of } (5.4)] \\ \tan\alpha \sin\varphi_2 \ [\text{RHS of } (8.4)] = [\text{RHS of } (7.4)] \end{array}\right\} \quad (9.4)$$

$$\left.\begin{array}{l} \tan\alpha \cos\psi_2 \ [\text{RHS of } (8.5)] = [\text{RHS of } (5.5)] \\ \tan\alpha \sin\psi_2 \ [\text{RHS of } (8.5)] = [\text{RHS of } (7.5)] \end{array}\right\} \quad (9.5)$$

By squaring and adding each of the pairs of equations, we obtain 5 equations in 5 unknowns - V_1, V_2, V_3, ρ_1, φ_1. These are equations (10).

$$\begin{aligned} &\tan^2\alpha \left\{ \rho_1 \cos\alpha + t_{12} \left[(V_1 \sin\gamma_1 - V_2 \cos\gamma_1) \sin\theta_1 + V_3 \cos\theta_1 \right] \right\}^2 = \\ &\rho_1^2 \sin^2\alpha + 2\rho_1 \sin\alpha \, t_{12} \left[\cos\varphi_1 (V_1 \cos\gamma_1 + V_2 \sin\gamma_1) \right. \\ &\quad \left. - \sin\varphi_1 \left(\left[V_1 \sin\gamma_1 - V_2 \cos\gamma_1 \right] \cos\theta_1 - V_3 \sin\theta_1 \right) \right] \\ &\quad + t_{12}^2 \left\{ (V_1 \cos\gamma_1 + V_2 \sin\gamma_1)^2 \right. \\ &\quad \left. + \left[(V_1 \sin\gamma_1 - V_2 \cos\gamma_1) \cos\theta_1 - V_3 \sin\theta_1 \right]^2 \right\} \end{aligned} \quad (10.1)$$

$$\begin{aligned} &\tan^2\alpha \left\{ \rho_1 \left[-\sin\alpha \cos\varphi_1 \sin(\gamma_1 - \gamma_3) \sin\theta_3 \right. \right. \\ &\quad + \sin\alpha \sin\varphi_1 (\sin\theta_1 \cos\theta_3 - \cos\theta_1 \sin\theta_3 \cos(\gamma_1 - \gamma_3)) \\ &\quad \left. + \cos\alpha (\cos\theta_1 \cos\theta_3 + \sin\theta_1 \sin\theta_3 \cos(\gamma_1 - \gamma_3)) \right] \\ &\quad + t_{31} \left[(V_1 \sin\gamma_3 - V_2 \cos\gamma_3) \sin\theta_3 + V_3 \cos\theta_3 \right] \\ &\quad \left. - m \sin\theta_3 (\sin\lambda \sin\gamma_3 - \cos\lambda \cos\gamma_3) \right\}^2 \\ &= \left\{ \rho_1 \left[\sin\alpha \cos\varphi_1 \cos(\gamma_1 - \gamma_3) - \sin\alpha \sin\varphi_1 \cos\theta_1 \sin(\gamma_1 - \gamma_3) \right. \right. \\ &\quad \left. + \cos\alpha \sin\theta_1 \sin(\gamma_1 - \gamma_3) \right] + t_{31} (V_1 \cos\gamma_3 + V_2 \sin\gamma_3) \\ &\quad \left. - m (\sin\lambda \cos\gamma_3 + \sin\gamma_3 \cos\lambda) \right\}^2 \\ &+ \left\{ \rho_1 \left[\sin\alpha \cos\varphi_1 \sin(\gamma_1 - \gamma_3) \cos\theta_3 \right. \right. \\ &\quad + \sin\alpha \sin\varphi_1 (\sin\theta_1 \sin\theta_3 + \cos\theta_1 \cos\theta_3 \cos(\gamma_1 - \gamma_3)) \\ &\quad \left. + \cos\alpha (\cos\theta_1 \sin\theta_3 - \sin\theta_1 \cos\theta_3 \cos(\gamma_1 - \gamma_3)) \right] \\ &\quad - t_{31} \left[(V_1 \sin\gamma_3 - V_2 \cos\gamma_3) \cos\theta_3 - V_3 \sin\theta_3 \right] \\ &\quad \left. + m \cos\theta_3 (\sin\lambda \sin\gamma_3 - \cos\gamma_3 \cos\lambda) \right\}^2 \end{aligned} \quad (10.2)$$

$$\begin{aligned} &\tan^2\alpha \left\{ \rho_1 \left[-\sin\alpha \cos\varphi_1 \sin(\gamma_1 - \gamma_3) \sin\theta_3 \right. \right. \\ &\quad + \sin\alpha \sin\varphi_1 (\sin\theta_1 \cos\theta_3 - \cos\theta_1 \sin\theta_3 \cos(\gamma_1 - \gamma_3)) \\ &\quad \left. + \cos\alpha (\cos\theta_1 \cos\theta_3 + \sin\theta_1 \sin\theta_3 \cos(\gamma_1 - \gamma_3)) \right] \\ &\quad + t_{32} \left[(V_1 \sin\gamma_3 - V_2 \cos\gamma_3) \sin\theta_3 + V_3 \cos\theta_3 \right] \\ &\quad \left. - m \sin\theta_3 (\sin\lambda \sin\gamma_3 - \cos\lambda \cos\gamma_3) \right\}^2 \\ &= \left\{ \rho_1 \left[\sin\alpha \cos\varphi_1 \cos(\gamma_1 - \gamma_3) - \sin\alpha \sin\varphi_1 \cos\theta_1 \sin(\gamma_1 - \gamma_3) \right. \right. \\ &\quad \left. + \cos\alpha \sin\theta_1 \sin(\gamma_1 - \gamma_3) \right] + t_{32} (V_1 \cos\gamma_3 + V_2 \sin\gamma_3) \\ &\quad \left. - m (\sin\lambda \cos\gamma_3 + \sin\gamma_3 \cos\lambda) \right\}^2 \end{aligned}$$

$$
\begin{aligned}
&+ \{ \rho_1 [\sin\alpha \cos\varphi_1 \sin(\gamma_1 - \gamma_3) \cos\theta_3 \\
&\quad + \sin\alpha \sin\varphi_1 (\sin\theta_1 \sin\theta_3 + \cos\theta_1 \cos\theta_3 \cos(\gamma_1 - \gamma_3)) \\
&\quad + \cos\alpha (\cos\theta_1 \sin\theta_3 - \sin\theta_1 \cos\theta_3 \cos(\gamma_1 - \gamma_3))] \\
&\quad - t_{32} [(V_1 \sin\gamma_3 - V_2 \cos\gamma_3) \cos\theta_3 - V_3 \sin\theta_3] \\
&\quad + m \cos\theta_3 (\sin\lambda \sin\gamma_3 - \cos\gamma_3 \cos\lambda) \}^2 \qquad (10.3)
\end{aligned}
$$

$$
\begin{aligned}
&\tan^2\alpha \{ \rho_1 [- \sin\alpha \cos\varphi_1 \sin(\gamma_1 - \gamma_2) \sin\theta_2 \\
&\quad + \sin\alpha \sin\varphi_1 (\sin\theta_1 \cos\theta_2 - \cos\theta_1 \sin\theta_2 \cos(\gamma_1 - \gamma_2)) \\
&\quad + \cos\alpha (\cos\theta_1 \cos\theta_2 + \sin\theta_1 \sin\theta_2 \cos(\gamma_1 - \gamma_2))] \\
&\quad + t_{21} [(V_1 \sin\gamma_2 - V_2 \cos\gamma_2) \sin\theta_2 + V_3 \cos\theta_2] \\
&\quad + \ell \cos\gamma_2 \sin\theta_2 \}^2 \\
&= \{ \rho_1 [\sin\alpha \cos\varphi_1 \cos(\gamma_1 - \gamma_2) - \sin\alpha \sin\varphi_1 \cos\theta_1 \sin(\gamma_1 - \gamma_2) \\
&\quad + \cos\alpha \sin\theta_1 \sin(\gamma_1 - \gamma_2)] + t_{21} (V_1 \cos\gamma_2 + V_2 \sin\gamma_2) \\
&\quad - \ell \sin\gamma_2 \}^2
\end{aligned}
$$

$$
\begin{aligned}
&+ \{ \rho_1 [\sin\alpha \cos\varphi_1 \sin(\gamma_1 - \gamma_2) \cos\theta_2 \\
&\quad + \sin\alpha \sin\varphi_1 (\sin\theta_1 \sin\theta_2 + \cos\theta_1 \cos\theta_2 \cos(\gamma_1 - \gamma_2)) \\
&\quad + \cos\alpha (\cos\theta_1 \sin\theta_2 - \sin\theta_1 \cos\theta_2 \cos(\gamma_1 - \gamma_2))] \\
&\quad - t_{21} [(V_1 \sin\gamma_2 - V_2 \cos\gamma_2) \cos\theta_2 - V_3 \sin\theta_2] \\
&\quad - \ell \cos\gamma_2 \cos\theta_2 \}^2 \qquad (10.4)
\end{aligned}
$$

$$
\begin{aligned}
&\tan^2\alpha \{ \rho_1 [- \sin\alpha \cos\varphi_1 \sin(\gamma_1 - \gamma_2) \sin\theta_2 \\
&\quad + \sin\alpha \sin\varphi_1 (\sin\theta_1 \cos\theta_2 - \cos\theta_1 \sin\theta_2 \cos(\gamma_1 - \gamma_2)) \\
&\quad + \cos\alpha (\cos\theta_1 \cos\theta_2 + \sin\theta_1 \sin\theta_2 \cos(\gamma_1 - \gamma_2))] \\
&\quad + t_{22} [(V_1 \sin\gamma_2 - V_2 \cos\gamma_2) \sin\theta_2 + V_3 \cos\theta_2] \\
&\quad + \ell \cos\gamma_2 \sin\theta_2 \}^2 \\
&= \{ \rho_1 [\sin\alpha \cos\varphi_1 \cos(\gamma_1 - \gamma_2) - \sin\alpha \sin\varphi_1 \cos\theta_1 \sin(\gamma_1 - \gamma_2) \\
&\quad + \cos\alpha \sin\theta_1 \sin(\gamma_1 - \gamma_2)] + t_{22} (V_1 \cos\gamma_2 + V_2 \sin\gamma_2) \\
&\quad - \ell \sin\gamma_2 \}^2
\end{aligned}
$$

$$
\begin{aligned}
&+ \{ \rho_1 [\sin\alpha \cos\varphi_1 \sin(\gamma_1 - \gamma_2) \cos\theta_2 \\
&\quad + \sin\alpha \sin\varphi_1 (\sin\theta_1 \sin\theta_2 + \cos\theta_1 \cos\theta_2 \cos(\gamma_1 - \gamma_2)) \\
&\quad + \cos\alpha (\cos\theta_1 \sin\theta_2 - \sin\theta_1 \cos\theta_2 \cos(\gamma_1 - \gamma_2))] \\
&\quad - t_{22} [(V_1 \sin\gamma_2 - V_2 \cos\gamma_2) \cos\theta_2 - V_3 \sin\theta_2] \\
&\quad - \ell \cos\gamma_2 \cos\theta_2 \}^2 \qquad (10.5)
\end{aligned}
$$

Further reduction of these equations to three equations in three unknowns is possible. However, these equations are more convenient for purposes of computer solution. These five equations in ρ_1, φ_1, V_1, V_2, and V_3 have been programmed for computer iteration using the Secant method for non-linear equations, which is a part of the GE-605 auxiliary library.

IV. LABORATORY MODEL AND EXPERIMENTAL RESULTS

A demonstration model of the Sisyphus system has been assembled for study in the laboratory and the mathematical analysis has been programmed in Fortran IV for computer data reduction. The model consists of three 7-power finder telescopes mated to three RCA-7265 photomultiplier tubes for detectors. The telescopes are mounted with their optical axes nearly parallel and forming an equilateral triangle whose sides are 10.8 cm in length. The telescope objective has a diameter of 3 cm and a focal length of 17.35 cm. A 2.54 cm diameter field aperture restricts the optical system field of view to a cone with a half-angle of 4 degrees. Misalignment, using cone 1 as a reference, is given by $\theta_2 = 3.8 \times 10^{-3}$, $\theta_3 = 1.4 \times 10^{-3}$, $\gamma_2 = 1.79$ and $\gamma_3 = 6.13$ radians, as defined in the misaligned solution in Section II. The θ's here represent the magnitude of the misalignment and the γ's specify the direction.

To simulate a solar illuminated particle, a flying spot scanner is used to project a repetitive sweep across a screen which is in the field of view of the three telescopes. The scanner being used consists of a small mirror attached to the shaft of a synchronous motor. A lens focusses a laser beam on the screen and the rotating mirror causes the spot to traverse the screen. The scanner is located 7 meters from the screen and rotates at 60 rps, resulting in a spot velocity of 5.23 km/sec. The velocity of the spot across the screen was also determined by measuring the time required for the spot to cross a given distance on the screen. By this method of simulating a solar illuminated particle, both the brightness and velocity can be easily controlled. The repetitive character of the sweep greatly eases the observational problem, while an oscilloscope camera can capture single sweep events for analysis of signal to noise characteristics.

The apparatus described has been used to perform a number of experiments demonstrating the system's ability to make range and velocity measurements of illuminated particles. The times at which the spot enters and leaves the field of view of each telescope are made with a digital counter. These times, along with the cone half-angle, the cone separation distance, and the misalignment angles, are the data inputs for the computer program which solves for the particle's position and velocity. An example of the experimental results is listed below:

Trajectory Parameter	Measured	Calculated from Misal. Sisyphus Solu.	Calculated from Aligned Solu.
Entrance Range (m)	5.29	5.56	7
V_1 (km/sec)	5.23	5.28	6.03
V_2 "	0	-0.71	0.34
V_3 "	0	-0.39	-3.28

Preliminary experiments indicate that the velocity components V_1 and V_2 and the range can be determined accurately with the system. The axial velocity component appears to be more sensitive to errors in time measurement. The accuracy of the time measurements for the above case is approximately $\pm$ 1μ sec. When compared to the

total time to cross a field of view ($\sim 100\mu$ sec), this represents an error of $\sim \pm 1\%$. Circuitry is now being built which will reduce the errors to $\pm 0.1\%$. It should also be noted that more precise methods of obtaining the measured values of range and velocity are being developed.

V. CONCLUSIONS

The latest experimental results, shown above, illustrate the improved agreement between the measured and calculated values of the unknown parameters. The values obtained with the misaligned solution are, in most cases, more nearly correct than those calculated using the aligned solution. It is presently felt that the largest source of error arises from the uncertainty in the transit times due to the optics and electronics. As previously mentioned, circuitry and optics are now being designed which will improve the time measurements and thus, further reduce errors in the velocity and range determinations.

PROJECT REPORT #5

OPTICAL CONSIDERATIONS FOR A SISYPHUS INTERPLANETARY METEOROID MEASUREMENT SYSTEM

METEOROID HAZARDS IN DEEP SPACE

Prepared Under

Contract NAS 9-8104
National Aeronautics & Space Administration
Manned Spacecraft Center
Houston, Texas

Prepared by: S. Chandra
R. Lambert
R. Soberman

Space Sciences Laboratory
Missile and Space Division
General Electric Company
PO Box 8555
Philadelphia, Pennsylvania
19101

I. INTRODUCTION

The Sisyphus concept to measure meteoroids in space has been described elsewhere. Since the meteoroids are sensed by detecting the visible solar radiation reflected from the particles, a primary consideration is the optical subsystems. The light is collected by a telescope system that must form a sharp image of the particle in the focal plane. In this same plane is a field stop to define the field of view. When a particle passes in front of the Sisyphus system, its image enters and exits the field of view as defined by the field stops. By making the image in each telescope sharp at the edges of the field stop, photoelectric detection of the light signal enables the measurement of the entry and exit times to the precision which is necessary for range and velocity measurements of the meteoroids.

II. SYSTEM DESIGN

A. Design Constraints for the Optical System

Following are the constraints that must be taken into account in designing the optical system.

1. very light weight
2. compact size for volume considerations
3. rigid and compact construction to withstand the acceleration vibration and shock environment of space flight
4. no moving parts that can result in operational failures

B. Design Requirements

1. Adequately large light collection area of the optics.
2. Short effective focal-length system so that a small light-weight photomultiplier can cover a 10-degree field of view.
3. Images must be very sharp at the field stop edges.

C. Design Concept

Normally the requirements of a large aperture and short focal length optics to yield very sharp images over as large a field as 10-degrees can be achieved only with multi-element highly corrected systems such as camera lenses. For six or eight inch aperture optics, an aerial camera type lens would be prohibitively heavy for interplanetary experiments. The problem, however, becomes soluble if instead of using general purpose optics, we use specialized optics which are specifically designed to optimize the following requirements of the Sisyphus system.

1. The images need to be sharp only at the edge of the field stop where the images enter and exit the field of view. Over the inner zones of the field stop plane, this requirement is not necessary because there the optical system acts merely as a light bucket.

2. At the edges of the field of view, the images need only be sharp in the radial direction so that the images enter and exit the field of view instantly. A small elongation of the image in the tangential direction will not do any harm. This concept is illustrated in Figure 1 where the short lines indicate the shape of the image at various times as the particle moves across the field of view.

D. Aberration Analysis

The main aberrations (the so-called Seidel aberrations) of any optical system are:

1. spherical aberration
2. coma
3. astigmatism
4. image curvature
5. distortion
6. aberration due to materials (e.g., chromatic aberrations)

For an on-axis object (very small field-of-view) only the spherical and chromatic aberrations exist. However, for a large angle field of view, all the aberrations need to be considered.

The chromatic aberrations can be avoided by using reflecting optics in the image forming part of the optical system. For imaging point objects, image distortion is of no consequence. The image curvature will not present any problems because we need sharp focus only at the rim of the field where the off-axis angle remains constant. Therefore, the field curvature effects can be avoided by setting the field-stop for the location of the rim region focus. The astigmatism characterises the behavior of an optical system forming the images in two orthogonal directions (radial and tangential directions) at two different focal planes. For the Sisyphus system, the images need to be sharp only in the radial direction and an elongation of the images in the tangential direction is acceptable. Therefore, by paying attention to only the radial focus, the effects of astigmatism can be neutralized. (Figure 1 shows the images in-focus in the radial direction in the rim region). The other two aberrations, spherical aberration and coma, increase rapidly for fast f-ratios and for increases in the field of view. Since the Sisyphus system requires both fast f-ratio and large angles, the optical system must be free of spherical aberration and coma.

Conclusion: The optical system must be aplanatic (free of spherical aberration and coma), however, it may have other aberrations (excepting chromatic aberration).

III. DETAILED DESIGN

A. Preliminary Study

Before a detailed investigation for the needs and design of an optimum optical design was undertaken, a "first cut" analysis was made for a conventional parabolic

mirror system (which is free of the on-axis spherical aberration) to see if it would provide adequately sharp images at 4 or 5 degrees off the axis (see Appendix to this section). Aberrations due to coma alone was 6 milliradians. If an assumption is made that the image due to aberrations is a symmetrical circle, the effects of the aberrations cancel out to a fair extent and have only minor effects in the calculation of the particle range and velocity. However, in the practical situation, the aberrations will be serious effects due to the following two reasons:

1. The comatic images (main source of aberration) are not circulat but highly non-symmetrical in the radial direction. Therefore, the effects of aberration will be diminished only to a small degree, and there will be a considerable error in range and velocity measurement.

2. An image which is extended in the radial direction will enter the field only gradually. Correspondingly, this will produce a slowly rising impulse in the photomultiplier output. If it enters the different telescope fields of view with different entrance angles, then the rise times will not be similar leading to differential time errors. However, much higher timing accuracy can be obtained if the images are sharp and there is a sudden impulse than if the images are blurred and the impulses gradual.

From these considerations, it was clear that a conventional parabolic system was inadequate for the needs of the Sisyphus system and specially designed optics are needed.

B. Detailed Specifications of the Optical System

Various wide angle systems such as those due to Schmidt, Maksutov and Baker-Schmidt were considered. The Schmidt and Baker-Schmidt system require rather long tube lengths which is undesirable from plane and structural considerations for space flight. The Maksutov system has the disadvantage that it requires a rather thick and heavy refractive corrector element in front which is unrealistic for space flight. The Ritchey-Chretien system, in which both the primary and secondary mirrors are conics (often hyperbolas whose eccentricity is determined from the detailed calculations for each system) turns out to be the best suited one for the Sisyphus optics. This last system is aplanatic (free of coma and spherical aberrations) for arbitrarily wide field of view. The original concept and theory of this system was developed by K. Schwarzschild whose notation is used here. Usually the limit of usefulness of such a system is set by the astigmatism and field curvature. However, as we have discussed earlier, these aberrations can be neutralized by a proper selection of the focal-plane. Therefore, of the various optical systems currently known, the Ritchey-Chretien appears to meet the requirement best.

C. Calculation of the Components

The following formulas were used for calculating the details of the Ritchey-Chretien system:

Notation:

D	diameter of the primary mirror
F	focal length of the primary-secondary system
F_1	focal length of the primary system
F_2	focal length of the secondary system
e_p	eccentricity of the primary system
e_s	eccentricity of the secondary system
D_s	minimum diameter of the secondary to provide an unvignetted image
E	distance of the focal plane in front (-E) or behind (+E) the primary mirror
d	separation between the primary and secondary
α	half angle of the field of view

$$d = \frac{F_1 (F - E)}{F + F_1} \tag{1}$$

$$D_s = \frac{(d + E) D}{F} + 2 d \alpha \tag{2}$$

$$e_p = \left[1 + 2 \left(\frac{F_1}{F}\right)^2 \left(\frac{F_1 - d}{d}\right)\right]^{1/2} \tag{3}$$

$$e_s = \left[\frac{2 F F_1^3}{d (F - F_1)^3} - \left(\frac{F + F_1}{F - F_1}\right)^2\right]^{1/2} \tag{4}$$

$$\text{Tangential length of the image} = \frac{F_1 (2F - d)}{4 (F_1 - d)} \cdot \alpha^2 \tag{5}$$

$$\text{Angular diameter for the circle of least confusion due to astigmatism} = \frac{F_1 (2F - d)}{4 F^2 (F_1 - d)} \cdot D \cdot \alpha^2 \tag{6}$$

Calculations were made for a number of combinations with these parameters:

1. diameter of the primary mirror = 8 inches
2. focal length of the primary mirror = 5, 6, 7, 8, 9, 10 inches
3. focal length of the primary-secondary combined system = 6, 8, 10, 12 inches
4. field of view = 0.2, 0.14 radians
5. focal plane
   - (a) one inch in front of the vertex of the primary mirror (E = -1)
   - (b) in the plane of the vertex of the primary mirror (E = 0)
   - (c) two inches behind the plane of the vertex of the primary mirror (E = +2)

Specifications for a typical system might be as follows:

Input parameters:

diameter of the primary = 8 inches
focal length of the primary = 6 inches (f/0.75 mirror A)
focal length of the combination = 10 inches (f/1.25 system)
field of view = 0.2 radians
focal plane location = 1 inch in front of the vertex of the primary mirror

Calculated values:

distance between the primary and the secondary mirrors = 4.125 inches
diameter of the secondary for an unvignetted field of view = 3.3 inches
eccentricity of the primary = 1.152
eccentricity of the secondary = 5.687
focal length of the secondary = 5.689 inches
rim to vertex depth in the primary = 0.615 inch
tangential length of the astigmatic blur with the image 0.1 radian off the axis = 0.10 inch
near axis (= .01 radian) circle of least confusion = 7×10^{-5} radians

The above optical design is shown in Figure 2. In this figure, A is an 8-inch diameter concave hyperbolic primary (eccentricity = 1.152), B is the convex hyperbolic secondary (eccentricity = 5.689, focal length 4.69 inch, diameter 3.3 inch) at a distance of 4.125 inch from the primary. The resulting focal plane (which is one inch in front of the vertex of the primary) is at B where a precision cut circular field stop is placed to define the cone of view of the Sisyphus system (0.2 radians). A Fabry lens L images the primary (illuminated by the light of the source) on the photocathode surface of a small photomultiplier. The final version of the optical design will need some modification if it is used for simultaneous dual experiments as will be discussed later.

Some of the aspects of this optical design deserve special comments.

1. Resolution

As has been discussed earlier, the radial dimension of the images will have no width except for the effects of diffraction. The resolution for diffraction limited eight inch aperture optics is 0.7 arc sec (3.5×10^{-6} radians). However, if the optics have a $\lambda/3$ figuring accuracy, the resolution will be 0.075 milliradians which is slightly better than the image sharpness requirement of 0.1 milliradians commensurate with the electronics for the Sisyphus system.

2. Optics Material

The optics will be made of glass coated electroformed aluminum which can be constructed in extremely light weight form. The total weight for an 8-inch optics system is about 0.5 pounds including photomultiplier but excluding supports. An accuracy of $\lambda/4$ in figuring has been achieved with this material. A 30-inch mirror so constructed has already been flown.

3. Central Obscuration

One consequence of demanding a very compact system is that the secondary mirror has to be significantly larger than the conventional cassegranian telescopes of high focal ratio. However, the structural advantages of compactness outweigh the slight increase in central obscuration (which will be less than 2. % and, therefore, will yield an effective aperture diameter of 7 inches).

4. Support Structure

By making the optical system compact, it will be possible to support the primary mirror on the main supporting frame and to have the photomultiplier and the secondary mirror counterbalancing each other on the two sides of the primary. This will enable reduction in the weight of the supporting structure and thus minimize the tendency of the high g loading on launch to cause misalignment.

5. Optical Coupling with the Photomultiplier

Need of covering as large a field as 0.2 radians normally would require a large size photomultiplier to collect the full field of view (2 inch diameter photocathode area for a 10 inch focal length system). However, by using an ordinary quality light-weight field lens of plastic, the whole field of view can be brought to the small cathode area of a small light-weight photomultiplier. An alternative is to use the field lens in the Fabry lens mode such that the 8-inch primary located at an effective distance of 10 inches is imaged to 3/4 inch size. This arrangement will freeze the light-spot location on the photomultiplier irrespective of the location of the object in the field. Therefore, the effects of the sensitivity irregularities over the photocathode surface will be eliminated.

IV. DUAL EXPERIMENT POSSIBILITY

One unusual feature of the Sisyphus optics is that only the outer edge of the field of view is of importance, and a small part of the central field can be redirected with a mirror to another detector for another experiment such as a planetary scan.

It is important to note that such a dual experiment would not entail use of any moving parts which may be liable to mechanical failure, nor would it require a beam splitter which effectively cuts the light gathering power of the system to half. Because the two experiments will be using different parts of the field of view, both will have the full light gathering power of the 8-inch optics. The actual details of removing to one side a small central portion of the field of view would depend upon the size, shape and weight considerations of the detector used in the second experiment; however, the possibility of carrying out two experiments with the same optics is quite feasible and should be pointed out in future proposals.

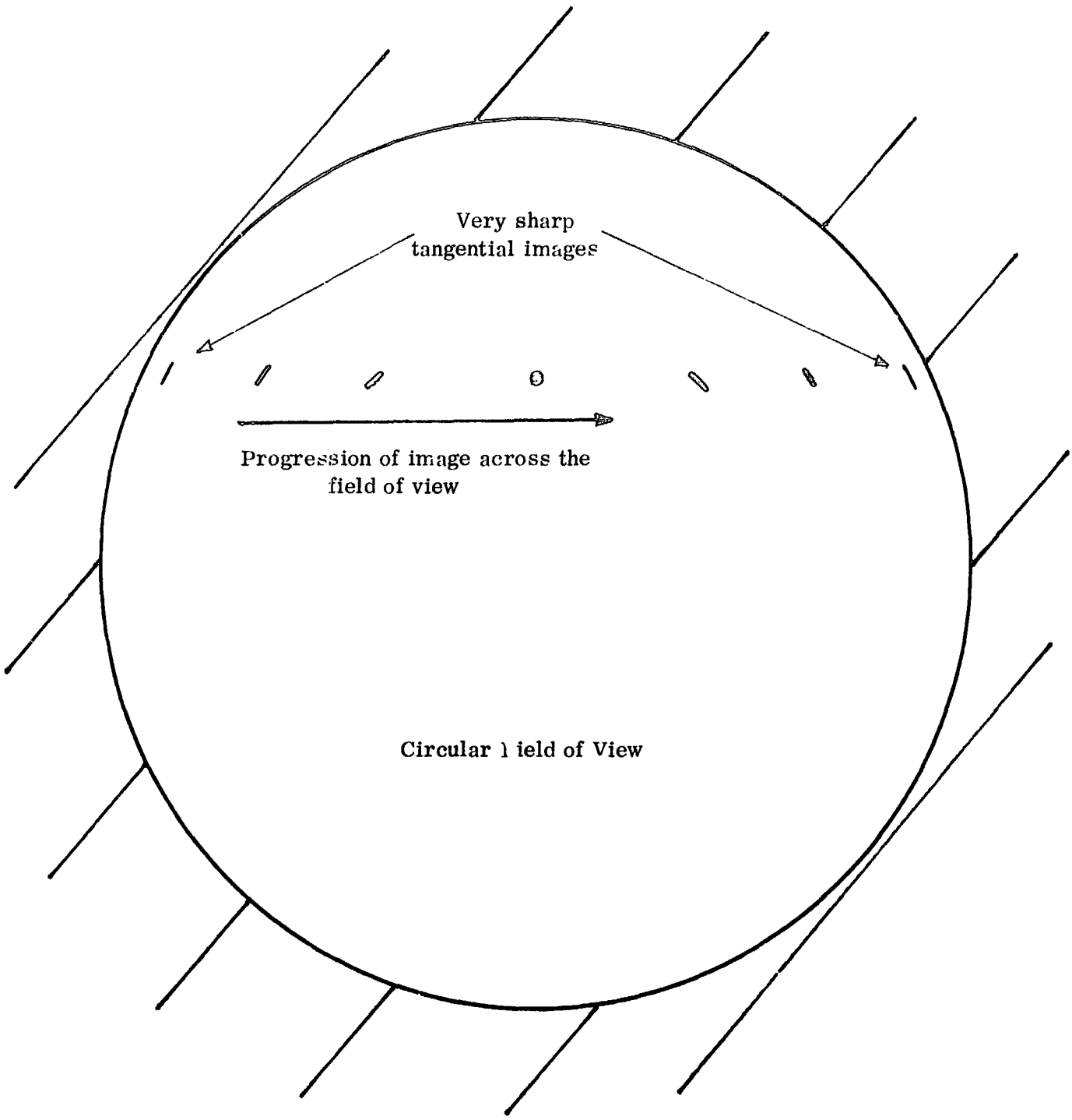

Figure 1. Variation of image shape as it traverses the circular field of view.

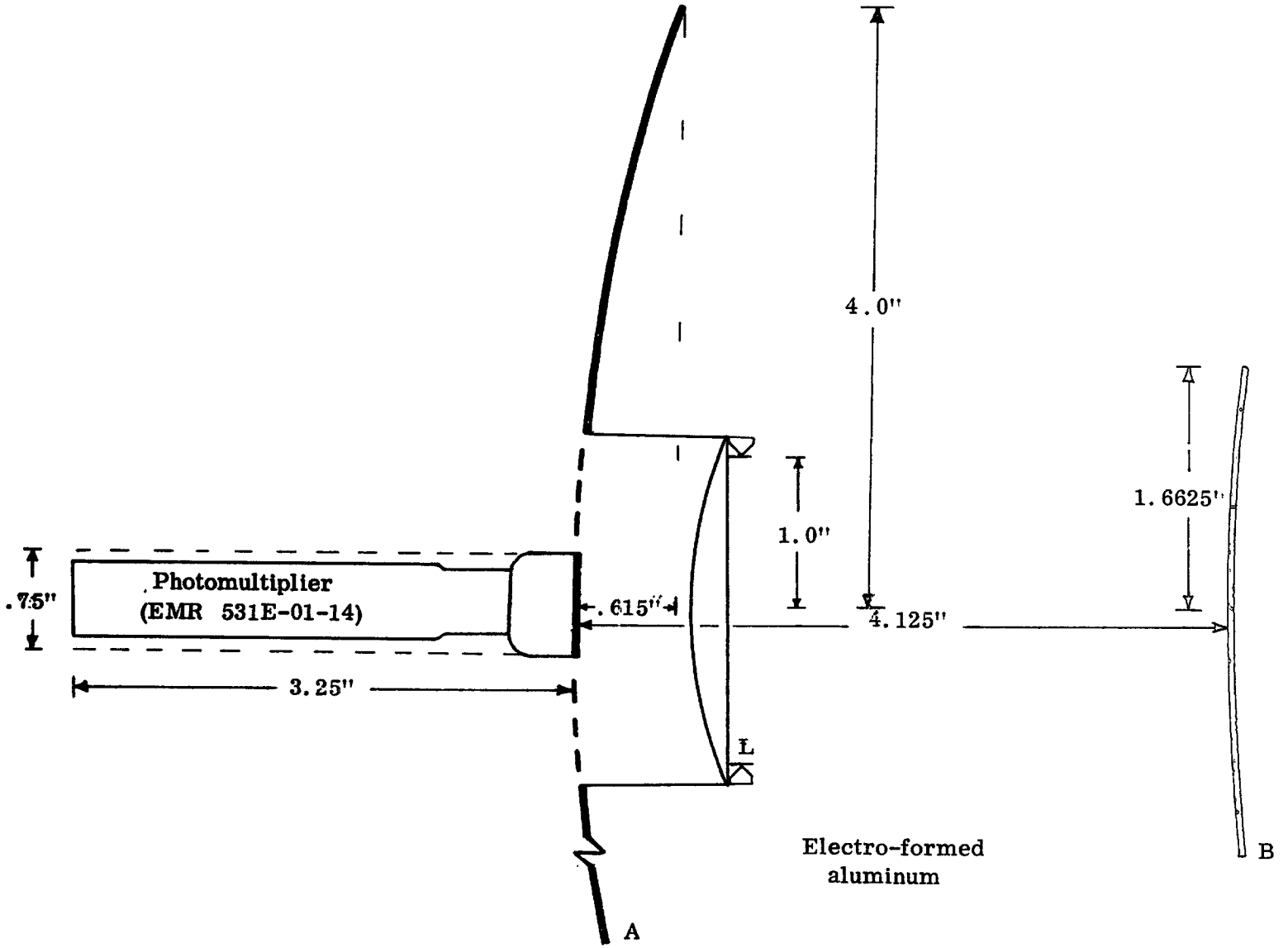

Figure 2. Preliminary Optical Design Drawing

V.

APPENDIX

SISYPHUS OPTICAL ACCURACY

by

R. H. Lambert

Degradation of the image formed by the optical system will cause changes in the apparent transit times. It is the purpose of this PIR to identify sources of image degradation, estimate their angular magnitude and resulting time variations.

General Considerations

It will be assumed that the imaging system is that being considered for the Meteorid Hazards instrument, namely 6" diameter, F/1 electro formed mirrors. With 1" diameter photomultipliers, these mirrors will yield a total field of view of 9.5 degrees or 162 m radians.

If we consider a simple spherical mirror, the major source of image degradation will be spherical aberration. A simple but useful approximation for the image size produced on axis by a spherical mirror is

$$s = 7.8 \times 10^{-3}/F^{+3}$$

radians. At F/1 this approximation is accurate to within 3 percent. For the system in question, the variation is 7.8 mr approximately 5% of the total field, however, at F/2 the magnitude would be less than 1 mr on axis.

To completely correct for spherical aberration we must resort to an aspheric surface, namely a paraboloid. The hieght of the surface X at a radius r from the axis is

$$x = r^2/4f$$

where f is the focal length. In many cases it is not necessary to have a perfect paraboloid since its image may be far smaller than required. A parabolic mirror of 6" diameter will produce a diffraction limited image of $\simeq$.01 m radians. The amount of material to be removed from a sphere of radius R to generate a paraboloid touching the sphere at the center and radius r_o in units of focal length is

$$\frac{T}{f} = \frac{1}{2^{10} F^4} \left(\frac{r}{r_o}\right)^2 \left[\left(\frac{r}{T_o}\right)^2 - 1\right]$$

From this expression we can estimate the surface accuracy necessary to produce an image which will not exceed some specified intermediary size.

In considering off axis imagery the error which first enlarges the image is coma. The effective angular size of the comatic image is

$$c = \frac{U}{16\ F^2}$$

where U is the half angle of the system. For the system in question $\approx$ 5 m radians or roughly 3% of the total field.

At large field angles astigmatism is an important contributor to image size. The angular substance on a flat focal plane is given by

$$as = \frac{U^2}{F} = 6.7 \text{ microns}$$

or approximately 4% of the total field. There are other smaller sources of image degradation but their relative contribution is small compared to those mentioned above. They will not be considered.

Variation in Signal

The off axis effects are neither symetric nor are they uniform. As a first approximation, however, we will asume that the images produced are perfectly round, uniformly illuminated and their maximum size is given by the sum of the three image degradation mechanisms. It will also be assumed that the total field of view is large compared to the image size. The following figure shows the geometry involved when a finite size image enters the field stop

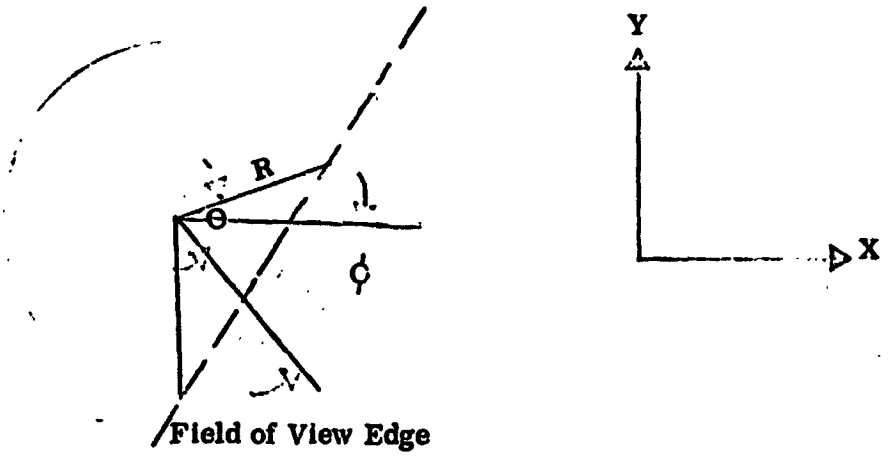

The shaded area defined by the intersection of the image with the edge of the field of view is directly proportional to the signal level. The signal level is given by

$$S = \frac{2}{360} r^2 \Theta - \frac{1}{2} r^2 \text{ Sin } 2\Theta$$

And the position x is given by

$$x = r \frac{\text{Cos } \Theta}{\text{Cos } \phi}$$

Calculated Variations

From the above equations, we can derive the temporal variations in signal at a given velocity for particles passing perpendicularly to the axis of the field of view. Since the system, as presently conceived, begins to measure time at a fixed level above threshold, the variation in transit time will depend on the absolute strength of the signal image. The signal from a degraded circular image has a rise time history shaped as a cosine function. A bright circularly degraded image will appear to have a longer transit time than that of an equally bright true point image. By the same reasoning, a degraded low level signal will have a shorter transit time than that of an equivalent point source. In all the following cases considered, the threshold level has been assumed to be 67% of peak signal. This peak level will correspond to the lowest signal level necessary for coincidence in the presently conceived system.

Cases Considered

As a first cut at determining the errors in range and velocity due to image degradation, we have compared the resulting differences between a point image and a circularly degraded image in the following four field of view configurations.

Configurations 1 and 3 are the fields of view at the minimum range. Configurations 2 and 4 are the fields of view at three times minimum range. In all cases, the vector particle velocity was assumed to be 2.40×10^5 ft/sec; the highest meteoric velocity expected in earth orbit and a minimum range of 11.5 ft.

Field-of-View Configurations

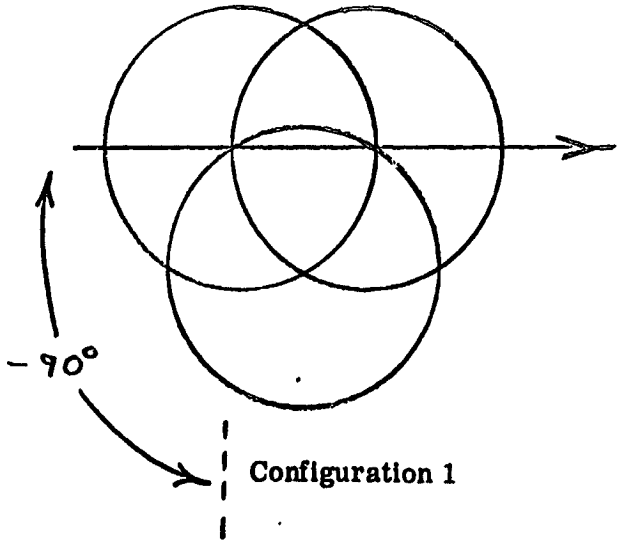

Configuration 1

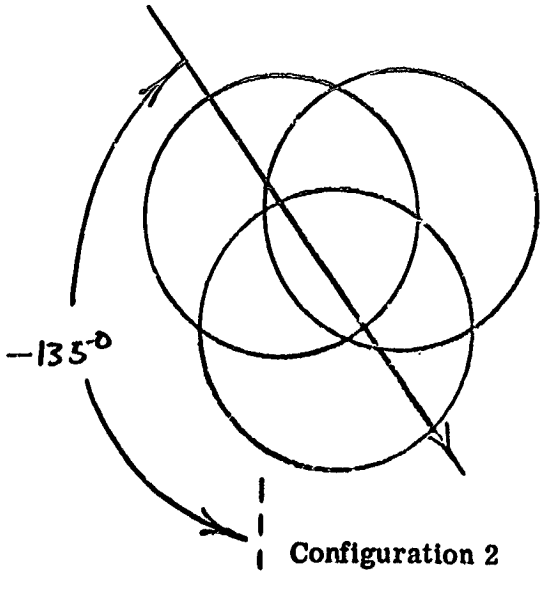

Configuration 2

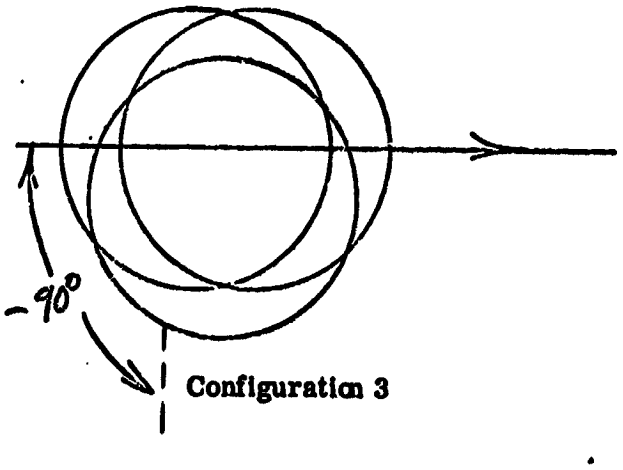

Configuration 3

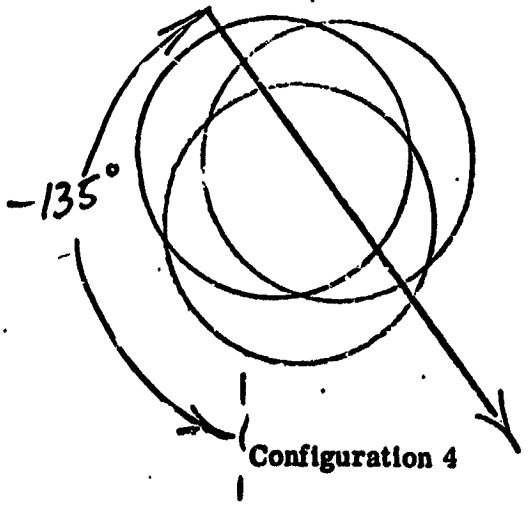

Configuration 4

Results

In all cases, the errors in transit times produced a shortening in the range measurements. As expected, the error in the range measurement is linearly proportional to the image size. See figure 1. In addition, the percent error is both independent of velocity and the absolute range distance. The results also show that for symmetrical errors in time, there is less than .001% error in the x and y velocities.

When the particle entered at the 90° point, the plane of the trajectory remained perpendicular to the line of sight in all cases. This was not the case when the particle entered at 135°. If we consider a positive tilt as one in which the exit range is shorter than the entrance range, then at minimum range the trajectory assumes an increasing positive tilt with increasing image size. At 3 times minimum range, the trajectory assumed an increasing negative tilt with increasing image size. In each case, the z velocity increased proportionately. Figure 2 shows the two results. This result may be attributable to different percentage changes in time (even though symmetric) in each of the three fields of view.

Conclusions

1. As long as the time errors on entrances and exits are symmetrical (i.e, one has a circular blur and entry and exit to the fields of view are at similar angles), then the resultant velocity errors are small.

2. Since the above symmetry is unrealistic due to three-dimensional field traversal and asymmetric optical aberrations, investigations into methods of achieving better imagery through the use of better optics and/or designing for good imagery at the format edges are an absolute necessity.

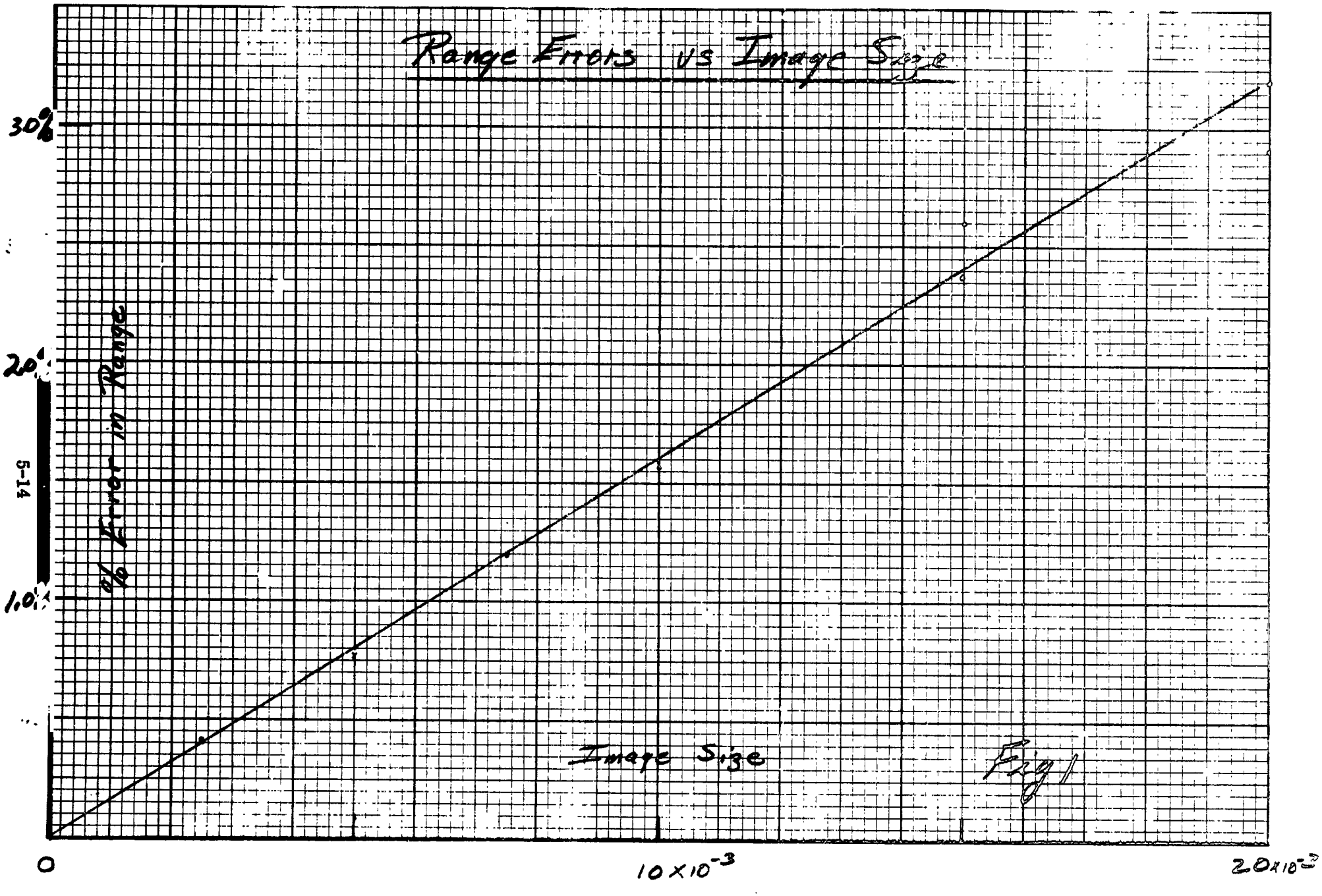
Range Errors vs Image Size
30%
20%
1.0%
% Error in Range
Image Size
0
10 x 10⁻³
20 x 10⁻³
Fig 1

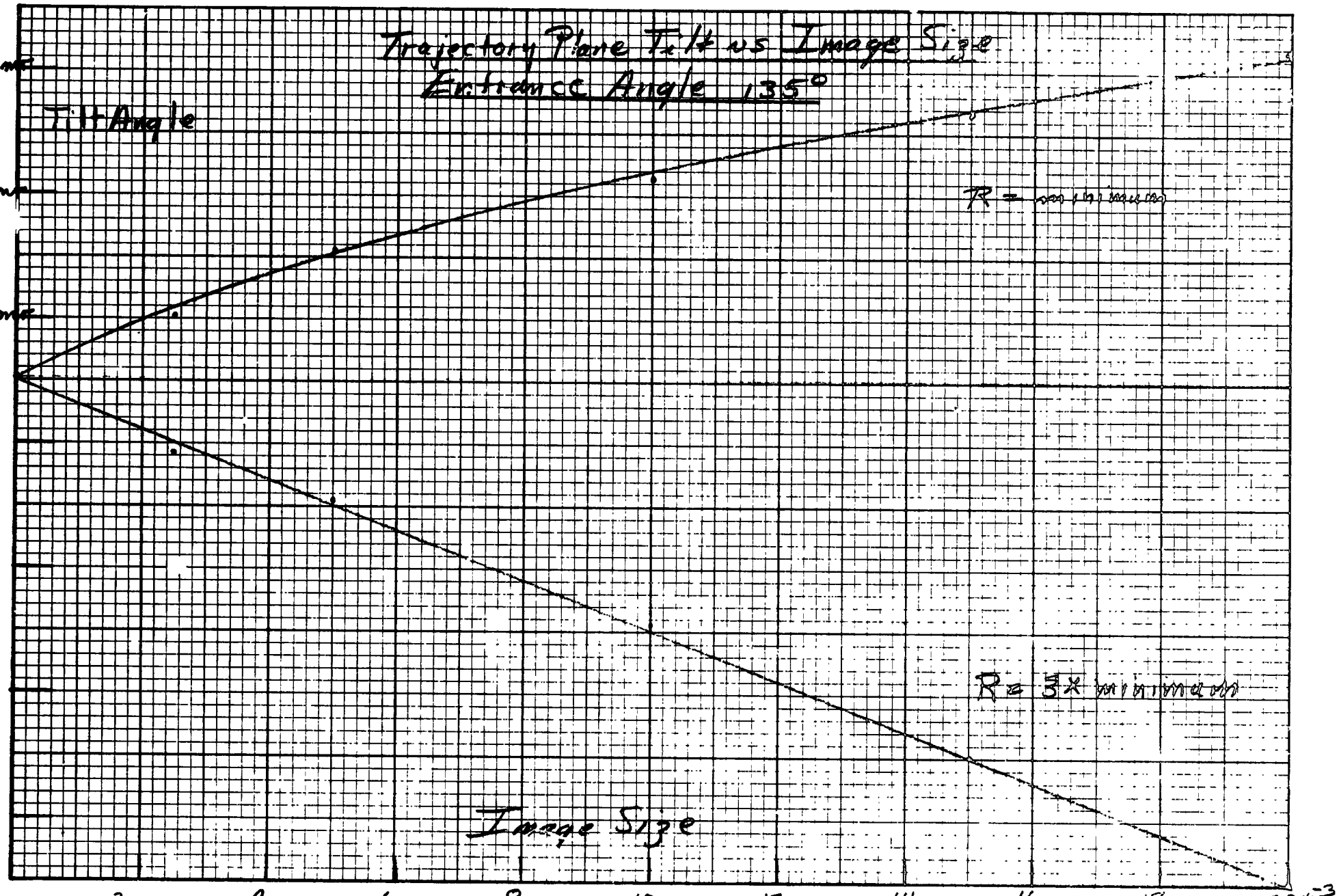

Fig 2

5-15/16

10 X 10 TO THE INCH 5DG